Master thesis and internship[BR]- Master's thesis : Analysis and simulation of aeroelastic effects in turbomachinery[BR]- Internship

Auteur : Camus, Sarah
Promoteur(s) : Dimitriadis, Grigorios
Faculté : Faculté des Sciences appliquées
Diplôme : Master en ingénieur civil en aérospatiale, à finalité spécialisée en "aerospace engineering"
Année académique : 2023-2024
URI/URL : http://hdl.handle.net/2268.2/21138

Analysis and simulation of aeroelastic effects in turbomachinery

Study by means of reduced order modeling techniques for problems with friction.

by

Camus Sarah

Master Thesis for the degree of Master Science in Aerospace Engineering

Supervisor :	Dimitriadis G.
Co-supervisors :	Martel C., Gonzalez-Monge J., Rodriguez Blanco S. and Salles L.
Institution:	Université de Liège - Faculté des Sciences Appliquées
Place:	Liège, Belgique
Academic year :	2023-2024

UNIVERSIDAD
POLITÉCNICA
DE MADRID

Abstract

This thesis investigates the structural dynamics of turbomachinery components, with a focus on the application of reduced order modeling techniques to enhance computational efficiency. The Craig-Bampton substructure coupling method is employed to reduce the computational time required for the dynamic analysis of a bladed-disk model while maintaining accuracy. The study is conducted using two distinct strategies: one involving a change of variables applied before the reduction method, and the other without such a transformation. These strategies are compared in terms of convergence and accuracy across various scenarios, including a realistic bladed-disk sector model.

In addition to the linear analysis, the thesis extends its scope to incorporate nonlinearities, recognizing the significant impact that nonlinear elements can have on the dynamic response of real-world systems. Nonlinear polynomial stiffness and Coulomb friction are introduced into the reduced models to capture these effects. The nonlinear analysis is performed using harmonic balance continuation, and the results are compared across both reduction strategies to evaluate their effectiveness in accurately representing the nonlinear dynamics.

The findings demonstrate that while both strategies yield consistent results in the linear analysis, the nonlinear dynamics introduce complexities that are captured differently by each approach. The study concludes that the Change of Variables (COV) method offers a slight computational advantage and maintains accuracy, particularly in scenarios involving nonlinear interactions.

This work not only validates the use of the Craig-Bampton reduction method for efficient dynamic analysis but also provides insights into the optimal strategy for incorporating nonlinearities in reduced-order models. The results are significant for advancing the modeling and analysis of turbomachinery components, where both linear and nonlinear dynamic behaviors play a critical role in performance and safety.

Acknowledgements

This thesis represents the culmination of my academic journey, and it would not have been possible without the support, guidance, and encouragement of many individuals.

First and foremost, I would like to express my deepest gratitude to my supervisor, Grigorios Dimitriadis from the Université de Liège, for his unwavering confidence in my abilities and his insightful guidance throughout this project. His expertise and encouragement were invaluable to the successful completion of this thesis.

I am profoundly grateful to my co-supervisors, Carlos Martel, Javier Gonzalez-Monge, and Salvador Rodriguez Blanco, from the Universidad Politécnica de Madrid. Their warm welcome and generous availability during the initial phase of my research were instrumental. The incredible experience I had in Madrid was largely due to their support and kindness, which significantly enriched my academic journey.

A heartfelt thank you goes to the members of my jury, Loic Salles and Gaetan Kerschen. Their invaluable advice, particularly in the second part of my thesis focusing on nonlinear dynamics, was instrumental in shaping my research. They provided crucial insights and supervision that guided me through the complex challenges associated with the nonlinear analysis. Their willingness to engage deeply with my work and their constructive feedback played a significant role in refining and enhancing the quality of this thesis. I am truly grateful for their dedication and the time they invested in helping me achieve my academic goals.

I am deeply indebted to my family for their unwavering support and encouragement throughout my studies. Their belief in me has been a constant source of motivation.

I would also like to thank my friends, especially those from my Master's program in Aerospace Engineering. Their camaraderie and the unforgettable moments we shared made these years truly special.

Lastly, I extend my appreciation to everyone who has contributed to my academic journey, whether directly or indirectly. Your support has made this achievement possible, and I am sincerely grateful.

CONTENTS

CHAPTER 1

INTRODUCTION

Gas turbines, integral components of modern propulsion systems and power generation plants, play a pivotal role in converting fuel into mechanical energy. An exemplary representation of such a turbine is provided in Figure 1.1. These sophisticated machines, however, are not immune to the challenges posed by the dynamic forces they endure during operation. One of the critical aspects that demand meticulous attention is the occurrence of blade vibrations within gas turbines. These vibrations are a consequence of complex aeromechanical phenomena, notably flutter and forced response, which significantly impact the structural integrity and overall performance of the turbine blades.

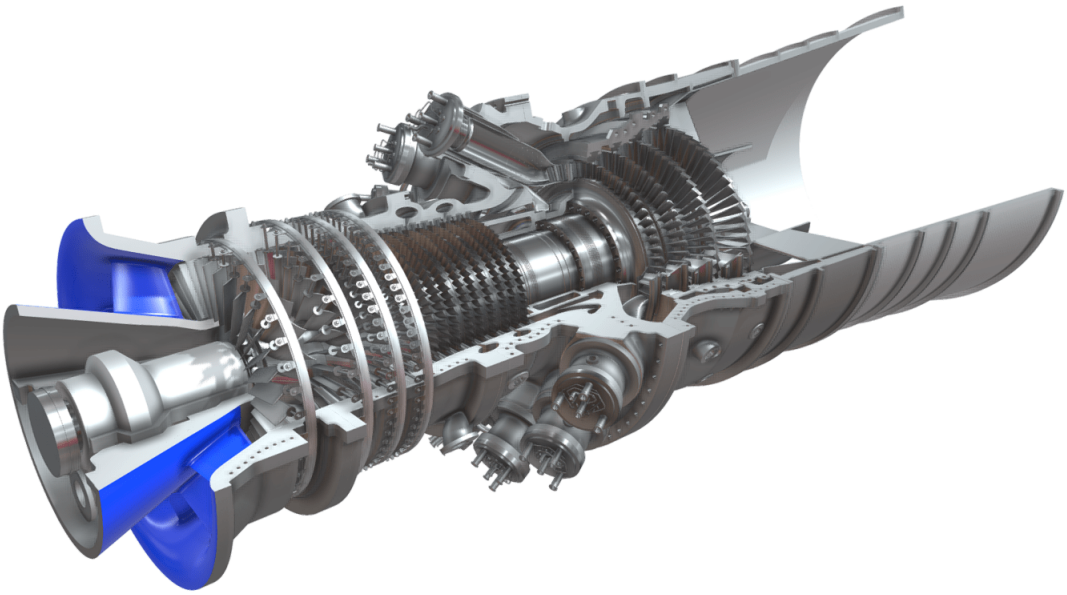

Figure 1.1: Typical gas turbine [1].

According to the article of the *Encyclopedia of Aerospace Engineering* about turbomachinery aeroelasticity [2], flutter, a self-excited vibration phenomenon, arises when the aerodynamic forces acting on a blade interact with its structural dynamics. This intricate interplay between aerodynamics and structural mechanics can lead to destructive oscillations, potentially com-

promising the turbine's reliability and longevity. On the other hand, forced response occurs when external forces, such as those induced by uneven flow conditions or transient events, excite the turbine blades, causing them to vibrate in a non-uniform manner.

A fundamental concept integral to the understanding of these phenomena is aeroelasticity. Aeroelasticity, a branch of mechanics, explores the interaction between aerodynamic forces and the elasticity of structures. In the context of gas turbines, aeroelasticity helps elucidate how aerodynamic loads influence the structural dynamics of turbine blades, giving rise to phenomena like flutter and forced response.

1.1 Aeromechanics phenomena

Aeromechanical phenomena, illustrated by Collar's triangle in Figure 1.2, emerge through the interplay of inertial, elastic, and aerodynamic forces. When the system experiences solely elastic and aerodynamic forces, it leads to static aeroelasticity. In this scenario, a steady aerodynamic influence induces a twist that can strain the structural capabilities. Conversely, dynamic aeroelasticity occurs when all three forces—inertial, elastic, and aerodynamic—act simultaneously, as seen in instances like flutter and forced response.

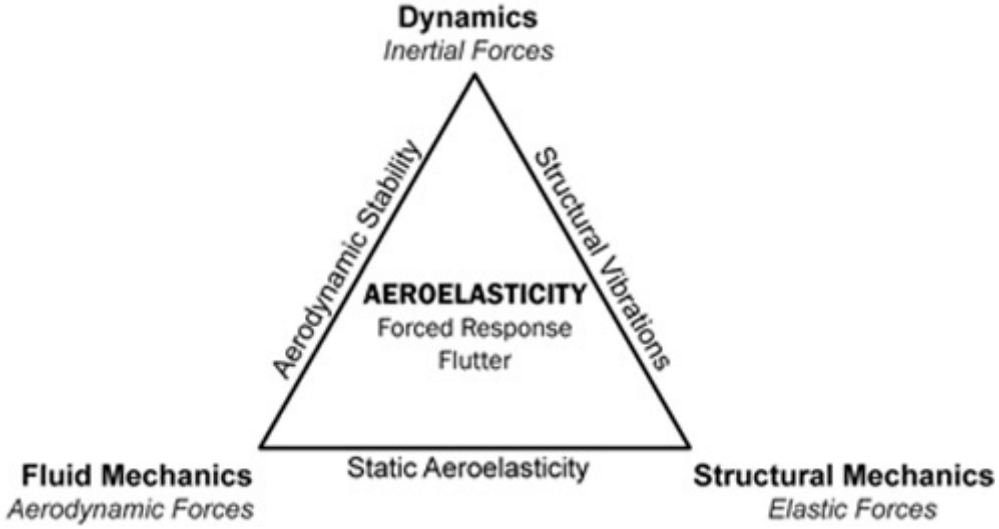

Figure 1.2: Collar's triangle [3].

In a bladed-disk or blisk configuration, as illustrated in Figure 1.3, the term "bladed disk" refers to the rotor — a specific component of the gas turbine. In this context, the inertial force is linked to mass, the elastic force to stiffness, and the aerodynamic force originates from external unsteady influences acting on the blade. These external influences stem from stator-rotor interactions, such as wakes and potential fields. Additionally, unsteady pressure generated by the blade's own motion contributes to the overall aerodynamic force. According to the article of E.P. Petrov and D. J. Ewins [4], the dynamic coupling of these forces gives rise to complex aeromechanical phenomena, shaping the behavior of structures and components in aerospace applications.

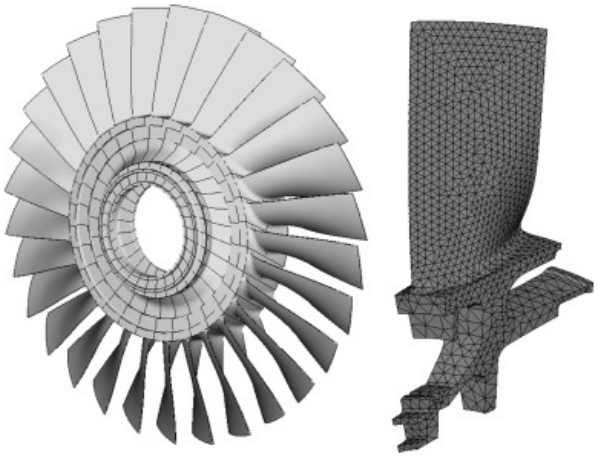

Figure 1.3: Bladed disk scheme [5].

1.2 Reduced Order Models

To ensure the safe and efficient operation of gas turbines, it becomes imperative to delve into the accurate analysis of these blade vibrations. Precise understanding and prediction of the dynamic behavior of turbine blades allow engineers to implement measures that mitigate the detrimental effects of flutter and forced response. In this pursuit, reduced order models (ROMs) emerge as indispensable tools in the field of aeromechanics.

Reduced order models are mathematical representations that capture the essential dynamics of complex systems while significantly reducing computational complexity. In the context of gas turbine blade vibrations, employing reduced order models enables engineers to strike a balance between accuracy and computational efficiency. By distilling the intricate aeromechanical interactions into a simplified yet representative model, engineers can expedite the analysis and design processes, facilitating the development of gas turbines that are robust and reliable under diverse operating conditions.

In this intricate landscape of gas turbine aeromechanics, the use of reduced order models stands as a testament to the ingenuity and precision required to navigate the challenges posed by blade vibrations. This exploration of advanced modeling techniques underscores the commitment of engineers and researchers to advancing the frontiers of gas turbine technology, ensuring that these vital components continue to drive innovation in propulsion and power generation.

1.3 Goal of the thesis

The primary objective of this thesis is to employ the Craig-Bampton reduction method on a bladed-disk model, with the aim of significantly reducing the computational time required for the study while preserving the accuracy of the results. This reduction method will be implemented using two distinct strategies: one involving a change of variables applied before the application of the reduction method, and the other without the incorporation of such a variable transformation. The convergence and accuracy of these two strategies will be rigorously compared, providing insights into the most suitable approach based on the specific model and various imposed conditions.

To achieve this goal, the thesis embarks on a comprehensive review of different reduction methods commonly used in structural and mechanical analyses. This thorough exploration lays the groundwork for a deeper understanding of the intricacies associated with model reduction techniques.

The application of the Craig-Bampton reduction method is initially demonstrated on a simple model featuring 10 degrees of freedom. This foundational step serves as a benchmark for assessing the method's efficiency and accuracy in a controlled setting.

Subsequently, attention is directed toward a more intricate but still simplified model, designed to represent two identical blades. The Craig-Bampton reduction method is then applied to this model, employing both strategies for comparison. This intermediate step allows for a nuanced evaluation of the reduction method's performance as the complexity of the model increases.

The culmination of the study involves the application of the Craig-Bampton reduction method to a realistic bladed-disk sector. By extending the analysis to a more representative and complex configuration, the thesis seeks to draw meaningful conclusions regarding the efficacy of the reduction strategies in real-world scenarios.

Furthermore, recognizing that real-world systems often exhibit nonlinear behaviors that can significantly impact their dynamic response, this thesis incorporates a dedicated chapter on nonlinearities. Nonlinear elements, such as nonlinear polynomial stiffness and Coulomb friction, are introduced into the reduced two-blade model to capture these complex behaviors. By comparing the two reduction strategies in the presence of these nonlinearities, the study aims to evaluate not only their efficiency and accuracy but also their ability to accurately represent the nonlinear dynamic interactions that are critical in practical applications.

Through these systematic investigations, the thesis aims not only to validate the Craig-Bampton reduction method but also to contribute valuable insights into the optimal strategy for achieving computational efficiency without compromising the accuracy of results. The inclusion of nonlinear analysis adds a layer of complexity to the study, making the findings particularly relevant for the broader field of structural and mechanical analyses, especially in the context of bladed-disk modeling where nonlinear effects are often significant.

CHAPTER 2

REDUCTION METHODS IN AEROELASTIC ANALYSIS

Reduction methods play a pivotal role in aeroelastic analysis, particularly in dealing with the complexities of dynamic models for structures like bladed-disks. These methods are essential tools for engineers and researchers, enabling them to simplify intricate structures for efficient analysis. The reduction of degrees of freedom in dynamic models enhances the ability to comprehend and analyze the behavior of structures under dynamic excitation. Without reduction techniques, a study for a typical realistic structure involves on the order of millions of degrees of freedom (for a Finite Element Method (FEM) model), which are intractable to simulate in the time domain.

This chapter explores the significance of reduction methods, provides an overview of various Reduced Order Models (ROMs), and delves into the details of the Craig-Bampton method, emphasizing its importance in maintaining physical displacements at contacts. Additionally, the chapter addresses the challenges posed by nonlinearities in aeroelastic systems and introduces advanced adaptive ROM techniques designed to accurately capture the complex dynamics introduced by these nonlinearities.

2.1 Importance of reduction methods

2.1.1 Simplifying complex structures

Reduction methods are crucial for simplifying complex structures encountered in industries such as aerospace, automotive, and civil engineering. These methods allow engineers to streamline dynamic models, making them more manageable for analysis. By reducing the number of degrees of freedom, engineers can perform accurate and efficient simulations, leading to improved designs and enhanced safety in a wide range of applications.

2.1.2 Efficiency in dynamic analysis

Dynamic analysis of complex structures, such as bladed-disks, demands significant computational effort. Reduction methods offer a way to alleviate this computational weight by transforming the dynamic model into a reduced form while preserving essential characteristics. This efficiency is particularly vital when dealing with large-scale models and considering

factors like mistuning, friction damping, and aerodynamic interactions.

2.2 Overview of reduced order methods

Dynamic analysis encompasses a range of substructure coupling methods that share a unified formulation. These methods, ranging from Guyan reduction to Subset Nominal Mode (SNM) and Component Mode Synthesis (CMS), serve as crucial tools in simplifying complex structures for efficient and accurate analysis. The fundamental differences between these methods lie in the mode sets used to describe substructure generalized coordinates and the techniques employed to enforce compatibility at substructure interfaces.

2.2.1 Definition of mode sets

The physical displacements of each substructure are expressed in terms of substructure generalized coordinates through the use of various "assumed modes." These include normal modes of the substructure and specific static deflection modes. The equation of motion for a substructure undergoing undamped free vibration, connected to other substructures, is formulated as

$$\begin{bmatrix} m_{ii} & m_{ij} \\ m_{ji} & m_{jj} \end{bmatrix} \begin{pmatrix} \ddot{x}_i \\ \ddot{x}_j \end{pmatrix} + \begin{bmatrix} k_{ii} & k_{ij} \\ k_{ji} & k_{jj} \end{bmatrix} \begin{pmatrix} x_i \\ x_j \end{pmatrix} = \begin{pmatrix} 0 \\ 0 \end{pmatrix}. \tag{2.1}$$

Here, the matrices M and K represent the mass and stiffness properties of the substructure, respectively. The terms m_{ii}, m_{ij}, m_{ji}, and m_{jj} in the mass matrix M indicate the self-masses and coupling between different degrees of freedom. Similarly, the terms k_{ii}, k_{ij}, k_{ji}, and k_{jj} in the stiffness matrix K denote the self-stiffness and coupling between degrees of freedom.

In the displacement vector X, x_i and x_j represent the displacements of connected degrees of freedom within the substructure.

This equation describes the dynamic behavior of the substructure undergoing undamped free vibration, capturing how masses and stiffness interact and how displacements evolve over time.

Note that, in the context of free vibration, the absence of external forcing renders the right-hand side vector null.

2.2.2 Fixed-interface normal modes

Fixed-interface normal modes are derived by setting $x_j = 0$ and solving for the free-vibration modes of the substructure. This leads to an eigenvalue problem of the form :

$$\left(k_{ii} - \omega^2 m_{ii}\right) x_i = 0. \tag{2.2}$$

The resulting eigenvalues (frequencies) form a diagonal matrix Λ and the corresponding normalized eigenvectors (mode shapes) form the modal matrix Φ. They can be written as

$$\Lambda = \text{diag}\left(\omega_1^2, \omega_2^2, \cdots, \omega_{N_i}^2\right), \tag{2.3}$$

and

$$\Phi = \begin{bmatrix} \phi_{i1} & \phi_{i2} & \cdots & \phi_{iN_i} \\ 0 & 0 & \cdots & 0 \end{bmatrix}, \tag{2.4}$$

where N_i is the total number of substructure interior coordinates.

2.2.3 Guyan

The Guyan reduction method is a static condensation technique used in structural dynamics to simplify the analysis of complex structures by reducing the number of degrees of freedom. This method was initially introduced by Robert J. Guyan, in his article about the reduction of stiffness and mass matrices [6]. It is particularly useful for computational efficiency while retaining physical interpretations of master nodes. The method involves selecting a subset of degrees of freedom (DOFs) known as master DOFs, which are treated as independent. The remaining DOFs, called slave DOFs, are expressed in terms of these master DOFs, allowing for a reduction in the overall size of the system.

Consider the equation of motion for a substructure undergoing undamped free vibration, connected to other substructures depicted by Equation 2.1.

The Guyan method involves selecting a subset of fixed-interface normal modes to reduce the size of the system. Let's denote the selected master DOFs as m and the corresponding slave DOFs as s.

The transformation matrix of the Guyan method is given by :

$$T_{\text{Guyan}} = \begin{bmatrix} I_{m,m} \\ -k_{s,s}^{-1} k_{s,m} \end{bmatrix} = \begin{bmatrix} I_{m,m} \\ \Phi_{s,m} \end{bmatrix}. \tag{2.5}$$

Here $I_{m,m}$ is the identity matrix corresponding to the master degrees of freedom, $k_{s,s}$ is the stiffness matrix of the slave degrees of freedom while $k_{s,m}$ is the coupling matrix between slave and master degrees of freedom, and $\Phi_{s,m} = -k_{s,s}^{-1} k_{s,m}$ represents the transformation matrix that maps slave displacements to master displacements.

The transformation matrix ensures that the condensed displacements $\tilde{x}$ capture the essential dynamic behavior of the structure while considering the selected master DOFs. The Guyan method relies on the assumption that the slave DOFs can be accurately represented by a linear combination of the master DOFs.

Applying this transformation matrix to the system as

$$\begin{pmatrix} \tilde{x}_m \\ \tilde{x}_s \end{pmatrix} = T_{\text{Guyan}} \cdot \begin{pmatrix} x_m \\ x_s \end{pmatrix}, \tag{2.6}$$

the reduction process leads to the following reduced equations of motion:

$$\begin{bmatrix} \tilde{m}_{mm} & \tilde{m}_{ms} \\ \tilde{m}_{sm} & \tilde{m}_{ss} \end{bmatrix} \begin{pmatrix} \ddot{\tilde{x}}_m \\ \ddot{\tilde{x}}_s \end{pmatrix} + \begin{bmatrix} \tilde{k}_{mm} & \tilde{k}_{ms} \\ \tilde{k}_{sm} & \tilde{k}_{ss} \end{bmatrix} \begin{pmatrix} \tilde{x}_m \\ \tilde{x}_s \end{pmatrix} = \begin{pmatrix} 0 \\ 0 \end{pmatrix}. \tag{2.7}$$

In these reduced equations, $\tilde{M}$ and $\tilde{K}$ represent the condensed mass and stiffness matrices, respectively, capturing the essential characteristics of the system. The tilde notation signifies quantities that have undergone a static condensation process through the Guyan method.

The reduced accelerations $\ddot{\tilde{x}}_m$ and $\ddot{\tilde{x}}_s$ and reduced displacements $\tilde{x}_m$ and $\tilde{x}_s$ correspond to the simplified degrees of freedom resulting from the Guyan reduction. These condensed

quantities offer a computationally efficient representation of the dynamic behavior of the substructure, showcasing the trade-off between accuracy and efficiency inherent in the Guyan method.

2.2.4 Subset Nominal Mode (SNM)

As highlited in the influential work by M.T. Yang and J. H. Griffin [7], the Subset Nominal Mode (SNM) method is a powerful reduced-order modeling technique employed in structural dynamics to streamline the dynamic analysis of intricate structures. Similar to the Guyan reduction method, the SNM approach strikes a balance between accuracy and computational efficiency, focusing on capturing essential dynamic behavior.

Consider the dynamic response of each substructure expressed as a linear combination of fixed-interface normal modes q_i and static correction modes δ_i :

$$\begin{pmatrix} x_i \\ x_j \end{pmatrix} = \begin{pmatrix} \Phi_i \\ \Phi_j \end{pmatrix} \begin{pmatrix} q_i \\ \delta_j \end{pmatrix}. \tag{2.8}$$

In this equation :

- x_i and x_j are the displacements of connected degrees of freedom within the substructure.
- Φ_i and Φ_j are matrices containing fixed-interface normal modes and static correction modes, respectively.
- q_i represents the fixed-interface normal modes.
- δ_j represents the static correction modes.

The mode shapes and frequencies are defined in the modal matrix Φ and diagonal matrix Λ, respectively depicted in Equations 2.4 and 2.3.

The SNM method focuses on selecting a subset of normal modes, called the "nominal mode," to represent the dominant dynamic response of the substructure.

The transformation matrix for SNM, denoted as T_{SNM} is given by:

$$T_{\text{SNM}} = [\Phi_k], \tag{2.9}$$

where Φ_k represents only the dynamic modes selected as the "nominal mode." This transformation matrix serves a crucial role in mapping the original displacements to the reduced set of dynamic modes.

The transformation matrix T_{SNM} is applied to the system as

$$\begin{pmatrix} \tilde{x}_k \\ \tilde{x}_{\text{corr}} \end{pmatrix} = T_{\text{SNM}} \cdot \begin{pmatrix} x_k \\ x_{\text{corr}} \end{pmatrix}, \tag{2.10}$$

where $\tilde{x}_k$ represents the reduced displacements corresponding to the dynamic modes and $\tilde{x}_{\text{corr}}$ represents the reduced displacements corresponding to the static correction modes.

The SNM method leads to the following reduced equations of motion:

$$\begin{bmatrix} \tilde{m}_{k,k} & \tilde{m}_{k,\text{corr}} \\ \tilde{m}_{\text{corr},k} & \tilde{m}_{\text{corr,corr}} \end{bmatrix} \begin{pmatrix} \ddot{\tilde{x}}_k \\ \ddot{\tilde{x}}_{\text{corr}} \end{pmatrix} + \begin{bmatrix} \tilde{k}_{k,k} & \tilde{k}_{k,\text{corr}} \\ \tilde{k}_{\text{corr},k} & \tilde{k}_{\text{corr,corr}} \end{bmatrix} \begin{pmatrix} \tilde{x}_k \\ \tilde{x}_{\text{corr}} \end{pmatrix} = \begin{pmatrix} 0 \\ 0 \end{pmatrix}. \tag{2.11}$$

Here, as for the Guyan method, the $\tilde{M}$ and $\tilde{K}$ represent the condensed mass and stiffness matrices, respectively, capturing the essential characteristics of the system. The tilde notation signifies quantities that have undergone a static condensation process through the SNM method.

The reduced acceleration $\ddot{\tilde{x}}_k$ and $\ddot{\tilde{x}}_{\text{corr}}$ and reduced displacements $\tilde{x}_k$ and $\tilde{x}_{\text{corr}}$ correspond to the simplified degrees of freedom resulting from the SNM method. These condensed quantities provide a computationally efficient representation of the dynamic behavior of the substructure, highlighting the SNM method's effectiveness in reduced-order modeling for structural dynamics.

The dynamic response is thus expressed as a linear combination of these selected modes and static correction modes. This approach simplifies the representation of dynamic behavior while maintaining accuracy, and it can be applied with or without cyclic symmetry.

The SNM method offers advantages in block-diagonal formulations and provides a computationally efficient way to capture the essential dynamic features of the structure. It stands as a versatile tool in the realm of reduced order modeling for structural dynamics.

2.2.5 Component Mode Synthesis (CMS)

Component Mode Synthesis (CMS) stands as a powerful methodology in structural dynamics, incorporating approaches like Craig-Bampton (CB) and Craig-Chang (CC). CMS extends the concept of Guyan reduction by integrating static correction modes, offering a versatile tool for efficient dynamic analysis.

Craig-Bampton

Craig-Bampton (CB) is a component mode synthesis technique that combines static and dynamic modes while maintaining compatibility at interfaces. The transformation matrix for CB, denoted as T_{CB} is given by:

$$T_{\text{CB}} = \begin{bmatrix} \Phi_{i,k} & \Psi_{i,b} \\ 0_{b,k} & I_{b,b} \end{bmatrix}, \tag{2.12}$$

where b stands for the boundary or interface degrees of freedom, i denotes the interior degrees of freedom, and k expresses the number of kept modes. These kept modes are dynamic modes obtained from an eigenvalue problem with fixed interface degrees of freedom.

The static modes $\Psi_{i,b}$ represent the deformation of slave degrees of freedom when master degrees of freedom are displaced, preserving the physical displacements at the interfaces. Specifically, $\Psi_{i,b}$ characterizes how the boundary degrees of freedom respond statically to displacements imposed on the interior degrees of freedom.

The dynamic modes $\Phi_{i,k}$ are a set of modes that capture the dynamic behavior of the system, and they are also obtained from the eigenvalue problem. These modes are retained based on their significance in representing the dynamic response of the structure.

In essence, the transformation matrix T_{CB} combines these static and dynamic components, allowing for the efficient reduction of the original system while preserving essential structural characteristics. This reduced order model becomes a valuable tool in aeroelastic simulations, facilitating computational efficiency without compromising accuracy.

Craig-Chang

Craig-Chang (CC) is another facet of CMS with a free-interface formulation, introducing attachment modes for unconstrained components. The transformation matrix for CC, denoted as T_{CC}, is given by:

$$T_{\text{CC}} = \begin{bmatrix} \Phi_{b,k} & \Psi_{b,b} & \Psi_{b,r} \\ \Phi_{i,k} & \Psi_{i,b} & \Psi_{i,r} \\ \Phi_{r,k} & \Psi_{r,b} & \Psi_{r,r} \end{bmatrix}, \tag{2.13}$$

where

- $\Phi_{b,k}$, $\Phi_{i,k}$ and $\Phi_{r,k}$ represent the boundary, interior, and rigid body modes, respectively.
- $\Psi_{b,b}$, $\Psi_{i,b}$ and $\Psi_{r,b}$ represent the boundary, interior, and rigid body modes contributing to dynamic correction.
- $\Psi_{b,r}$, $\Psi_{i,r}$ and $\Psi_{r,r}$ represent the boundary, interior, and rigid body modes contributing to static correction.

Application of the transformation matrix

For both methods, the transformation matrix is applied to the dynamic response equation as

$$\begin{bmatrix} \tilde{x}_k \\ \tilde{x}_{\text{corr}} \end{bmatrix} = T_{\text{CMS}} \cdot \begin{bmatrix} x_k \\ x_{\text{corr}} \end{bmatrix}, \tag{2.14}$$

where $\tilde{x}_k$ represents the reduced displacements corresponding to dynamic modes, and $\tilde{x}_{\text{corr}}$ represents the reduced displacements corresponding to static correction modes.

The CMS approach leads to the same reduced equations of motion as for the SNM method, described by Equation 2.11, capturing the essential dynamic and static behavior of the structure.

2.3 Craig-Bampton method

In this thesis, the reduced-order method used is Craig-Bampton. The Craig-Bampton method is considered one of the best reduction methods due to its efficiency and accuracy in reducing the degrees of freedom in large structural dynamic systems. This method allows for the reduction of a large finite element model into a smaller, more manageable model while retaining the essential dynamic characteristics of the original system. The reduced model can significantly decrease computational costs while providing accurate dynamic responses. This is achieved by partitioning the structure into component parts, known as substructures, and then coupling these substructures to form the complete structure.

Furthermore, this method treats all boundary freedoms alike, avoiding the need to distinguish between determinate and indeterminate constraints. This simplification is advantageous, especially for highly redundant boundary connections, and eliminates the need to establish equations relating rigid-body generalized coordinates to statically determinate constraint displacements.

2.3.1 Importance of physical displacements

In aeroelastic analysis, maintaining physical displacements at contacts is crucial for accurately representing the structural behavior. The CB method ensures that physical definitions of master nodes remain valid in the reduced space, enhancing the reliability of the analysis. The method achieves this by incorporating static modes, which represent the deformation of slave degrees of freedom when master degrees of freedom are displaced.

2.3.2 Notation for the Craig-Bampton method

Similar to the Guyan method, the Craig-Bampton methodology introduces a specific notation, which will remain consistent throughout this thesis.

Instead of employing the terms "slave" and "master," the notation adopts the terms "elastic" and "contact," denoted by the subscripts "e" and "c" respectively.

To implement the Craig-Bampton method, the degrees of freedom and the matrices associated with them are partitioned into blocks. The vector of degrees of freedom is split as follows

$$x = \begin{pmatrix} x_e \\ x_c \end{pmatrix}, \tag{2.15}$$

while the mass and stiffness matrices are partitioned as

$$M = \begin{bmatrix} M_{ee} & M_{ec} \\ M_{ce} & M_{cc} \end{bmatrix} \qquad \text{and} \qquad K = \begin{bmatrix} K_{ee} & K_{ec} \\ K_{ce} & K_{cc} \end{bmatrix}. \tag{2.16}$$

To maintain consistency with this partitioning, the Craig-Bampton transformation matrix, initially defined in Equation 2.12, can be rewritten as

$$\alpha = \begin{bmatrix} \Phi & \Psi \\ 0 & I \end{bmatrix}, \tag{2.17}$$

where the notation α is used to avoid confusion with the previously defined transformation matrix.

Here, Φ represents the natural vibration modes of the structure, computed by setting the contact displacement to zero ($x_c = 0$) and solving the eigenvalue problem for the elastic degrees of freedom:

$$\left(K_{ee} - \omega^2 M_{ee}\right) x = 0, \tag{2.18}$$

for a given number of modes N_a.

The resulting frequencies obtained from this eigenvalue problem are stored in the diagonal matrix K_{aa}, defined as

$$K_{aa} = \text{diag}\left(\omega_1^2, \omega_2^2, \cdots, \omega_{N_a}^2\right), \tag{2.19}$$

and the associated mode shapes are stored as column vectors in the matrix

$$\Phi = \left(x_1, x_2, \cdots x_{N_a}\right). \tag{2.20}$$

These mode shapes satisfy the relations of the mode shapes of an eigenvalue problem:

$$\Phi^T M_{ee} \Phi = I \qquad \text{and} \qquad \Phi^T K_{ee} \Phi = K_{aa}. \tag{2.21}$$

Regarding the matrix of the constrained mode, corresponding to the static displacement of the elastic degrees of freedom for a prescribed motion of the contacts, it is given by:

$$\Psi = -K_{ee}^{-1} K_{ec}. \tag{2.22}$$

This matrix is obtained by considering all possible displacements of the contacts, where $x_c = I$, and I is the identity matrix.

Applying the transformation matrix to the system as

$$\begin{pmatrix} x_e \\ x_c \end{pmatrix} = \begin{bmatrix} \Phi & \Psi \\ 0 & I \end{bmatrix} \begin{pmatrix} a \\ x_c \end{pmatrix} = \alpha \begin{pmatrix} a \\ x_c \end{pmatrix}, \tag{2.23}$$

where a is a vector containing the amplitude of the N_a natural modes and the contact displacements x_c remain the same as for the full model formulation, the reduction process leads to the following reduced equations of motion:

$$\begin{bmatrix} I & M_{ax} \\ M_{xa} & M_{xx} \end{bmatrix} \begin{pmatrix} \ddot{a} \\ \ddot{x}_c \end{pmatrix} + \begin{bmatrix} K_{aa} & 0 \\ 0 & K_{xx} \end{bmatrix} \begin{pmatrix} a \\ x_c \end{pmatrix} = \begin{pmatrix} 0 \\ 0 \end{pmatrix}, \tag{2.24}$$

where the reduced mass and stiffness matrices are given by:

$$\begin{aligned} M_{ax} &= M_{xa}^T = \Phi^T M_{ee} \Psi + \Phi^T M_{ec}, \\ M_{xx} &= \Psi^T M_{ee} \Psi + \Psi^T M_{ec} + M_{ce} \Psi + M_{cc}, \\ K_{aa} &= \text{diag}\left(\omega_1^2, \omega_2^2, \cdots, \omega_{N_a}^2\right), \\ K_{xx} &= K_{cc} - \Psi^T K_{ee} \Psi. \end{aligned} \tag{2.25}$$

2.4 Incorcoporating nonlinearity in Reduced Order Models

While the Craig-Bampton method and other reduction techniques are highly effective for linear systems, they face challenges when applied to systems with significant nonlinearities. Nonlinearities in aeroelastic systems can arise from various sources, such as material properties, geometric configurations, and contact interactions like friction joints.

Recent research has focused on developing improved adaptive ROMs to address the limitations of traditional methods in capturing nonlinear behaviors. For instance, Yuan et al. [8] [9] introduced an adaptive ROM that dynamically filters out insignificant modes based on an energy-based error estimator, allowing for more efficient and accurate simulations of systems with frictional joints.

In the context of aeroelastic analysis, nonlinear effects are particularly important in systems like fan blade assemblies with dovetail joints. These joints introduce significant nonlinearities due to friction at the contact interfaces, which can lead to complex vibration patterns and energy dissipation mechanisms.

Patil and Datta [10] further demonstrate the importance of incorporating nonlinearities in the analysis of coaxial rotor systems. Their study highlights how nonlinear interactions between the upper and lower rotors, driven by aerodynamic forces and frictional contacts,

result in significant dynamic behaviors that must be accurately modeled to ensure the system's performance and safety .

The development of these advanced adaptive ROMs represents a significant advancement in aeroelastic analysis, providing the necessary tools to capture the intricate behaviors induced by nonlinearities. By integrating these methods, engineers can better predict the performance and safety of aerospace structures, leading to more accurate and reliable designs.

2.5 Conclusion

Reduction methods are indispensable tools in aeroelastic analysis, providing the means to simplify dynamic models and improve computational efficiency. The Craig Bampton method, with its focus on maintaining physical displacements at contacts, stands out as a valuable approach. Understanding the importance of reduction methods and selecting appropriate ROMs contribute significantly to the success of aeroelastic analyses in diverse engineering applications. However, the inclusion of nonlinear effects through advanced adaptive ROMs is crucial for accurately capturing the dynamic behaviors of modern aerospace structures, especially in systems with significant contact interactions like friction joints.

This exploration into reduction methods draws inspiration from the work of Mauricio Gutierrez Salas [11]. Additionally, insights and perspectives have been shaped by the comprehensive review conducted by Craig Jr. and Chang in their review of the substructuring coupling methods [12].

In adapting and applying these methodologies, the aim is to contribute to the ongoing advancements in aeroelastic analysis and its applications within various engineering domains.

CHAPTER 3

ANALYSIS OF A 10-DEGREES OF FREEDOM LUMPED MODEL

This chapter delves into the dynamic analysis of a 10-degree-of-freedom lumped model, exploring the behavior of interconnected masses and springs subjected to external forces. By defining the system and carefully selecting parameters, we aim to understand its dynamic response to various excitation frequencies. Modal analysis, numerical simulations, and resonance curve analysis provide insights into natural frequencies, mode shapes, and resonant behavior. Additionally, the application of the Craig-Bampton reduction strategy is introduced to efficiently solve complex systems. This exploration offers a detailed understanding of the system's dynamics and showcases effective techniques for analysis and simulation.

3.1 Definition of the model

Consider a 10-degree-of-freedom system depicted in Figure 3.1, where masses m are interconnected by springs of stiffness k. An external force is applied to the first mass.

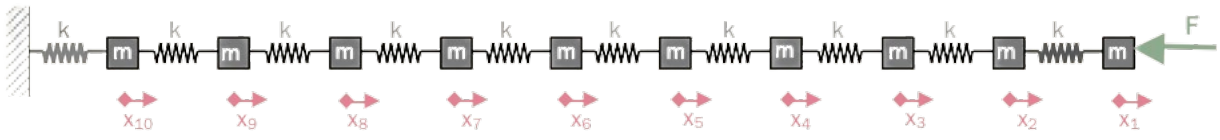

Figure 3.1: System of 10 degrees of freedom.

The equation of motion of the system is given by

$$M\ddot{x} + C\dot{x} + Kx = f(t), \tag{3.1}$$

with the mass M and stiffness K matrices defined as

$$M = \begin{bmatrix} m & 0 & \cdots & 0 \\ 0 & m & \cdots & 0 \\ \vdots & \vdots & \ddots & \vdots \\ 0 & 0 & \cdots & m \end{bmatrix}, \quad K = \begin{bmatrix} k & -k & 0 & \cdots & 0 \\ -k & 2k & -k & \cdots & 0 \\ \vdots & \vdots & \vdots & \ddots & \vdots \\ 0 & 0 & 0 & -k & 2k \end{bmatrix}, \tag{3.2}$$

and the degrees of freedom vector x as

$$x = \begin{pmatrix} x_1 \\ x_2 \\ \vdots \\ x_{10} \end{pmatrix}. \tag{3.3}$$

In the chosen model, the damping matrix C is specifically chosen to be proportional to the stiffness matrix K, represented as

$$C = \xi K. \tag{3.4}$$

This choice for proportional damping is made for a specific reason. When the damping is proportional to the stiffness matrix, it results in a damping matrix that maintains the same eigenvectors as the undamped system. In other words, the normal modes of the undamped system, which occur when $\xi = 0$, remain the same in the damped system.

The choice of the values for the mass m, spring stiffness k and proportional constant ξ is crucial in defining the dynamic behavior of the system. In this case, $m = 1$ is selected to ensure a normalized mass scale, while a value of $k = 10$ allows to set a substantial stiffness level, reflecting a relatively stiff structural configuration. A proportional constant of $\xi = 0.1$ is chosen. This indicates a lightly damped system, allowing for moderate energy dissipation in the presence of damping proportional to the stiffness. These chosen values strike a balance between ensuring numerical stability, capturing realistic physical behavior, and enabling meaningful analysis of the dynamic response of the 10-degree-of-freedom system.

The force vector is defined as

$$f(t) = \begin{pmatrix} 1 \\ 0 \\ \vdots \\ 0 \end{pmatrix} \sin(\Omega t). \tag{3.5}$$

The external force is applied to the first mass for the sake of simplicity and familiarity with the model. This choice serves as a straightforward selection for this lumped model used to gain familiarity with the Craig-Bampton technique.

3.2 Modal analysis

To gain insights into the dynamic characteristics of the 10-degree-of-freedom system, a comprehensive modal analysis is conducted. Modal analysis is a powerful technique employed in structural dynamics to identify the natural frequencies and associated mode shapes of a system.

The process begins by formulating the eigenvalue problem for the system. Considering the equation of motion described in Equation 3.1, setting $f(t) = 0$, the system is assumed to oscillate in the form $x(t) = \phi e^{i\omega t}$, where ϕ is the eigenvector and ω is the angular frequency. Substituting this into the equation leads to the generalized eigenvalue problem

$$(K - \omega^2 M)\phi = 0. \tag{3.6}$$

It is noteworthy that there is no need of the term relative to the damping, $i\omega C$, in this equation. This elimination is justified by the fact that, due to the proportional relationship between stiffness and damping, the normal modes of the undamped system remain unchanged in the damped system.

Solving this eigenvalue problem yields the natural frequencies ω and corresponding mode shapes ϕ of the system. The natural frequencies indicate the rates at which the system tends to oscillate, while the mode shapes represent the spatial distribution of displacements at a particular frequency.

In this case, the software MATLAB is used to compute the eigenvalues and eigenvectors, revealing the modal properties of the 10-degree-of-freedom system.

3.2.1 Natural frequencies and mode shapes

The natural frequencies for different modes are visualized in Figure 3.2, providing a clear representation of the rates at which the system tends to oscillate in each mode.

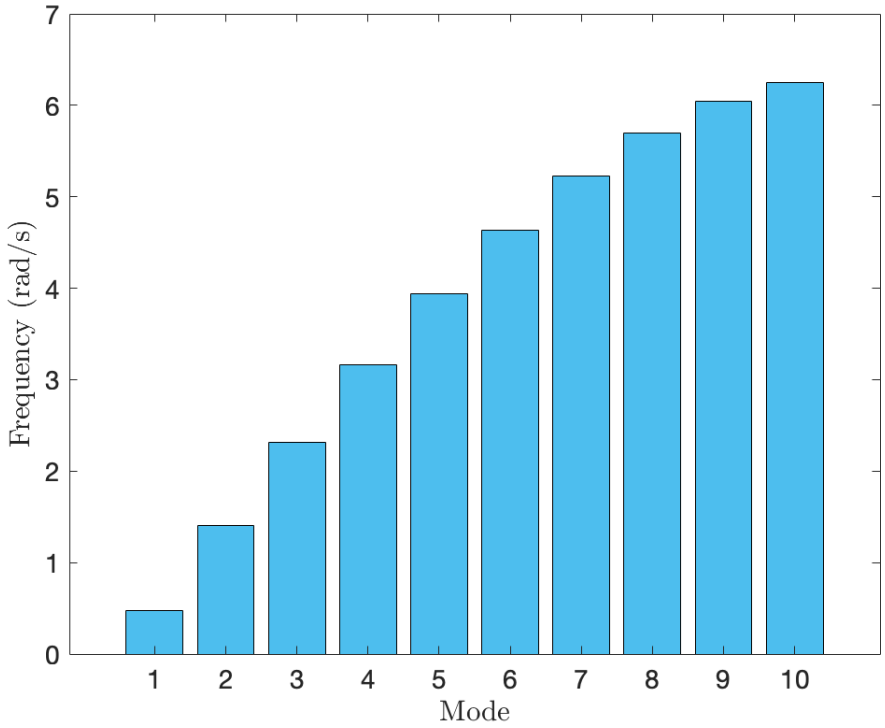

Figure 3.2: Natural frequencies of the 10-DOFs system.

Similarly, Figure 3.3 illustrates the corresponding three first mode shapes, revealing the spatial distribution of displacements at specific frequencies. These mode shapes are essential in understanding the dynamic behavior and deformation patterns of the 10-degree-of-freedom system.

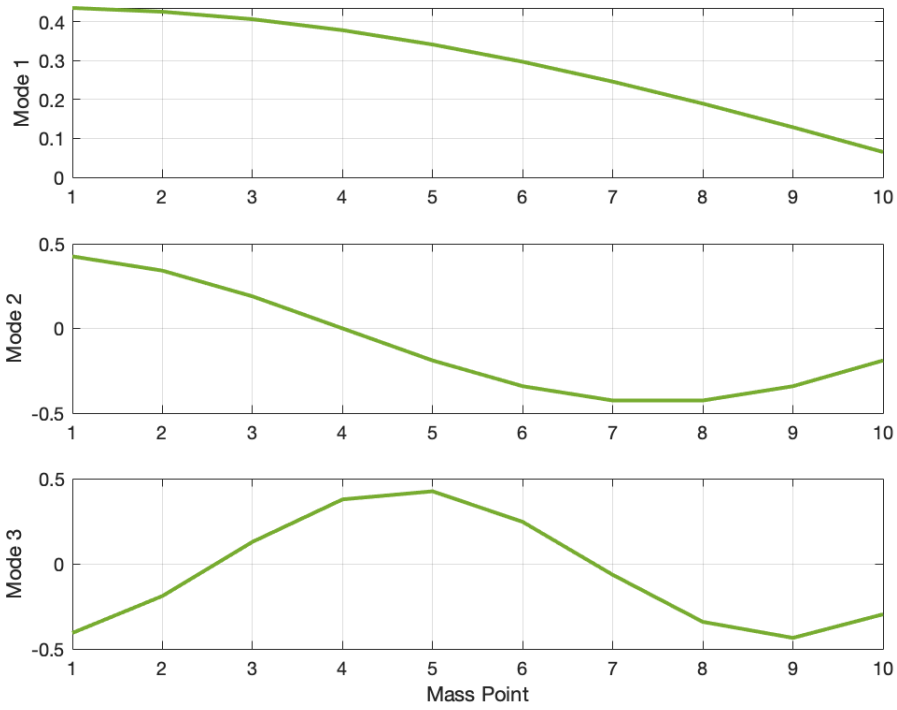

Figure 3.3: Three first mode shapes of the 10-DOF system.

3.2.2 Solution for different excitation frequencies

To comprehensively understand the dynamic response of the 10-degree-of-freedom system, the numerical solution of Equation 3.1 is conducted for different excitation frequencies, denoted by Ω. This meticulous numerical analysis captures the system's evolving displacements, providing valuable insights into its behavior across diverse frequency ranges.

The solution is computed using the ODE45 solver [13] [14], a variable-step Runge-Kutta method for solving Ordinary Differential Equations (ODEs). The solver handles the system of differential equations defined by the matrix M, damping matrix C and stiffness matrix K. The initial conditions for all simulations are :

$$u(0) = \begin{pmatrix} 0 \\ \vdots \\ 0 \end{pmatrix} \qquad \text{and} \qquad \dot{u}(0) = \begin{pmatrix} 0 \\ \vdots \\ 0 \end{pmatrix}, \tag{3.7}$$

meaning the system starts from rest with zero initial displacements and velocities. The excitation force is applied at the first degree of freedom with an amplitude of 1. Using an amplitude of 1 simplifies the analysis and interpretation of the results, allowing for a straightforward comparison of the system's dynamic responses to different excitation frequencies.

The initial conditions are kept the same for both excitation frequencies to ensure a consistent baseline for comparison. This allows us to isolate and observe the effects of the excitation frequency on the system's dynamic response without the influence of differing initial states.

As an illustrative example, the results for two distinct excitation frequencies are presented. First, for $\Omega = 0.4726$ rad/s, the time simulations of displacements are showcased in Figure 3.4, offering a glimpse into the system's dynamic behavior under this specific frequency.

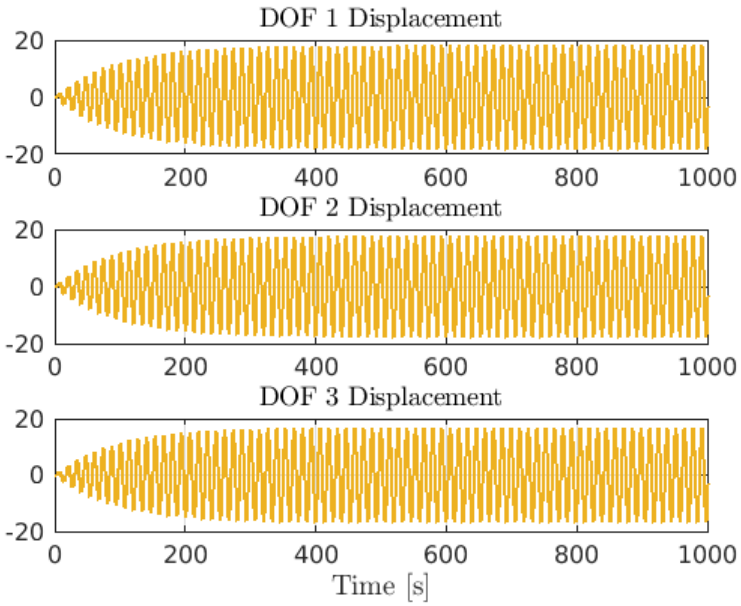

Figure 3.4: Displacements of the first 3 degrees of freedom of the 10-DOFs system for $\Omega = 0.4726$ rad/s.

For a different excitation frequency, specifically $\Omega = 6.2539$ rad/s, the corresponding displacements are presented in Figure 3.5.

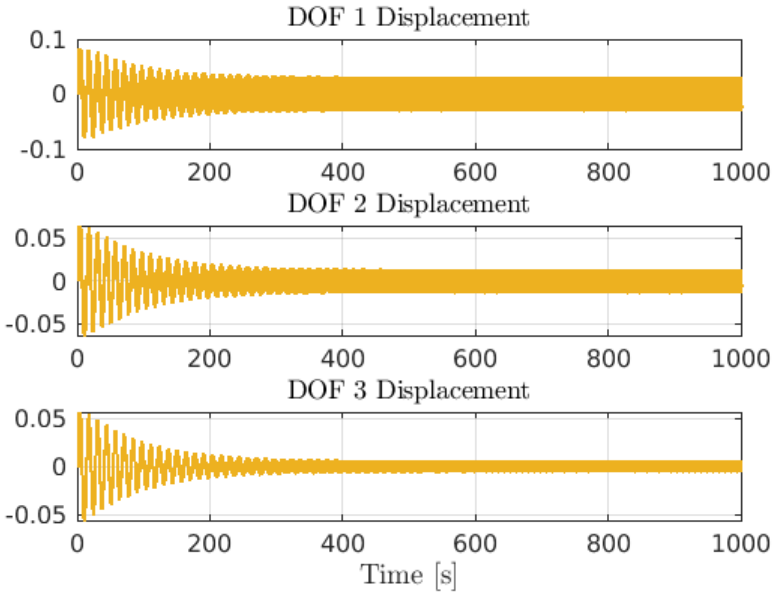

Figure 3.5: Displacements of the first 3 degrees of freedom of the 10-DOFs system for $\Omega = 6.2539$ rad/s.

The observed differences in the displacement plots for the chosen frequencies, $\Omega = 0.4726\ \mathrm{rad/s}$ and $\Omega = 6.2539\ \mathrm{rad/s}$, reveal distinctive dynamic behaviors of the 10-degree-of-freedom system.

For the first frequency of $\Omega = 0.4726\ \mathrm{rad/s}$, the system exhibits an initial phase of small oscillations that progressively increase in amplitude over time, reaching a steady-state periodic solution after approximately 100 seconds. This gradual amplitude buildup is indicative of the system resonating near its first natural frequency. Resonance occurs because the excitation frequency is close to the first natural frequency of the structure, effectively exciting the corresponding mode shape and leading to a sustained response with significant amplitude.

In contrast, the response to the second frequency of $\Omega = 6.2539\ \mathrm{rad/s}$ reveals a different dynamic behavior. Initially, the system undergoes high amplitude oscillations, which then decrease gradually over time. Simultaneously, the period of oscillation shortens, resulting in more frequent oscillations. This behavior is particularly noticeable in the first degree of freedom. The high initial amplitude followed by a decline suggests that the system is initially excited at a higher energy state, but due to damping and modal coupling effects, the energy dissipates, leading to reduced amplitudes.

The excitation frequency of $\Omega = 6.2539\ \mathrm{rad/s}$ is close to the higher natural frequencies of the system, specifically in the range of the 9^{th} and 10^{th} modes. These higher modes typically involve more complex deformation patterns and are associated with higher energy states. The rapid oscillations and denser response indicate that these higher modes are being activated, which is consistent with the observed increase in frequency of the oscillations.

In summary, the distinct responses at different excitation frequencies underscore the sensitivity of the multiple degrees-of-freedom system to resonance phenomena. When the excitation frequency is near a natural frequency, the corresponding mode is predominantly excited, leading to significant amplitude responses. Lower frequency excitation aligns with lower modes characterized by larger, more sustained oscillations. In contrast, higher frequency excitation aligns with higher modes, characterized by more rapid oscillations and complex dynamic behavior. These observations highlight the importance of understanding the modal characteristics of the system for predicting its response under various excitation conditions.

3.3 Resonance curve analysis

Expanding our exploration of the 10-degree-of-freedom system, we delve into the resonance curve analysis.

Critical frequencies, also known as natural frequencies, are the specific frequencies at which the system tends to oscillate naturally when not subjected to damping or external forces. These frequencies are determined through modal analysis. This process involves solving the eigenvalue problem derived from the system's mass and stiffness matrices. The eigenvalues obtained from this analysis correspond to the squares of the natural frequencies.

The plotted resonance curve, presented in Figure 3.6, showcases the system's response amplitudes in proximity to the first resonance frequency. The distinctive peaks and patterns in the curve provide a visual representation of the dynamic behavior at these critical frequencies.

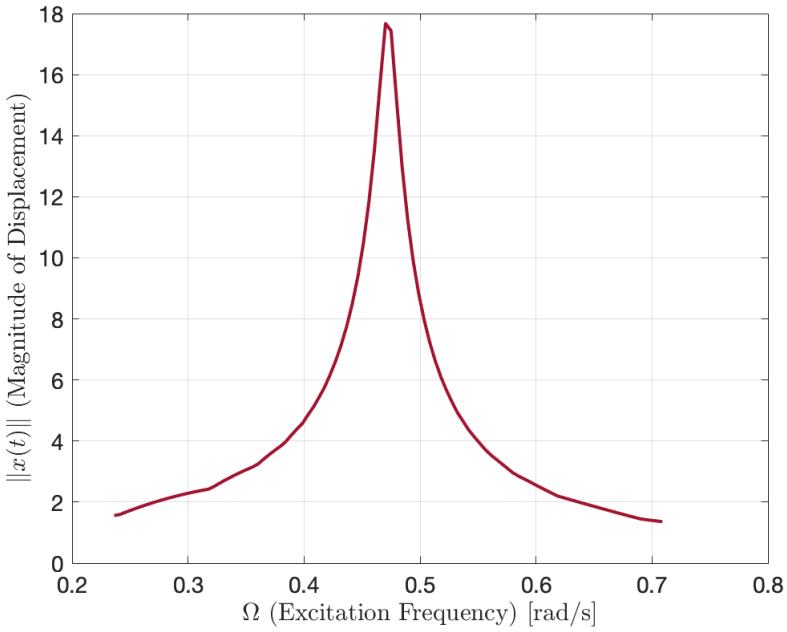

Figure 3.6: Resonance curve near the first resonance frequency.

For a comprehensive understanding of the system's behavior across the entire range of excitation frequencies, the resonance curve is plotted for the complete spectrum of natural frequencies in Figure 3.7.

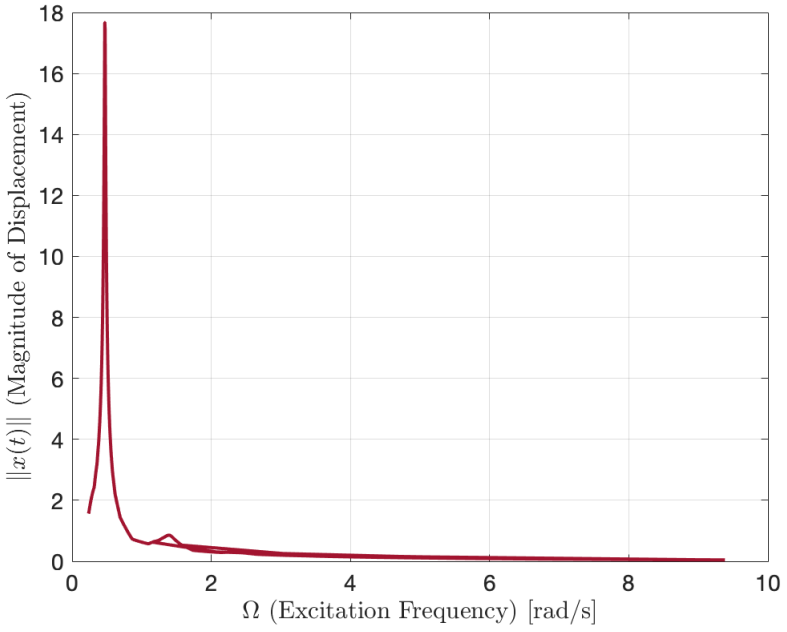

Figure 3.7: Resonance curve for the whole spectrum of excitation frequencies.

This presentation offers a broader insight into the magnitude of displacement across the system's modal frequencies, facilitating a more thorough analysis of its dynamic response.

3.4 Craig-Bampton reduction strategy

In dealing with complex structures, the Craig-Bampton reduction technique becomes an invaluable tool, allowing us to efficiently solve a reduced set of equations while preserving the accuracy of the overall solution. This method proves particularly useful when dealing with a substantial number of degrees of freedom, a common scenario in realistic structures where the number of contact points is significantly smaller than the total degrees of freedom.

3.4.1 Degrees of freedom splitting

To implement the Craig-Bampton reduction, we segregate the degrees of freedom into two distinct categories: elastic degrees of freedom (x_e) and contact degrees of freedom (x_c). For our 10-degree-of-freedom system, this separation can be represented as:

$$x_e = \begin{pmatrix} x_1 \\ x_2 \\ x_3 \\ x_4 \\ x_5 \\ x_6 \\ x_7 \\ x_8 \end{pmatrix} \qquad \text{and} \qquad x_c = \begin{pmatrix} x_9 \\ x_{10} \end{pmatrix}. \tag{3.8}$$

3.4.2 Matrix block splitting

The matrices governing the system dynamics, such as mass M and stiffness K, are also partitioned into blocks to accommodate this degree of freedom division:

$$M = \begin{bmatrix} M_{ee} & M_{ec} \\ M_{ce} & M_{cc} \end{bmatrix} \qquad \text{and} \qquad K = \begin{bmatrix} K_{ee} & K_{ec} \\ K_{ce} & K_{cc} \end{bmatrix}. \tag{3.9}$$

Here, the subscripts "ee," "ec," "ce," and "cc" denote the respective blocks corresponding to elastic-elastic, elastic-contact, contact-elastic, and contact-contact interactions. This block-wise organization allows us to efficiently manipulate and solve reduced sets of equations while preserving the essential interactions within the system.

3.4.3 Application of Craig-Bampton reduction

The next step involves the application of the Craig-Bampton reduction method to the system matrices, with a focus on extracting the elastic modes from the mass matrix (M_{ee}) and stiffness matrix (K_{ee}). Additionally, the procedure incorporates the identification of constraint modes arising from the relationship between elastic degrees of freedom (x_e) and contact degrees of freedom (x_c).

The application of the Craig-Bampton reduction follows the established procedure outlined in the work of R. R. Craig and M. C. C. Bampton [15]. This method ensures the accurate capture of the essential elastic characteristics of the system while effectively handling constraints and reducing the overall computational complexity.

3.5 Comparison of whole and reduced model solutions

To assess the accuracy of the Craig-Bampton (CB) reduced model in comparison to the complete model, resonance curves are examined and compared in Figure 3.8. The plots reveal minimal differences across various numbers of retained modes in the CB method, particularly noticeable at the highest peak. However, these distinctions are nearly negligible for the given model.

Notably, when 8 modes are retained in the CB reduction, the results align with the exact solution. This alignment is intuitive, considering that 8 corresponds to the number of elastic degrees of freedom—a logical maximum for retention in the reduction process. This indicates that, in essence, solving with 8 retained modes in the CB reduction equates to solving the complete structure and not performing any reduction, and as such, the results exactly mirror those obtained for the full model.

The resonance curves depicted in Figure 3.8 showcase the overall consistency between the complete and reduced models, affirming the effectiveness of the Craig-Bampton reduction in preserving system dynamics.

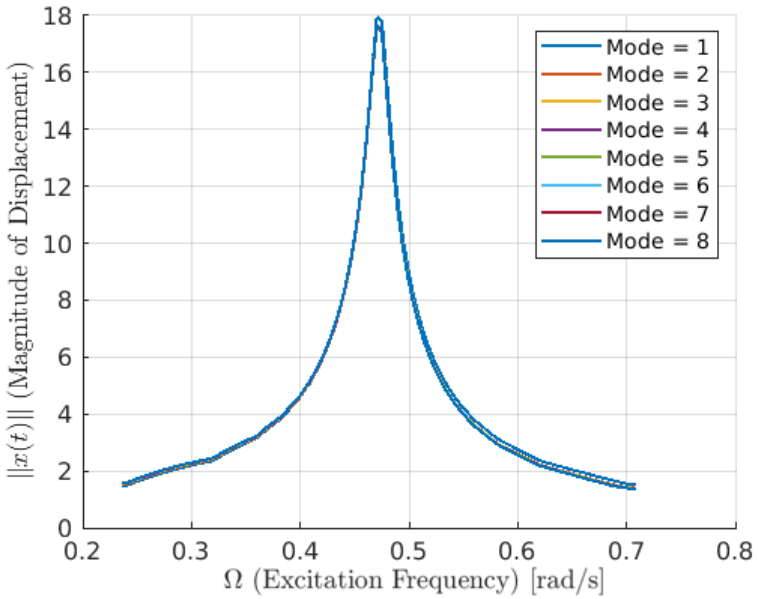

Figure 3.8: Comparison of the resonance curves for the different number of modes retained.

A closer inspection in Figure 3.9 provides a detailed view of the peak region, emphasizing the subtle variations among different mode retention scenarios.

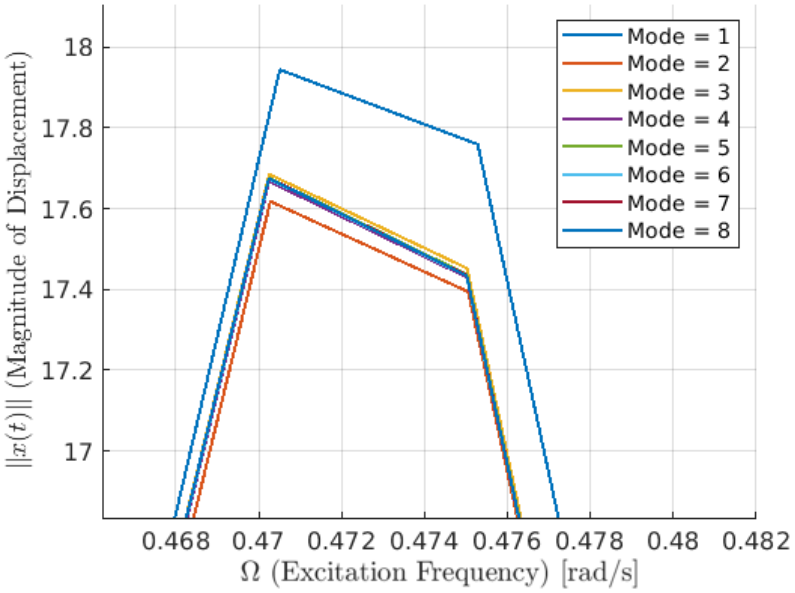

Figure 3.9: Zoom on the peak of the resonance curves.

This comparative analysis demonstrates the reliability and efficiency of the Craig-Bampton reduction method in capturing the essential characteristics of the dynamic system. The negligible differences observed further support the practical application of reduced-order models, offering computational advantages without compromising solution accuracy.

However, it is important to note that these observations are valid primarily when considering excitation frequencies close to the first natural frequency. For such local analyses, the reduced model can effectively approximate the system's behavior. In contrast, for a global analysis encompassing higher frequencies, the reduced model, especially with fewer retained modes, may not capture the complete dynamic behavior accurately.

Figure 3.10 illustrates the resonance curves for the entire spectrum of excitation frequencies. Notably, as shown in Figure 3.11, while the differences between the resonance curves for various numbers of retained modes remain relatively low, they are more pronounced than when focusing solely on frequencies near the first natural frequency.

This limitation is due to the inability of a low-mode reduced model to represent all the resonance peaks inherent to the full system. Therefore, while the Craig-Bampton reduction method is efficient for local analysis near the first natural frequency, caution must be exercised when extending these conclusions to the entire frequency range of the system.

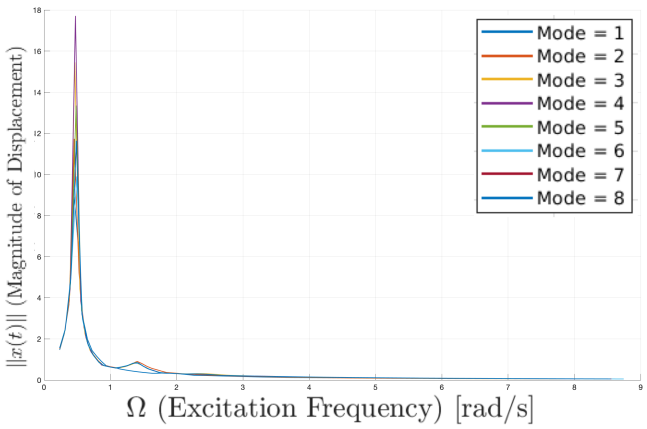

Figure 3.10: Comparison of the resonance curves for the different number of modes retained, for the whole spectrum of excitation frequencies.

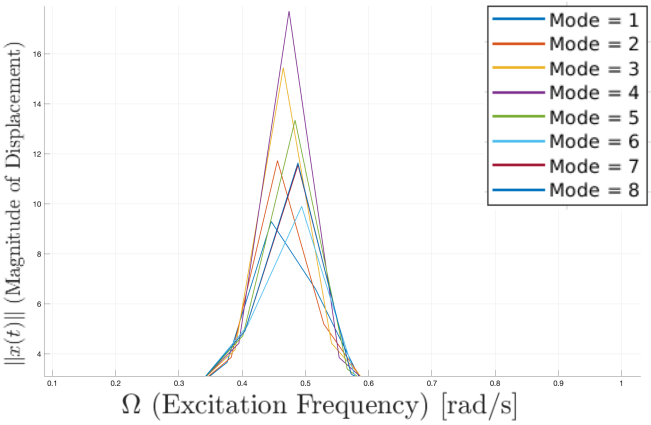

Figure 3.11: Zoom on the peak of the resonance curves, considering the whole spectrum of excitation frequencies.

CHAPTER 4

STUDY OF A MORE DETAILED FINITE ELEMENT MODEL

This chapter provides a comprehensive study of a detailed finite element model focusing on shrouded turbine blades. The chapter integrates both the description of the analysis tools and their application in modeling. By using the CalculiX software, this study aims to analyze the dynamic behavior of these blades, particularly under conditions with and without contact interaction. The chapter also discusses the implementation of a reduction method to improve computational efficiency while maintaining accuracy.

4.1 Description of the Finite Element Model tool

Finite Element Method (FEM) is a powerful numerical technique used for solving complex engineering problems that involve complicated geometries, loadings, and material properties. FEM allows engineers to divide a large, complex system into smaller, more manageable elements and solve for the behavior of each element. The results are then combined to provide an overall solution for the entire system.

In this thesis, the CalculiX software is employed for finite element analysis, offering a comprehensive toolset for building, running, and post-processing finite element models. CalculiX is particularly favored for its capability to handle the intricate geometries of turbomachinery components, making it an ideal choice for analyzing the shrouded blades in this study.

4.1.1 Finite Element Method

The Finite Element Method is widely used across various fields of engineering, including mechanical, aerospace, and civil engineering, among others. It involves discretizing a continuous domain (such as the structure of a turbine blade) into a finite number of smaller elements, each governed by its own set of equations. These elements are then assembled into a global system, representing the entire domain.

For the analysis of the models in this study, a particular focus is placed on addressing challenges like shear locking, which can arise due to the thin, high-aspect-ratio structures and specific loading conditions inherent to turbine blades. To mitigate these issues, the study employs C3D10 elements, which are ten-node tetrahedral elements known for their ability

to accurately capture the complex behaviors of such structures. The node numbering of a C3D10 element follows the convention of Figure 4.1.

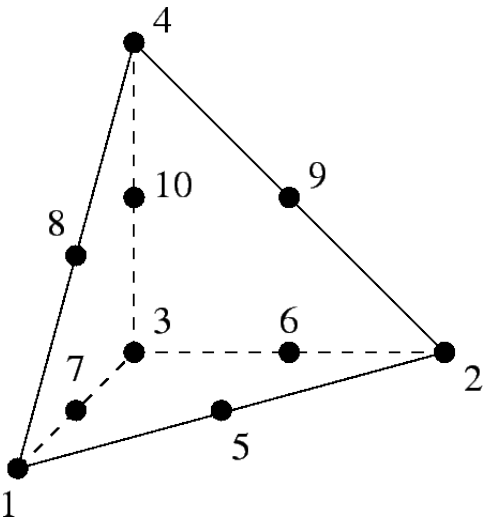

Figure 4.1: Node numbering of a C3D10 element [16].

4.1.2 CalculiX

CalculiX is an open-source FEM software package that includes a solver, CrunchiX, and a pre-postprocessor, GraphiX. It is well-suited for static and modal analysis, which are crucial in understanding the vibrational characteristics of components like turbine blades. In this study, CalculiX is used to perform modal analysis on the bladed-disk sector model, determining the natural frequencies and mode shapes, which are key to avoiding resonant frequencies that could lead to structural failure.

CalculiX 's capability to export full mass and stiffness matrices makes it an ideal tool for comparison with other software like Matlab, ensuring consistency and accuracy in the modal analysis results.

4.1.3 Application of CalculiX in this study

In this thesis, CalculiX is used to create and analyze a finite element model representing the interaction between two shrouded blades. The meshing strategy involves using C3D10 elements to ensure that the model can accurately simulate the complex geometries and behaviors associated with turbine blades. A total of 3526 nodes are used in the model, with a mesh convergence analysis performed to ensure the optimal distribution of elements.

The analysis begins without considering contact interaction between the blades, allowing for an initial understanding of the system's modal behavior. Following this, a fully coupled (or "stuck") model is analyzed to examine the effects of contact interaction on the dynamic response of the system.

4.2 Study of the Finite Element Model

The primary objective of this thesis revolves around the implementation of a reduction method employing two distinct strategies. The initial model serves as a prototype designed to emulate the contact interaction between two shrouded blades. This specific model was chosen because it allows both solids to be fixed in place, which effectively eliminates issues related to rigid body motion.

The depicted model, showcased in Figure 4.2 and implemented using the CalculiX platform, serves as a foundational representation. It lays the groundwork for our investigation into the intricate dynamics of the contact between shrouded blades. In this preliminary stage, the focus is on establishing a robust framework that captures the essential aspects of the system under consideration. This includes the fixation of both solids and the exclusion of rigid body motion challenges.

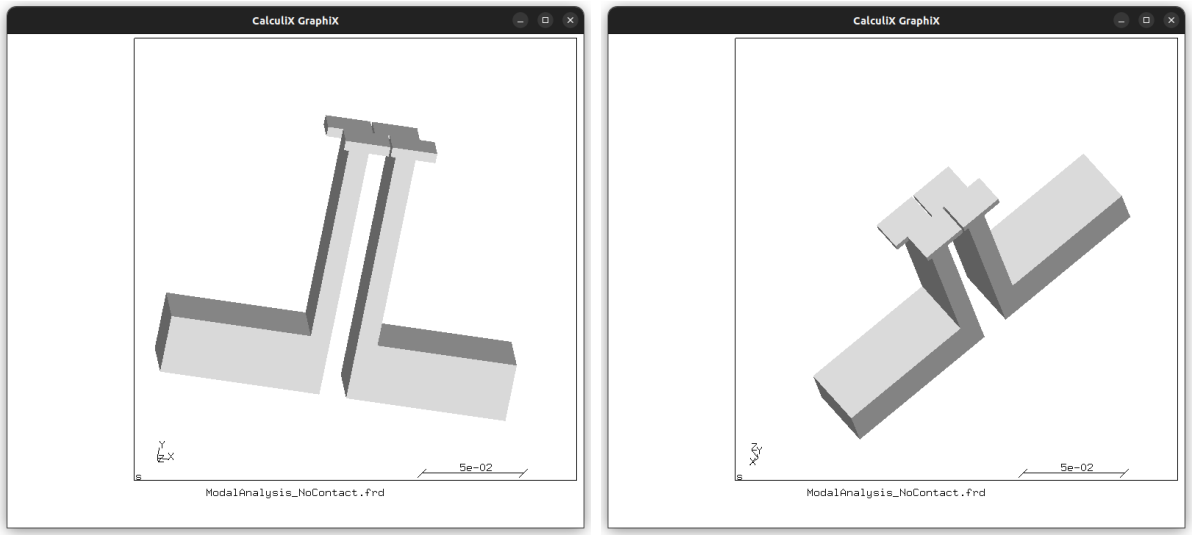

Figure 4.2: Representation of the simplified model on CalculiX.

The meshing strategy introduced in Section 4.1, employing C3D10 elements, plays a crucial role in the prototype model's analysis. Selected for its ability to capture intricate geometries and simulate complex behaviors, the C3D10 element addresses challenges related to shear locking in scenarios involving thin structures and specific loading conditions. This meshing approach ensures a solid foundation for the accurate representation of the prototype model's behavior, laying the groundwork for subsequent analyses in this study. Notably, the mesh consists of 3526 nodes, emphasizing the detailed discretization employed to capture the complexity of the prototype model. A mesh convergence analysis was conducted by S. Rodriguez Blanco in his doctoral thesis [17]. Figure 4.3 visually represents the meshed model using C3D10 elements.

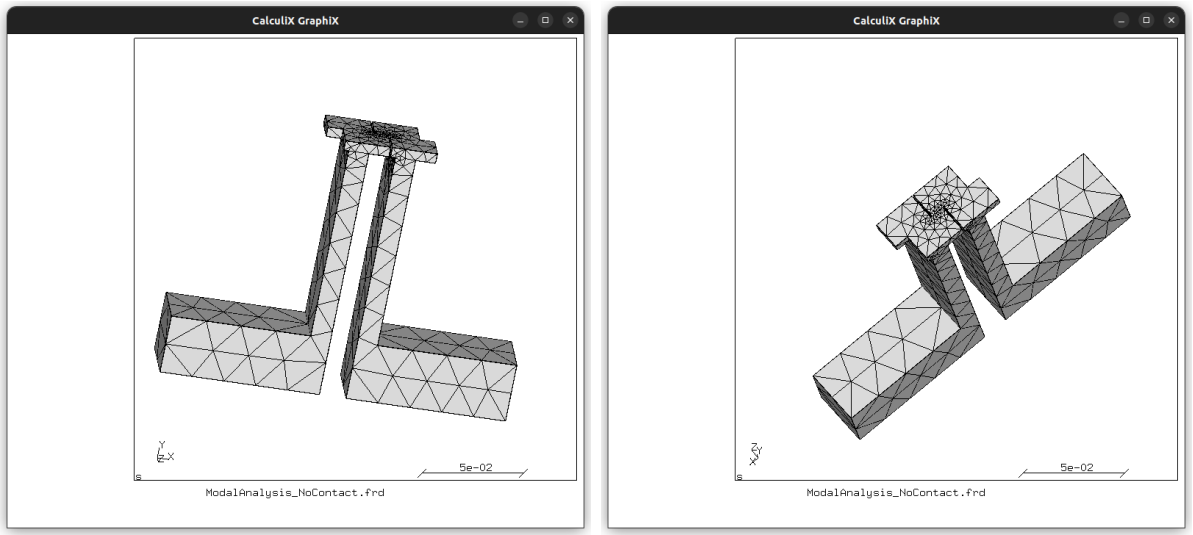

Figure 4.3: Representation of the mesh on CalculiX.

The analysis will be initially conducted without accounting for contact between the two solids, followed by an examination of the fully coupled or "stuck" model.

4.2.1 Boundary conditions

To go further in the analysis, the boundary conditions applied to the finite element model of the two shrouded blades must be defined. Consistent with the study's setup, the degrees of freedom at the bottom of each blade are constrained in both the $x-$ and $z-$directions. This fixation is crucial for eliminating rigid body motion, thereby ensuring that the model accurately reflects the dynamic behavior of the blades under analysis.

Let us denote the DOFs for the displacement at a bottom node of a blade as follows:

- x_{bb} for the displacement in the x direction (1^{st} degree of freedom)
- z_{bb} for the displacement in the x direction (3^{rd} degree of freedom)

The boundary conditions can then be expressed mathematically as :

$$\begin{aligned} x_{bb} &= 0, \\ z_{bb} &= 0, \end{aligned} \tag{4.1}$$

where the subscript "bb" is for "blade bottom".

The first equation ensures that there is no horizontal displacement at the bottom of each blade, while the second equation ensures that there is no vertical displacement at the bottom of each blade.

By fixing the DOFs in these directions, the model ensures stability and accurately simulates the dynamic interactions between the blades without introducing errors associated with rigid body motions. These boundary conditions are applied consistently throughout the study to maintain the integrity and reliability of the simulation results.

The bottom blade nodes are represented in red in Figure 4.4.

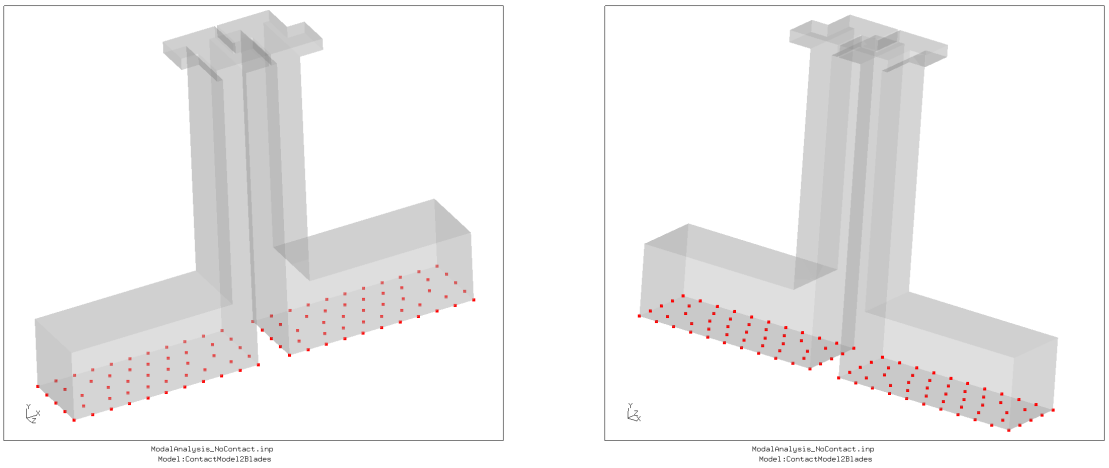

Figure 4.4: Boundary nodes of the model.

4.3 Modal analysis without contact interaction

Following the methodology outlined in Section 3.2, a modal analysis is conducted on the model, considering the absence of contact between the shrouded blades. This analysis is executed using both MATLAB and CALCULIX for comprehensive comparison.

The process involves exporting the full mass and stiffness matrices from CALCULIX to MATLAB. While there is no doubt about the reliability of the eigenvalue solvers in either CALCULIX or MATLAB, the comparison of natural frequencies serves a crucial purpose. It ensures that the implementation of the modal analysis method is consistent and correct across both software platforms. This step verifies the accuracy of the method applied, confirming that the procedure yields consistent results regardless of the computational tool used. This validation is essential to maintain confidence in the analytical approach and to ensure the robustness of the results obtained from the modal analysis.

4.3.1 Relative error between the natural frequencies

The relative error between the natural frequencies obtained from both software tools is calculated using the formula:

$$\epsilon = \frac{|\omega^2_{\text{MATLAB}} - \omega^2_{\text{CALCULIX}}|}{\omega^2_{\text{CALCULIX}}}. \tag{4.2}$$

The resulting relative errors are graphically presented in Figure 4.5, displayed as a bar plot for the first eight modes. Remarkably, the relative error is nearly negligible across these modes, indicating a high degree of consistency between the results produced by the two software platforms. This noteworthy similarity in outcomes underscores the robustness and reliability of both MATLAB and CALCULIX in providing comparable results for the modal analysis under the condition of no contact between shrouded blades.

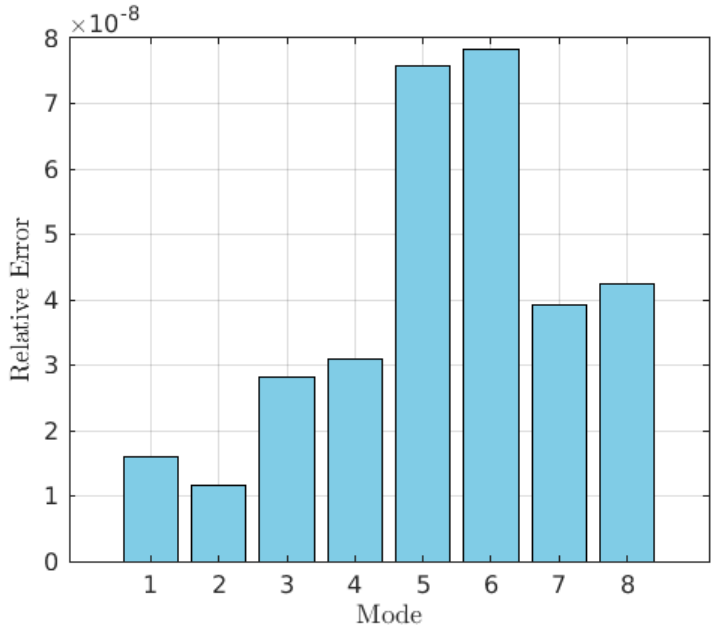

Figure 4.5: Relative error between the natural frequencies obtained with MATLAB and CALCULIX.

4.3.2 Modal Assurance Criterion

Another method to assess the consistency between the two software platforms involves comparing their mode shapes through the Modal Assurance Criterion (MAC) matrix. The MAC matrix is a quantitative measure extensively used in structural dynamics and modal analysis to evaluate the correlation between vibrational mode shapes. This numerical tool gauges how well the shapes of two modes align, providing valuable insights into the agreement between results obtained from different software tools.

The MAC matrix is computed by comparing the modal vectors of distinct modes and is presented as a symmetric matrix of coefficients ranging from 0 to 1. A value of 1 signifies a perfect correlation, indicating identical mode shapes, while a value of 0 implies no correlation between the shapes. This matrix proves to be a crucial tool for the validation and comparison of finite element models as well as experimental modal analysis results.

In the context of this study, the MAC matrix is defined as

$$\text{MAC} = \frac{\phi_{i,\text{MATLAB}}^T M_{tot} \phi_{j,\text{CALCULIX}}}{\sqrt{\phi_{i,\text{MATLAB}} M_{tot} \phi_{i,\text{MATLAB}}} \sqrt{\phi_{j,\text{CALCULIX}} M_{tot} \phi_{j,\text{CALCULIX}}}}. \tag{4.3}$$

Here, $\phi_{i,\text{MATLAB}}$ and $\phi_{j,\text{CALCULIX}}$ represent the mode shapes from MATLAB and CALCULIX, respectively, and M_{tot} is the total mass matrix. The subscripts i and j represent different vibrational modes. Each mode is associated with a set of mode shapes ϕ from the respective software platforms : $\phi_{i,\text{MATLAB}}$ represent the i-th mode from MATLAB and $\phi_{j,\text{CALCULIX}}$ represent the j-th mode from CALCULIX.

This equation allows for a quantitative comparison, further establishing the reliability and consistency of the mode shapes obtained from the two software tools. This additional validation step enhances the overall robustness of the comparative modal analysis.

The MAC matrix, illustrating the correlation between modes from the two software platforms, is depicted in Figure 4.6. Notably, the matrix is represented on a logarithmic scale to provide a clearer insight into the order of magnitude of its values. This logarithmic representation enhances the visualization, allowing for a more nuanced understanding of the relative magnitudes and facilitating the identification of significant correlations among the modes.

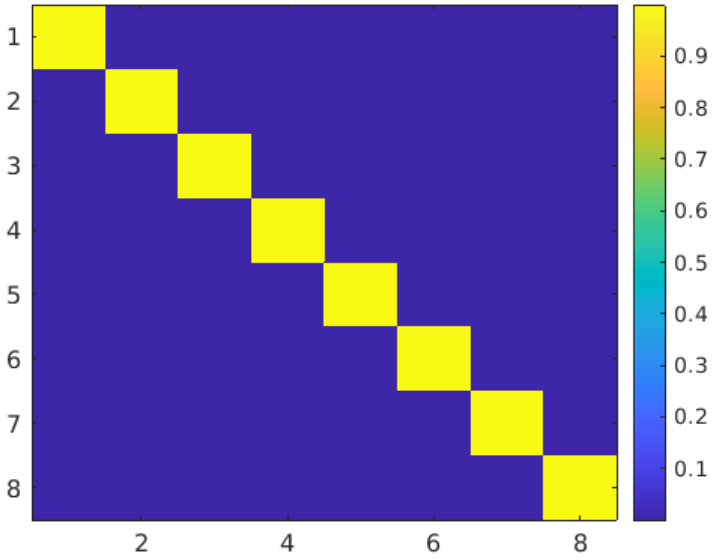

Figure 4.6: MAC matrix comparing modes obtained with MATLAB and CALCULIX.

In this instance, it is evident from the MAC matrix that the values are close to the identity matrix, indicating a high degree of similarity between the modes computed with MATLAB and CALCULIX. This observation further underscores the consistency and agreement between the modal analysis results obtained from the two software tools, validating the accuracy of the simulation outcomes.

4.3.3 Mode shapes on CALCULIX

The mode shapes for the scenario without contact can be visualized using CALCULIX. For instance, Figure 4.7 illustrates the first mode shape corresponding to the first natural frequency. It is worth noting that the associated natural frequency is precisely 633.81 cycles per second, equivalent to 3982.35 radians per second.

In the graphical representation, the mode shape of the first mode is presented at various amplitudes. This variation in amplitudes is intended to provide a comprehensive and representative insight into the deformation patterns of the structure under consideration. Analyzing mode shapes at different amplitudes contributes to a more nuanced understanding of how the structure responds to the first vibrational mode.

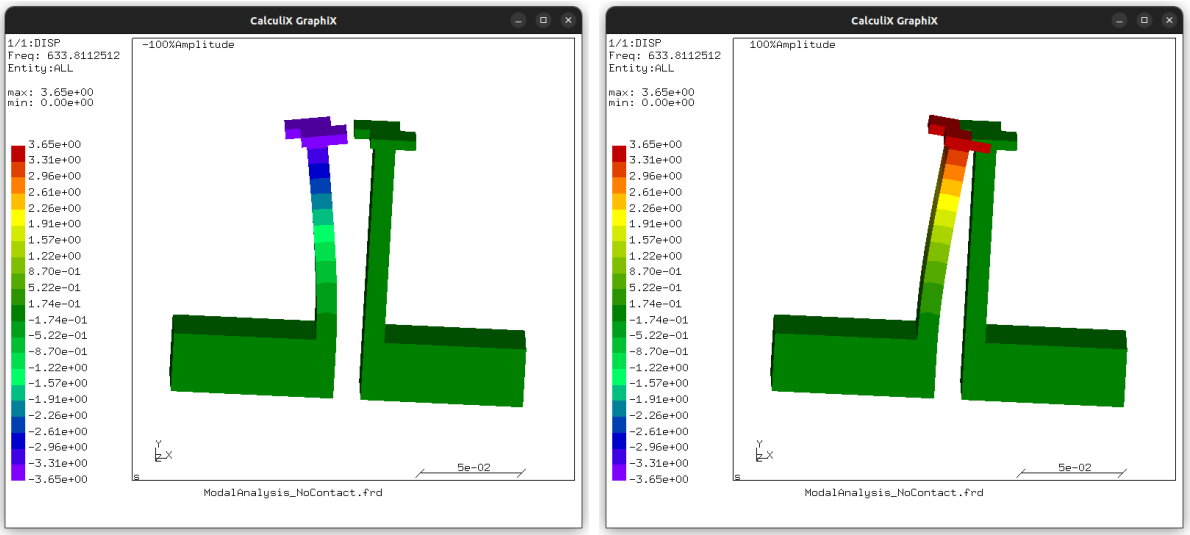

Figure 4.7: Mode shape of the first mode of the model without contact on CalculiX.

4.4 Modal analysis with contact interaction

Considering the same model, four pairs of contacts are defined at the upper regions of the blades. These contact pairs are visually highlighted in Figure 4.8, with distinct colors indicating the left (red) and right (blue) blades.

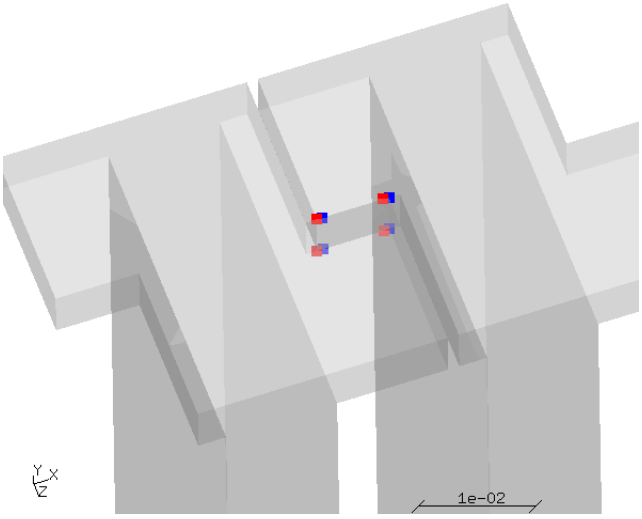

Figure 4.8: Location of the contact nodes within the model.

This strategic placement of contact pairs plays a pivotal role in simulating and analyzing the interaction between the blades. Further exploration and analysis of the model, considering these defined contact pairs, will shed light on the dynamic behavior and structural response under specific contact conditions.

To begin the analysis, the contacts are initially defined as fixed pairs. This imposes the condition:

$$x_{c_1} = x_{c_2}, \tag{4.4}$$

where x_{c_1} and x_{c_2} represent the degrees of freedom corresponding to contact nodes on the left (corresponding to the red dots in Figure 4.8) and right blades (corresponding to the blue dots in Figure 4.8), respectively.

It is crucial to note that this fixed contact condition is only an initial assumption. Throughout the analysis, various contact conditions will be explored to comprehensively understand their effects on the dynamic behavior and structural response of the blades.

4.4.1 Mode shapes on CalculiX

As performed previously, modal analysis is carried out using both MATLAB and CalculiX, and the resulting mode shapes are visualized using CalculiX. To initiate the analysis, it is assumed that the contacts are fixed to each other, implying that the two blades follow the same motion. Figure 4.9 depicts the first mode shape corresponding to the first natural frequency.

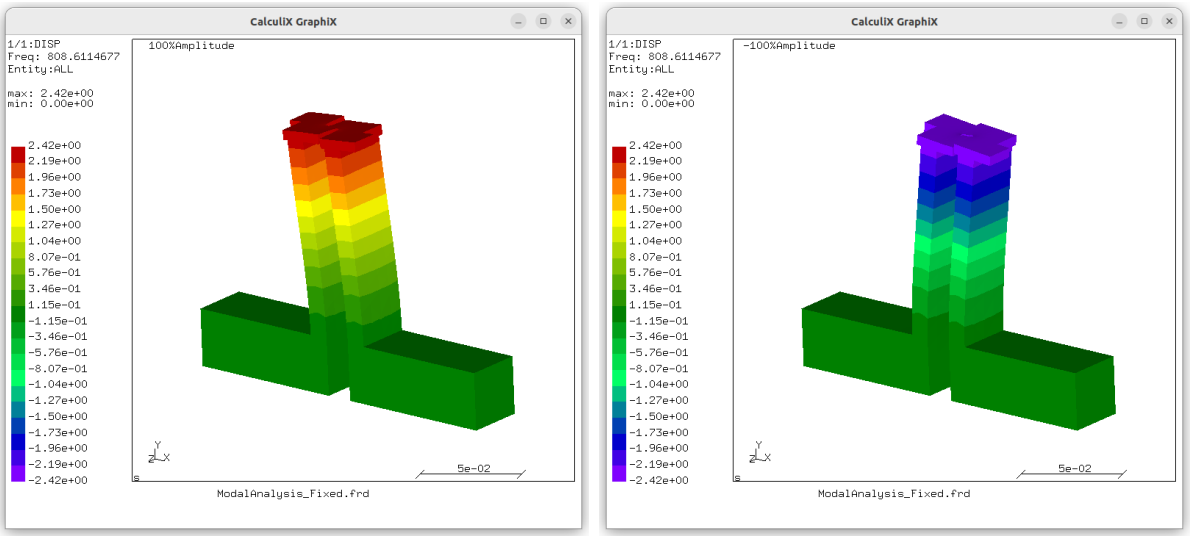

Figure 4.9: Mode shape of the first mode of the fixed model on CalculiX.

4.5 Application of the Craig-Bampton reduction

Given the substantial number of degrees of freedom in the meshed model under consideration, conducting modal analysis computations proves to be time-consuming and highly intricate. To streamline and simplify these calculations, a reduced-order method is employed. Specifically, within the scope of this thesis, the Craig-Bampton method, outlined in Section 2.3, is selected.

The application of the Craig-Bampton method involves two distinct strategies in this study. The first strategy entails implementing a change of variable at the degrees of freedom corresponding to the contact nodes. The second strategy involves applying the reduction method without the incorporation of the aforementioned change of variables. In both cases, it

is imperative to reorder the degrees of freedom, along with the associated mass and stiffness matrices, to adhere to the syntax of the Craig-Bampton method. This requires placing the elastic and contact degrees of freedom in their correct positions within the reordered structure.

This comprehensive approach aims to enhance the computational efficiency of the modal analysis by significantly reducing the number of degrees of freedom while ensuring the accuracy of the results. The subsequent sections will delve deeper into the implementation and outcomes of these two strategies within the framework of the Craig-Bampton reduction.

4.5.1 First strategy: Applying a change of variable

The initial strategy involves implementing a change of variable for the degrees of freedom associated with the contact nodes, as defined in Figure 4.8. This change of variables is expressed as:

$$\begin{aligned} x_+ &= x_{c1} + x_{c2}, \\ x_- &= x_{c1} - x_{c2}, \end{aligned} \tag{4.5}$$

such that

$$\begin{pmatrix} x_{c1} \\ x_{c2} \end{pmatrix} = Q_{\pm} \begin{pmatrix} x_+ \\ x_- \end{pmatrix}. \tag{4.6}$$

Here, x_{c1} and x_{c2} represent specific degrees of freedom corresponding to contact nodes on the left and right blades, respectively. The local transformation matrix is denoted as

$$Q_{\pm} = \begin{bmatrix} 0.5 & 0.5 \\ 0.5 & -0.5 \end{bmatrix}. \tag{4.7}$$

The global change of variable matrix is then defined as

$$R = \begin{bmatrix} I & 0 \\ 0 & Q_{\pm} \end{bmatrix}. \tag{4.8}$$

Considering the simplified equation of motion

$$M \begin{pmatrix} \ddot{x}_e \\ \vdots \\ \ddot{x}_{c1} \\ \ddot{x}_{c2} \end{pmatrix} + K \begin{pmatrix} x_e \\ \vdots \\ x_{c1} \\ x_{c2} \end{pmatrix} = 0, \tag{4.9}$$

this equation can be reformulated using the change of variable matrix

$$R^T M R \begin{pmatrix} \ddot{x}_e \\ \vdots \\ \ddot{x}_+ \\ \ddot{x}_- \end{pmatrix} + R^T K R \begin{pmatrix} x_e \\ \vdots \\ x_+ \\ x_- \end{pmatrix} = 0. \tag{4.10}$$

Note that the force vector considered here is null, so there is no need to apply the change of variable matrix to the right-hand side. However, in the case where a non-zero force vector is considered, the R^T matrix should pre-multiply the force vector.

The introduction of this change of variables serves the purpose of establishing a relationship between pairs of contacts. With x_{c1} and x_{c2} arranged in pairs, the variables x_+ and x_- are defined to capture the summation and subtraction of contacts within a pair.

These newly defined variables, x_+ and x_-, play a crucial role in modeling friction within the system. Notably, friction forces often depend on the relative difference between displacements. Introducing x_- as a variable is particularly convenient for this purpose. The x_- degrees of freedom represent the relative displacements within a contact pair, making them well-suited for capturing the nuanced dynamics associated with friction.

On the other hand, the x_+ degrees of freedom, being linked to the summation of contacts within a pair, can be seamlessly included in the elastic degrees of freedom. Since they do not significantly influence friction forces, incorporating them in the elastic degrees of freedom proves advantageous. This strategic inclusion of x_+ in the elastic dofs results in a reduction in the number of degrees of freedom specifically dedicated to modeling friction, streamlining the overall system representation.

This modification not only enhances the system's ability to model friction accurately but also optimizes the computational efficiency by reducing the number of friction-specific degrees of freedom. Moreover, it aligns with the overarching goal of the study, which is to effectively capture and analyze frictional interactions within the dynamic system.

Once the change of variables is applied, the matrices and vectors of the system need to be reorganized to effectively implement the Craig-Bampton method, adhering to the strategy outlined in Section 3.4.

Convergence study: Relative error analysis with varying number of retained modes in the Craig-Bampton method

To determine the optimal number of modes to be retained in this analysis, one computes the relative error between the natural frequencies obtained for the full model and those derived from the reduced model. In this case, the relative error is expressed as

$$\epsilon = \frac{|\omega_{\text{CB}}^2 - \omega_{\text{tot}}^2|}{\omega_{\text{tot}}^2}. \tag{4.11}$$

Here, ω_{CB} and ω_{tot} represent the first natural frequencies of the reduced and full model respectively. Specifically, ω_{CB} refers to the natural frequencies obtained from the Craig-Bampton reduced model, while ω_{tot} refers to the corresponding natural frequencies from the complete model. The natural frequencies being compared depend on the number of modes retained in the reduced model. As the number of retained modes increases, more natural frequencies are included in the comparison.

This assessment is conducted across varying numbers of modes retained in the Craig-Bampton method. The goal is to identify the smallest number of modes that effectively captures the dynamic behavior of the full model, ensuring the retrieval of identical natural frequencies and modes.

The evolution of the relative error for each mode, as a function of the number of modes retained in the Craig-Bampton method, is illustrated in Figure 4.10. This graph serves as a valuable visualization of how the accuracy of the reduced model progresses with the inclusion of additional modes. Note that the relative error will be represented in logarithmic scale through all this thesis, when represented in function of number of modes retained, in order to have a better idea of the order of m

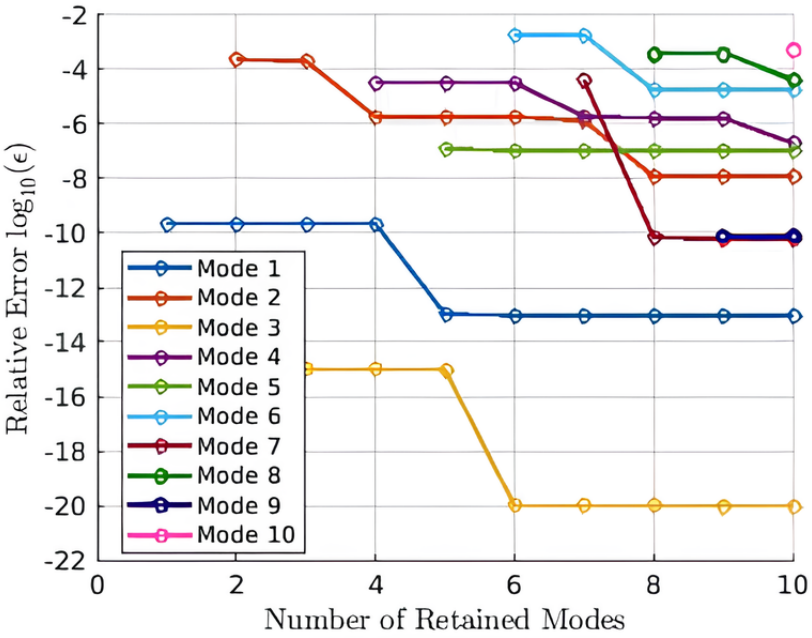

Figure 4.10: Evolution of the relative error between the natural frequencies with the number of modes retained in Craig-Bampton, using the first strategy.

It is important to note that the relative error is computed based on the natural frequencies of both the full and the reduced models. Consequently, the number of values obtained for relative errors is contingent upon the number of modes retained. This comprehensive analysis allows for the identification of an optimal mode retention threshold, striking a balance between computational efficiency and accuracy in representing the dynamic characteristics of the full model.

The graphical representation in Figure 4.10 indicates that even with a small number of modes retained, the relative error is already quite modest. While there might be slight fluctuations in the relative error for certain modes, retaining 8 modes emerges as a compelling compromise. Notably, the relative error values begin to stabilize and reach a sufficiently low threshold with the inclusion of 8 retained modes.

This observation suggests that beyond 8 modes, the reduction in relative error becomes marginal, making the inclusion of additional modes less impactful in terms of improving accuracy. The decision to retain 8 modes strikes a balance between computational efficiency and precision in capturing the dynamic behavior of the full model.

Table 4.1 provides the values of the first 8 natural frequencies obtained for both the full and reduced models.

Table 4.1 Natural frequencies of the full and reduced model using the first strategy.

	Full model	Reduced model
ω_1 [rad/s]	$3.9824 \cdot 10^3$	$3.9824 \cdot 10^3$
ω_2 [rad/s]	$3.9824 \cdot 10^3$	$3.9831 \cdot 10^3$
ω_3 [rad/s]	$9.4793 \cdot 10^3$	$9.4793 \cdot 10^3$
ω_4 [rad/s]	$9.4793 \cdot 10^3$	$9.4940 \cdot 10^3$
ω_5 [rad/s]	$2.4269 \cdot 10^4$	$2.4280 \cdot 10^4$
ω_6 [rad/s]	$2.4269 \cdot 10^4$	$2.4373 \cdot 10^4$
ω_7 [rad/s]	$2.5045 \cdot 10^4$	$2.5045 \cdot 10^4$
ω_8 [rad/s]	$2.5045 \cdot 10^4$	$2.5452 \cdot 10^4$

It is observed that the natural frequencies, and consequently the eigenvalues of the model, are repeated. This repetition arises from the symmetry of the system; both blades being identical, the first natural frequency of the pair is associated with the motion of the left blade, while the second one corresponds to the motion of the right blade.

Analysis of MAC matrix with 8 retained modes

In the context of retaining 8 modes in the Craig-Bampton method, an in-depth exploration is conducted through the examination of the Modal Assurance Criterion matrix. This matrix is derived from the mode shapes of both the full and reduced models, representing a comprehensive assessment of their vibrational correlation.

The MAC matrix is mathematically expressed as

$$\text{MAC} = \frac{\phi_{i,\text{CB}}^T M_{\text{tot}} \phi_{j,\text{tot}}}{\sqrt{\phi_{i,\text{CB}} M_{\text{tot}} \phi_{i,\text{CB}}} \sqrt{\phi_{j,\text{tot}} M_{\text{tot}} \phi_{j,\text{tot}}}}. \tag{4.12}$$

In this equation, $\phi_{i,\text{CB}}$ and $\phi_{j,\text{tot}}$ symbolize the mode shapes from the reduced and full models, respectively, while M_{tot} denotes the total mass matrix. The subscripts i and j distinguish different vibrational modes, each corresponding to a set of mode shapes ϕ from the reduced and full models. Specifically, $\phi_{i,\text{CB}}$ embodies the mode shapes of the i-th mode in the reduced model, while $\phi_{j,\text{tot}}$ encapsulates the j-th mode from the full model.

To ensure compatibility for the multiplication in the formula of the MAC matrix, the $\phi_{i,\text{CB}}$ modes are computed by pre-multiplying the modes obtained for the reduced model by the transformation matrix of Craig-Bampton, given by Equation 2.12.

As mentioned before in Subsection 4.3.2, the MAC matrix values, ranging from 0 to 1, offer insights into the extent of agreement between the two sets of mode shapes. A higher MAC value signifies a more accurate representation of the vibrational behavior in the reduced model compared to the full model.

The structure of the MAC matrix, as illustrated in Figure 4.11, reveals interesting patterns that provide insights into the quality of the modal reduction achieved by the Craig-Bampton method. In a perfect scenario, the MAC matrix would be an identity matrix, indicating an exact match between the modes of the whole and reduced models.

However, in our case, the MAC matrix deviates from a perfect identity, and distinctive blocks of four values each can be identified. This deviation is especially noticeable when considering the diagonal blocks. It is important to note that the matrix is now represented in a non-logarithmic scale to emphasize the details. The diagonal blocks, though not precisely equal to 1, exhibit a close resemblance, with a value of $\frac{1}{\sqrt{2}}$.

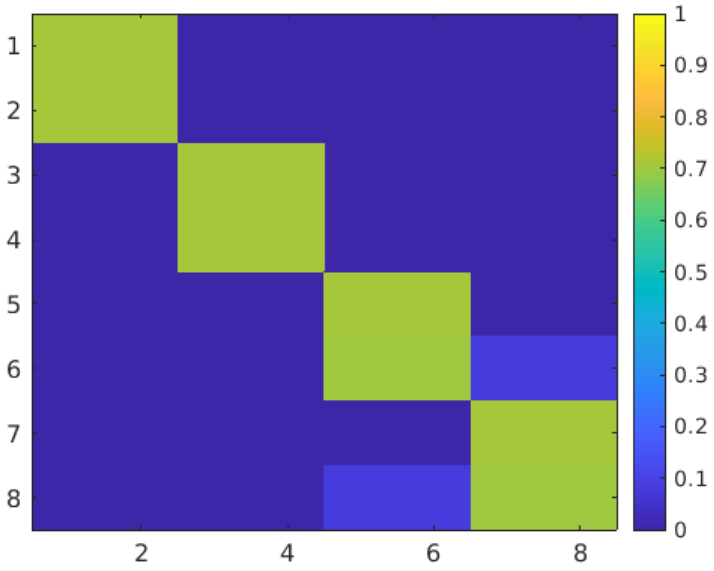

Figure 4.11: MAC matrix comparing modes obtained with the full and reduced model using first strategy.

The value of $\frac{1}{\sqrt{2}}$ is not arbitrary; it originates from the procedure for computing eigenmodes in both MATLAB and CALCULIX, employed consistently for the full model when the change of variables is applied. Let ϕ_1 denote the first mode representing the motion of the left blade and ϕ_2 the first mode representing the motion of the right blade, as illustrated in Figure 4.12.

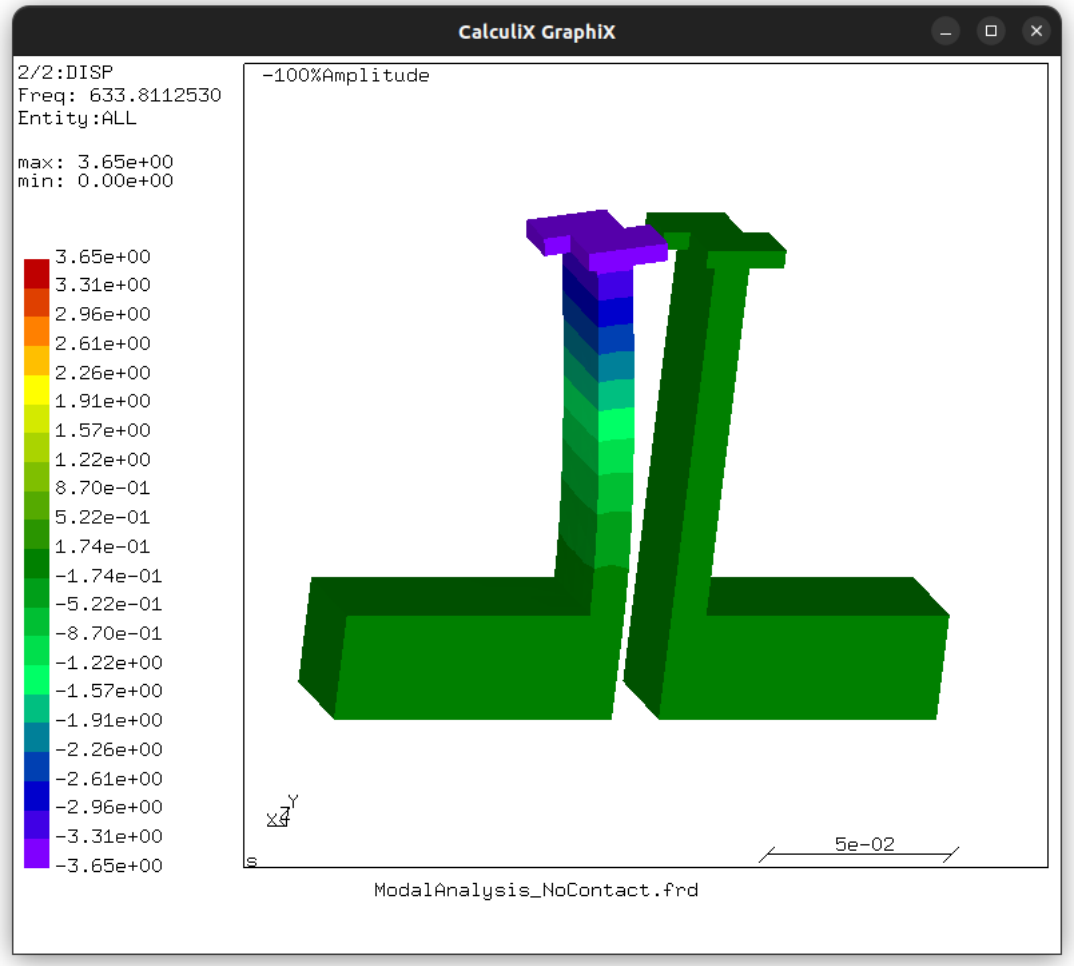

Figure 4.12: Representation of the motion of the left blade.

In this context, it's important to recognize that the condition $x_{c_1} = x_{c_2}$ is not fulfilled, indicating that the contacts between the blades are not fixed to each other in pairs. This is particularly relevant as the analysis focuses solely on the motion of one blade. Given that Figure 4.12 illustrates the motion of the left blade exclusively, fixing the contacts would not be appropriate.

During the modal analysis of the full model, rather than computing ϕ_1 and ϕ_2 separately, MATLAB and CALCULIX compute the combined modes $\phi_1' = \phi_1 + \phi_2$ and $\phi_2' = \phi_1 - \phi_2$. These combined modes capture the motion of the two blades when moving in phase and in antiphase, respectively, as depicted in Figure 4.13.

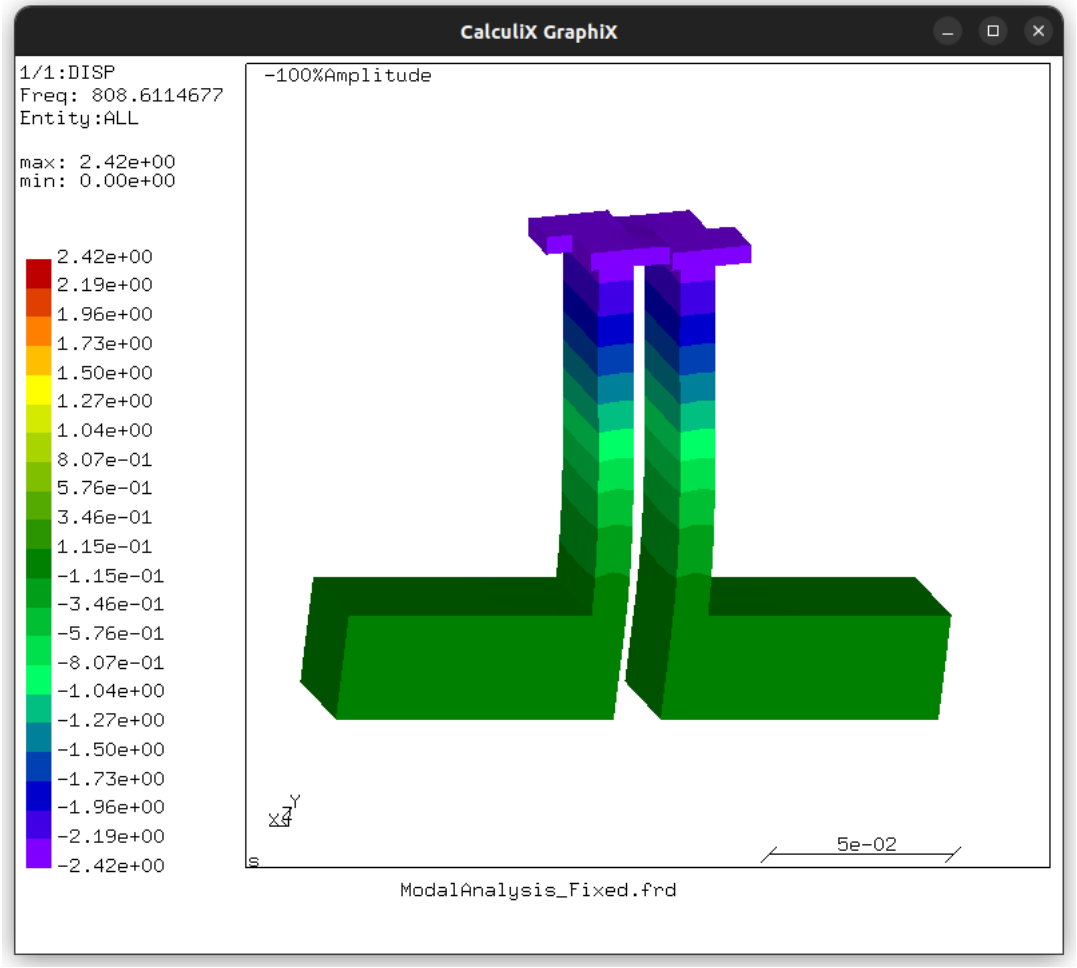

Figure 4.13: Representation of the motion in phase of the coupled blades.

However, in the modal analysis of the reduced model using Craig-Bampton, ϕ_1 and ϕ_2 represent the motion of each blade individually.

When computing the Modal Assurance Criterion matrix using Equation 4.12, it is crucial to note that these are not precisely the same modes being compared. Considering the computation of the element (1,1) of the matrix, the MAC equation can be expressed as

$$\mathrm{MAC}(1,1) = \frac{\phi_1' M_{\mathrm{tot}} \phi_1}{\sqrt{\phi_1' M_{\mathrm{tot}} \phi_1'} \sqrt{\phi_1 M_{\mathrm{tot}} \phi_1}}. \tag{4.13}$$

Given that $\phi_1' = \phi_1 + \phi_2$, this equation can be expanded as

$$\mathrm{MAC}(1,1) = \frac{\phi_1 M_{\mathrm{tot}} \phi_1}{\sqrt{\phi_1' M_{\mathrm{tot}} \phi_1'} \sqrt{\phi_1 M_{\mathrm{tot}} \phi_1}} + \frac{\phi_2 M_{\mathrm{tot}} \phi_1}{\sqrt{\phi_1' M_{\mathrm{tot}} \phi_1'} \sqrt{\phi_1 M_{\mathrm{tot}} \phi_1}}, \tag{4.14}$$

and considering the orthogonality of ϕ_1 and ϕ_2 ($\phi_2 M_{\mathrm{tot}} \phi_1 = 0$), the second term vanishes, simplifying the expression to

$$\mathrm{MAC}(1,1) = \frac{\phi_1 M_{\mathrm{tot}} \phi_1}{\sqrt{\phi_1' M_{\mathrm{tot}} \phi_1'} \sqrt{\phi_1 M_{\mathrm{tot}} \phi_1}}. \tag{4.15}$$

Expanding the first term of the denominator, one gets:

$$\sqrt{\phi_1' M_{\text{tot}} \phi_1'} = \sqrt{(\phi_1 + \phi_2)\, M_{\text{tot}}\, (\phi_1 + \phi_2)} = \sqrt{\phi_1 M_{\text{tot}} \phi_1 + \phi_2 M_{\text{tot}} \phi_2 + 2\phi_1 M_{\text{tot}} \phi_2}. \quad (4.16)$$

Simplifying based on $\phi_1 M_{\text{tot}} \phi_1 = \phi_2 M_{\text{tot}} \phi_2 = 1$ and $2\phi_1 M_{\text{tot}} \phi_2 = 0$, one gets:

$$\sqrt{\phi_1' M_{\text{tot}} \phi_1'} = \sqrt{1 + 1 + 0} = \sqrt{2}. \quad (4.17)$$

Substituting this into the MAC matrix equation yields:

$$\text{MAC}(1,1) = \frac{\phi_1 M_{\text{tot}} \phi_1}{\sqrt{\phi_1' M_{\text{tot}} \phi_1'} \sqrt{\phi_1 M_{\text{tot}} \phi_1}} = \frac{1}{\sqrt{2}\sqrt{1}} = \frac{1}{\sqrt{2}}. \quad (4.18)$$

This result is applicable to all elements (i, i) of the MAC matrix and for elements where the indices satisfy $|i - j| = 1$. The presence of these $\frac{1}{\sqrt{2}}$ values stems from the repetition of eigenvalues discussed in Table 4.1, where identical eigenvalues in a model give rise to linearly dependent eigenvectors.

To mitigate the discrepancies between the full and reduced models arising from the modal analysis methods employed by the softwares, especially when a change of variables is applied, a coupling between the two blades is necessary to ensure a shared motion. The details of this connection will be established and elaborated upon in Section 4.6.

4.5.2 Second strategy : Without applying a change of variable

In contrast to the first strategy, the second approach involves implementing the Craig-Bampton reduction method without introducing a change of variable for the degrees of freedom associated with contact nodes. The decision to pursue this strategy stems from a consideration of certain scenarios where maintaining the original degrees of freedom proves advantageous.

The utility of not implementing a change of variable lies in preserving the inherent degrees of freedom associated with the contact nodes, offering insights into specific structural behaviors. This unaltered representation may be crucial in scenarios where maintaining the original system's configuration is deemed more relevant for a comprehensive understanding of certain dynamic interactions.

Once again, to apply the Craig-Bampton reduction method, it is necessary to reorganize the vectors and matrices, as demonstrated in Section 3.4.

Convergence study: Relative error analysis with varying number of retained modes in the Craig-Bampton method

Once again, the relative error between the natural frequencies derived from the full and the reduced model is computed, using Equation 4.2. This analysis is conducted for various numbers of modes retained in the Craig-Bampton method, aiming to determine the optimal number of modes that accurately captures the dynamic behavior of the full model. The results of this convergence study are illustrated in Figure 4.14. The figure is presented in a similar format to the one used in the first strategy.

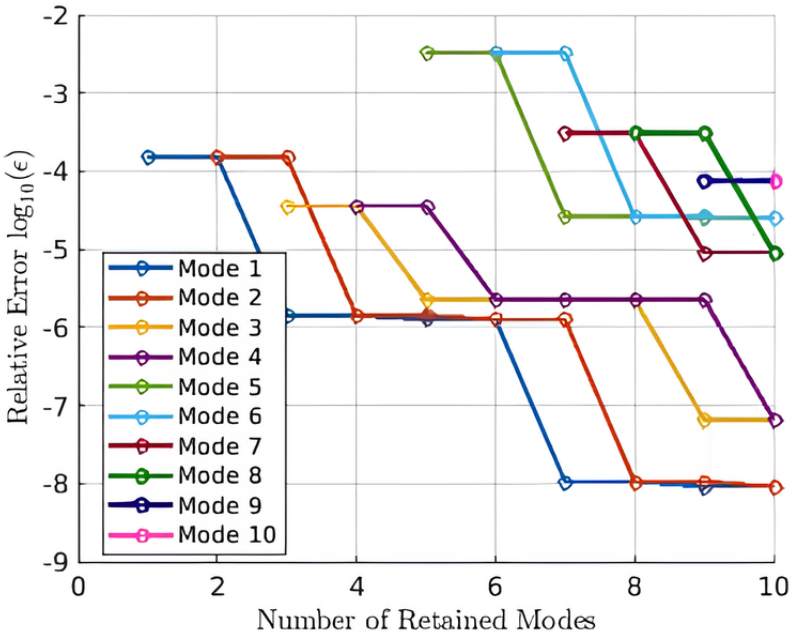

Figure 4.14: Evolution of the relative error between the natural frequencies with the number of modes retained in Craig-Bampton, using the second strategy.

Similar to Figure 4.10, the relative error is observed to be quite small even for a small number of retained modes. For consistency, it is determined that retaining 8 modes in the Craig-Bampton method is sufficient to adequately represent the behavior of the full system.

Table 4.2 presents the values of the first 8 natural frequencies obtained from both the full and reduced models.

Table 4.2 Natural frequencies of the full and reduced model using the second strategy.

	Full model	Reduced model
ω_1 [rad/s]	$3.9824 \cdot 10^3$	$3.9830 \cdot 10^3$
ω_2 [rad/s]	$3.9824 \cdot 10^3$	$3.9830 \cdot 10^3$
ω_3 [rad/s]	$9.4793 \cdot 10^3$	$9.4829 \cdot 10^3$
ω_4 [rad/s]	$9.4793 \cdot 10^3$	$9.4829 \cdot 10^3$
ω_5 [rad/s]	$2.4269 \cdot 10^4$	$2.4391 \cdot 10^4$
ω_6 [rad/s]	$2.4269 \cdot 10^4$	$2.4391 \cdot 10^4$
ω_7 [rad/s]	$2.5045 \cdot 10^4$	$2.5126 \cdot 10^4$
ω_8 [rad/s]	$2.5045 \cdot 10^4$	$2.5126 \cdot 10^4$

Once again, it is evident that the natural frequencies exhibit repetition, and this time, the repetition is exact even in the reduced model. This consistent repetition is attributed to the inherent symmetry of the system. Notably, the precise replication of results in the reduced model is a consequence of solely reordering vectors and matrices to facilitate the application of Craig-Bampton, without the introduction of any change of variables in this particular case.

Analysis of MAC matrix with 8 retained modes

To further support the decision to retain 8 modes in the Craig-Bampton method, the Modal Assurance Criterion matrix is calculated using Equation 4.12. The MAC matrix provides insight into the similarity between the modes obtained from the full and reduced models.

In Figure 4.15, it is evident that the MAC matrix takes the form of an identity matrix, indicating a perfect match between the modes derived from the full and reduced models. This observation aligns with the fact that, in this case, no change of variables is applied. Both the full and reduced models compute modes in an identical manner, reaffirming that retaining 8 modes is sufficient to accurately capture the modes of the full model.

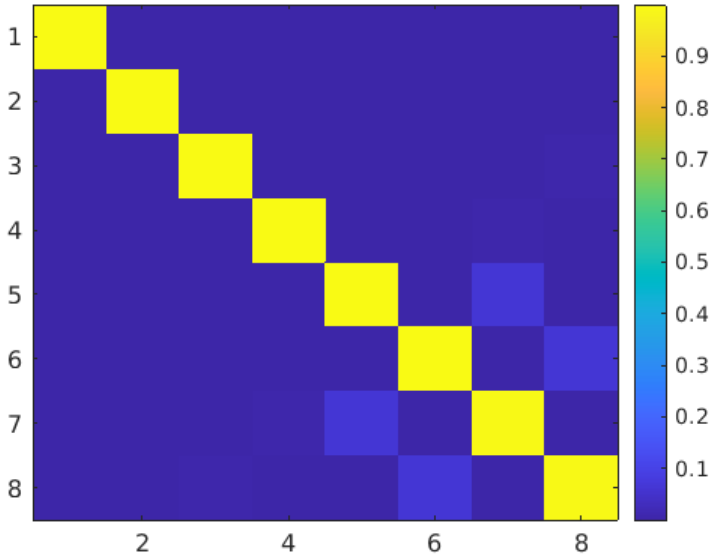

Figure 4.15: MAC matrix comparing modes obtained with the full and reduced model using second strategy.

4.5.3 Comparison between the two strategies

The first and second strategies for applying the Craig-Bampton reduction method were explored to assess their impact on the modal analysis results.

In the first strategy, a change of variable was introduced for the degrees of freedom associated with contact nodes. This change aimed to capture the interaction between pairs of contacts and provide a concise representation of the dynamic behavior.

On the other hand, the second strategy opted to retain the original degrees of freedom associated with contact nodes, without introducing a change of variable. This choice was made to preserve the inherent degrees of freedom and offer insights into specific structural behaviors.

The convergence studies conducted for both strategies revealed that retaining 8 modes in the Craig-Bampton method was sufficient to accurately represent the dynamic behavior of the full model. The relative errors between the natural frequencies for both strategies were found to be small, indicating a high level of accuracy in the reduced models.

When comparing the results, it was observed that the first strategy, involving a change of variable, led to slightly smaller relative errors in some cases. However, the second strategy, without a change of variable, exhibited an exact replication of natural frequencies in the reduced model due to the inherent symmetry of the system.

In terms of the Modal Assurance Criterion matrix, both strategies resulted in an identity-like matrix, confirming an excellent match between the modes of the full and reduced models.

Ultimately, the choice between the two strategies depends on the specific goals of the analysis. The first strategy provides a more concise representation of dynamic interactions between contact nodes, while the second strategy preserves the original degrees of freedom and may be advantageous in scenarios where maintaining the system's configuration is crucial for understanding certain dynamic interactions.

4.6 Enhancement through the addition of springs to the contact nodes

When introducing pairs of contact to the structural components, particularly in realistic scenarios, the presence of friction becomes a noteworthy consideration. However, given that friction is a nonlinear phenomenon and the primary focus of this thesis centers around linear problems, a pragmatic approach is employed to manage the nonlinearity. In order to circumvent the complexities associated with friction, linear springs are strategically incorporated between the contacts of the two blades.

These linear springs serve as a practical solution to address the nonlinearity introduced by friction, providing a simplified yet effective representation within the scope of linear analysis. Their introduction is characterized by their conventional and standard values, ensuring a consistent treatment of the linear interactions between the contact pairs.

With the addition of these linear springs, the pairs of contact are no longer fixed to each other as before. Consequently, the condition defined by Equation 4.4 is not fulfilled anymore, reflecting the altered dynamics resulting from the introduction of these springs.

The choice of strategies in the incorporation of these linear springs is a critical aspect that significantly influences the overall representation of the system. The selection of different strategies can lead to distinct formulations and representations, thereby shaping the analytical framework through which the system's behavior is examined. This nuanced approach allows for a tailored and systematic exploration of the linear aspects of the contact problem, aligning with the overarching linear focus of the thesis.

4.6.1 First strategy

The first strategy involves applying a variable change, as described in Subsection 4.5.1, and reorganizing the vectors and matrices of the system to correctly apply Craig-Bampton. The modified system, incorporating the added springs at the contact nodes, can be expressed as

$$R^T M R \begin{pmatrix} \ddot{x}_e \\ \vdots \\ \ddot{x}_+ \\ \vdots \\ \ddot{x}_- \end{pmatrix} + R^T \left(K + k_{\text{spr}} \begin{bmatrix} 0 \\ \vdots \\ \vdots \\ 0 \\ I \end{bmatrix} \right) R \begin{pmatrix} x_e \\ \vdots \\ x_+ \\ \vdots \\ x_- \end{pmatrix} = 0. \tag{4.19}$$

This comprehensive transformation is instrumental in optimizing the system for enhanced stability and performance. The deliberate inclusion of the added springs at the contact nodes is a strategic move to address and mitigate potential structural challenges.

By investigating the system with two distinct values of k_{spr}—a relatively modest value of 10^2 N/m and a significantly higher value of 10^9 N/m—the resulting natural frequencies are tabulated in detail within Table 4.3.

Table 4.3 Natural frequencies of the full model for different added stiffness values using the first strategy.

	Addition of $k_{\text{spr}} = 10^2$ N/m	Addition of $k_{\text{spr}} = 10^9$ N/m
ω_1 [rad/s]	$3.9824 \cdot 10^3$	$5.0763 \cdot 10^3$
ω_2 [rad/s]	$3.9836 \cdot 10^3$	$9.4798 \cdot 10^3$
ω_3 [rad/s]	$9.4793 \cdot 10^3$	$1.7125 \cdot 10^4$
ω_4 [rad/s]	$9.4798 \cdot 10^3$	$1.8766 \cdot 10^4$
ω_5 [rad/s]	$2.4269 \cdot 10^4$	$2.6542 \cdot 10^4$
ω_6 [rad/s]	$2.4269 \cdot 10^4$	$2.7046 \cdot 10^4$
ω_7 [rad/s]	$2.5045 \cdot 10^4$	$3.9364 \cdot 10^4$
ω_8 [rad/s]	$2.5045 \cdot 10^4$	$4.6113 \cdot 10^4$

This detailed exploration underscores that the natural frequencies corresponding to $k_{\text{spr}} = 10^2$ N/m align closely with those obtained in Table 4.1 for the full model. However, for $k_{\text{spr}} = 10^9$ N/m, the frequency values exhibit a substantial increase, emphasizing the profound impact of the added stiffness on the system's dynamic behavior.

Dynamic exploration: natural frequency evolution with varied spring values

To gain insights into the system's behavior and understand the influence of added spring values on natural frequencies, an exploration of the evolution is conducted. Figure 4.16 illustrates the dynamic changes in natural frequencies as the added spring values to the contact nodes vary. Note that the added spring values are represented on a logarithmic scale to provide a more comprehensive depiction of the frequency evolution.

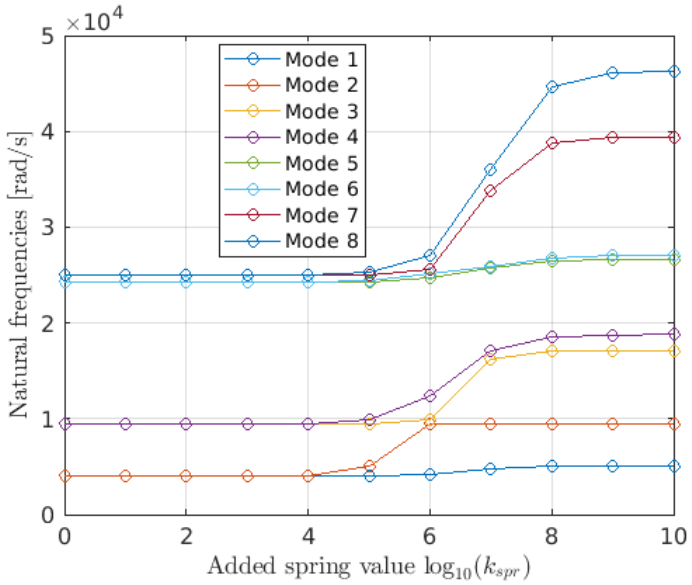

Figure 4.16: Evolution of the natural frequencies with the added spring values, using first strategy.

The plotted results reveal three distinct regions, each providing valuable information about the system's response to differing levels of added spring stiffness:

1. **Soft spring values**
   In this initial region, characterized by low added spring values, natural frequencies remain constant and exhibit a clear pairing pattern. The stability in frequencies during this phase lays the foundation for understanding the baseline behavior of the system under minimal added spring influence.

2. **Intermediate spring values**
   Transitioning into the second region, corresponding to moderate added spring values, a rapid evolution in natural frequencies unfolds. The frequencies demonstrate a dynamic response, evolving swiftly with successive logarithmic increases in the added spring values. This region highlights the system's sensitivity to intermediate levels of added stiffness, suggesting potential critical points.

3. **Hard spring values**
   The final region reveals stabilized yet notably higher natural frequencies associated with higher added spring values. This signifies the saturation of the system's response to increased spring stiffness. Understanding this stabilized behavior is crucial for determining optimal operational conditions and potential structural limits.

The comprehensive exploration of the natural frequency evolution, crucial for understanding the intricate dynamics of the system under varying added spring values, is further enhanced by specifically selecting three values of added spring stiffness. These values, namely 10^2, 10^7, and 10^{10} $\mathrm{N/m}$, are strategically chosen to represent distinct regions within the

frequency evolution. The use of a logarithmic scale in the representation ensures a detailed insight into the system's behavior, offering a nuanced perspective on how it responds to different magnitudes of added spring values.

This detailed examination not only helps in making informed decisions about structural design but also serves as a key element in ensuring stability and mitigating potential resonance or instability issues. By strategically choosing these specific values, one gains a deeper understanding of the system's behavior and can optimize its performance across a broader spectrum of operational conditions.

4.6.2 Second strategy

In the second strategy, we bypass the application of a change of variables, directly implementing Craig-Bampton as outlined in Subsection 4.5.2. The introduction of springs with the same stiffness value k_{spr} results in the following modified system:

$$M \begin{pmatrix} \ddot{x}_e \\ \vdots \\ \ddot{x}_+ \\ \vdots \\ \ddot{x}_- \end{pmatrix} + \left(K + k_{\text{spr}} \begin{bmatrix} 0 \\ \vdots \\ \vdots \\ 0 \\ S \end{bmatrix} \right) \begin{pmatrix} x_e \\ \vdots \\ x_+ \\ \vdots \\ x_- \end{pmatrix} = 0. \tag{4.20}$$

Here, S is a matrix of size $n_{\text{Contact}} \times n_{\text{Contact}}$, where n_{Contact} is the number of degrees of freedom relative to the contact nodes. Matrix S is defined as

$$S = \begin{bmatrix} 1 & -1 & \cdots & -1 \\ -1 & \ddots & & \vdots \\ \vdots & & \ddots & \\ -1 & \cdots & & 1 \end{bmatrix}. \tag{4.21}$$

For the same distinct values of added spring stiffness chosen for the first strategy, namely 10^2 N/m and 10^9 N/m, natural frequencies are determined through modal analysis and presented in Table 4.4.

Table 4.4 Natural frequencies of the full model for different added stiffness values using the second strategy.

	Addition of $k_{\text{spr}} = 10^2$ N/m	Addition of $k_{\text{spr}} = 10^9$ N/m
ω_1 [rad/s]	$3.9824 \cdot 10^3$	$5.0763 \cdot 10^3$
ω_2 [rad/s]	$3.9836 \cdot 10^3$	$9.4798 \cdot 10^3$
ω_3 [rad/s]	$9.4793 \cdot 10^3$	$1.7125 \cdot 10^4$
ω_4 [rad/s]	$9.4798 \cdot 10^3$	$1.8766 \cdot 10^4$
ω_5 [rad/s]	$2.4269 \cdot 10^4$	$2.6542 \cdot 10^4$
ω_6 [rad/s]	$2.4269 \cdot 10^4$	$2.7046 \cdot 10^4$
ω_7 [rad/s]	$2.5045 \cdot 10^4$	$3.9364 \cdot 10^4$
ω_8 [rad/s]	$2.5045 \cdot 10^4$	$4.6113 \cdot 10^4$

It is noteworthy that, in both cases, the computed natural frequencies precisely mirror those obtained with the first strategy (refer to Table 4.3). This outcome is expected, as the

absence of a change of variables does not impact the computation of natural frequencies. According to David C. Lay's book on algebra [18], under similarity transformations, as performed in the first strategy, the eigenvalues (corresponding to the squared natural frequencies) of the transformed system (in this case, using the first strategy) remain the same as those of the original system (in this case, using the second strategy). Therefore, despite the change in variables, the underlying physical characteristics of the system, represented by the natural frequencies, remain unchanged.

Furthermore, it is important to note that the reordering of vectors and matrices for the Craig-Bampton application does not affect the modal analysis either.

The consistency in results reaffirms the robustness of the system's representation, irrespective of the chosen strategy for implementing the Craig-Bampton reduction method with added springs.

It is important to note that this discussion pertains to frequencies computed without applying reduction techniques, and they represent the natural frequencies of the full model. However, when applying Craig Bampton reduction, the perfect mirror between the frequencies is not maintained. The introduction of reduction methods alters the system characteristics, and consequently, the frequencies of the reduced model may differ from those of the original full model.

Dynamic exploration: natural frequency evolution with varied spring values

Once again, delving into a deeper exploration to enrich our understanding of the system's response to varying spring values at the contacts, the natural frequencies are plotted for different values of k_{spr}, maintaining the logarithmic scale. The insights gained from Figure 4.17 reveal the persistence of three distinct regions of natural frequencies, similar to those observed in the first strategy.

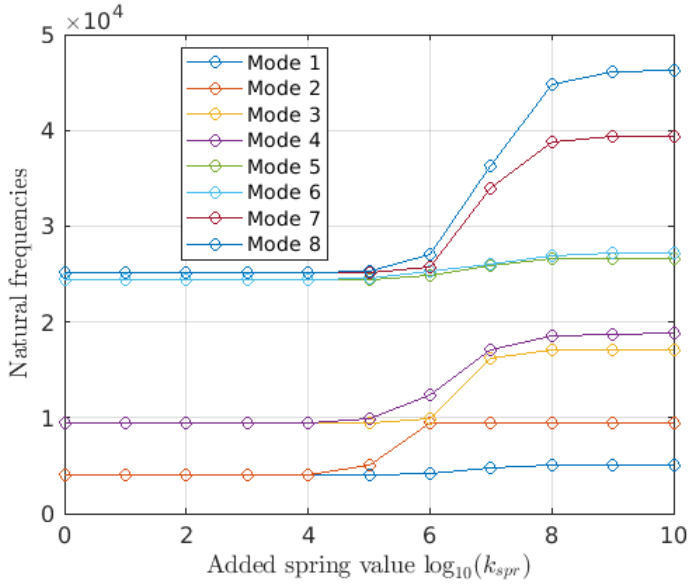

Figure 4.17: Evolution of the natural frequencies with the added spring values, using second strategy.

For the sake of consistency and thorough analysis, the study maintains a consistent

selection of three specific values: 10^2, 10^7, and 10^{10} $\mathrm{N/m}$. These values serve as anchor points throughout the ensuing investigation, allowing for a comprehensive examination of the system's behavior across various added spring strengths. The forthcoming sections will delve into the specific observations and implications derived from this systematic exploration.

4.7 Application of the Craig-Bampton reduction with the added springs at the contact nodes

With the addition of springs at the contact nodes, the Craig-Bampton reduction method is once again applied, using both strategies. The reduction method is employed for three different values of added springs.

4.7.1 First strategy

Convergence study: Relative error analysis with varying number of retained modes in the Craig-Bampton method

A critical aspect of the Craig-Bampton reduction method is determining the optimal number of modes to retain. To achieve this, one performs a convergence study by computing the relative error between the natural frequencies of the full and reduced models. The relative error is evaluated for different numbers of retained modes, providing valuable insights into the accuracy of the reduction method. Figure 4.18 showcases the relative error for an added spring of 10^2 $\mathrm{N/m}$, while Figure 4.19 and Figure 4.20 present the results for added springs of 10^7 $\mathrm{N/m}$ and 10^{10} $\mathrm{N/m}$, respectively.

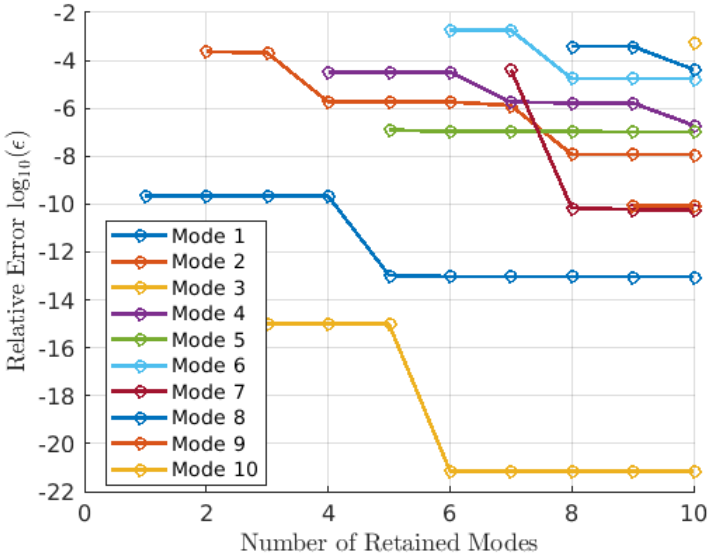

Figure 4.18: Evolution of the relative error between the natural frequencies with the number of modes retained in Craig-Bampton, for an added spring of 10^2 $\mathrm{N/m}$, using the first strategy.

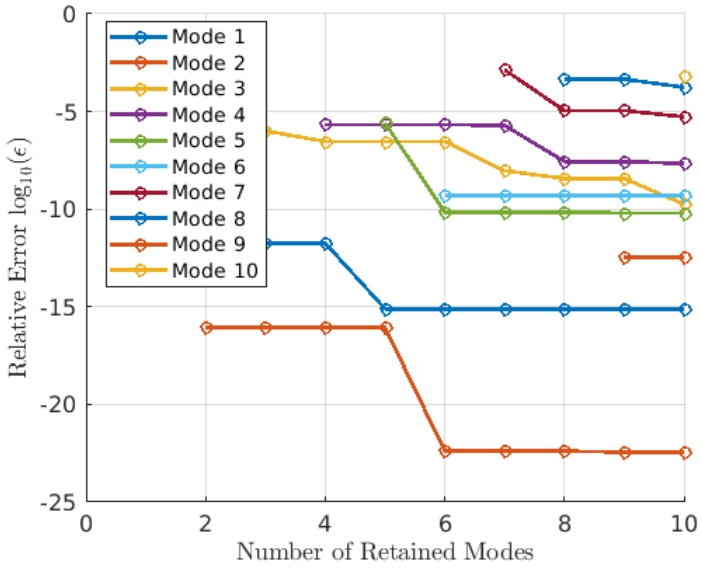

Figure 4.19: Evolution of the relative error between the natural frequencies with the number of modes retained in Craig-Bampton, for an added spring of 10^7 N/m, using the first strategy.

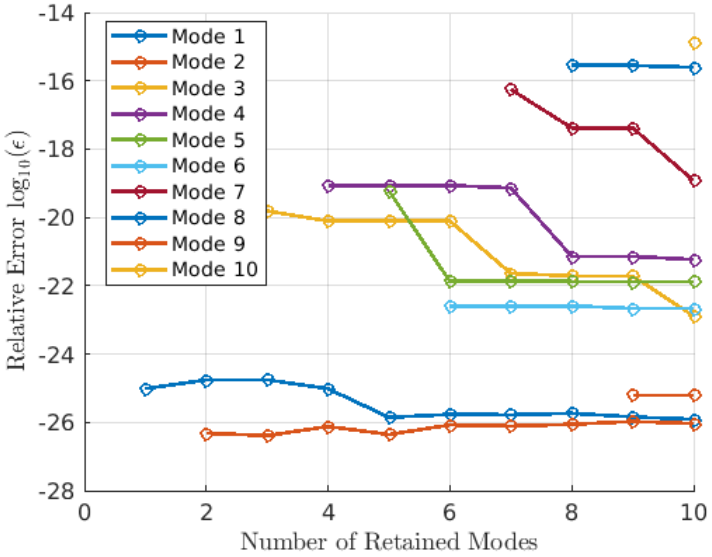

Figure 4.20: Evolution of the relative error between the natural frequencies with the number of modes retained in Craig-Bampton, for an added spring of 10^{10} N/m, using the first strategy.

Across all three scenarios, it can be inferred that maintaining a modest number of 6 modes in the reduction method appears to be adequate for capturing the essential characteristics of the full model. This observation is substantiated by the minimal relative error observed between the natural frequencies for each case. Striking this optimal balance ensures a computationally efficient yet accurate representation of the system's dynamics, laying a robust foundation for further in-depth analysis and design considerations.

However, it is noteworthy that the optimal number of modes to be retained might exhibit slight variations depending on the value of the added springs at the contact nodes. To delve further into the analysis and enhance precision, the Modal Assurance Criterion matrix will be computed. This additional step aims to provide a more nuanced understanding of the number of modes to be retained for the three distinct cases, ensuring a thorough exploration of the system's dynamic behavior.

Analysis of MAC matrix for different number of modes retained

The Modal Assurance Criterion matrix can now be visualized for various numbers of modes retained in the Craig-Bampton method, corresponding to different values of the added springs. This matrix provides insights into the convergence of the optimal number of modes to be retained in the reduction method for the three distinct cases.

In Figure 4.21, it is noticeable that for an added spring value of 10^2 N/m, the MAC matrix tends to approach a perfect identity matrix starting from 10 modes retained in the Craig-Bampton method. However, it is essential to note that it does not precisely become an identity matrix. This behavior aligns with the explanation provided in Subsection 4.5.1, indicating that the stiffness between the contacts is not sufficiently high. As a result, the two blades may still exhibit slightly independent motions, contributing to the observed behavior in the MAC matrix.

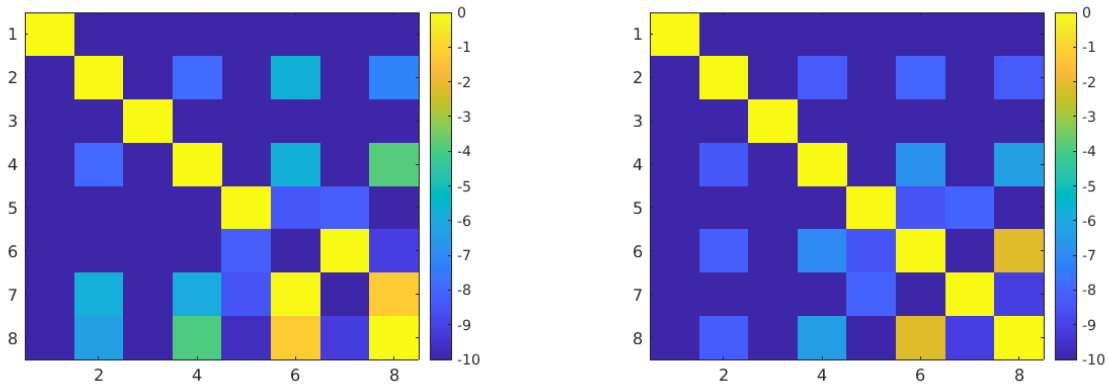

(a) MAC matrix for 6 modes retained.

(b) MAC matrix for 10 modes retained.

Figure 4.21: MAC matrix comparing modes obtained for the full and reduced model for different number of modes retained, for an added spring of 10^2 N/m, using first strategy.

In Figure 4.22, corresponding to an added spring value of 10^7 N/m, the MAC matrix exhibits promising behavior as it begins to approach a perfect identity matrix from 6 modes retained in the Craig-Bampton method. The convergence towards an identity matrix becomes even more apparent with 10 modes retained. This improved behavior can be attributed to the higher stiffness introduced by the added spring, which significantly diminishes the likelihood of the two blades exhibiting independent motions. The increased stiffness fosters a more coupled motion between the blades, contributing to the observed convergence and enhanced agreement in the MAC matrix. However, some off-diagonal elements still persist at an order of magnitude of 10^{-3}, which is not negligible. This persistence is due to the mid-range added

spring values in Figure 4.16, where the natural frequencies evolve rapidly with increasing order of magnitude.

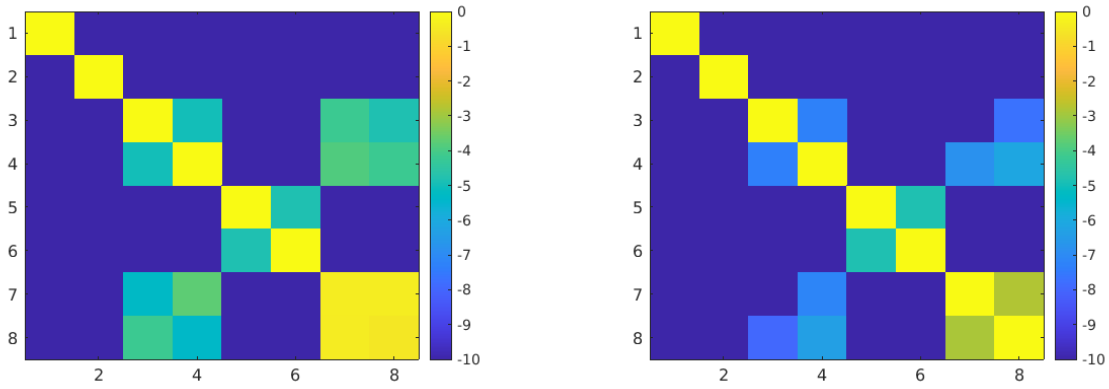

(a) MAC matrix for 6 modes retained.

(b) MAC matrix for 10 modes retained.

Figure 4.22: MAC matrix comparing modes obtained for the full and reduced model for different number of modes retained, for an added spring of 10^7 N/m, using first strategy.

In Figure 4.23, corresponding to an added spring value of 10^{10} N/m, the MAC matrix demonstrates a distinctive behavior. It already approaches a perfect identity matrix starting from 6 modes retained in the Craig-Bampton method. This observation signifies that the substantial stiffness introduced by the added spring is highly effective in coupling the motion of the two blades. The large magnitude of the added spring value ensures a robust connection between the blades, resulting in a synchronized motion that is accurately captured even with a relatively modest number of retained modes. The convergence towards a perfect identity matrix in this case emphasizes the potency of the added spring in minimizing independent motions and fostering a more integrated response from the structural system.

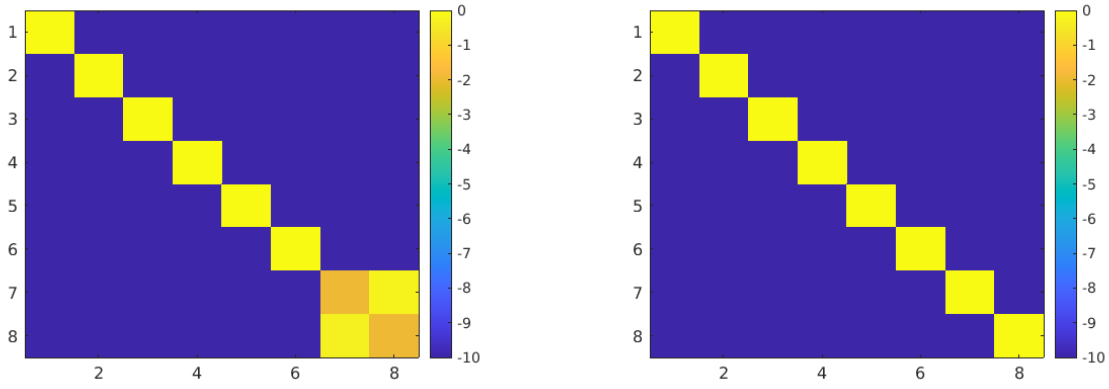

(a) MAC matrix for 6 modes retained.

(b) MAC matrix for 10 modes retained.

Figure 4.23: MAC matrix comparing modes obtained for the full and reduced model for different number of modes retained, for an added spring of 10^{10} N/m, using first strategy.

Mode shapes on CalculiX

To provide a comprehensive visual representation of the system's mode shapes, an analysis is conducted using MATLAB for modal analysis, and the results are then translated into files compatible with CalculiX for visualization. This approach enables a detailed exploration of the first mode shapes corresponding to different values of added springs at the contact nodes.

In Figure 4.24, the first mode shape is presented, aligning with the first natural frequency. A spring of stiffness 10^2 N/m is applied at the contact nodes, and the mode shape is depicted at varying amplitudes to ensure a thorough representation of the motion of the blades.

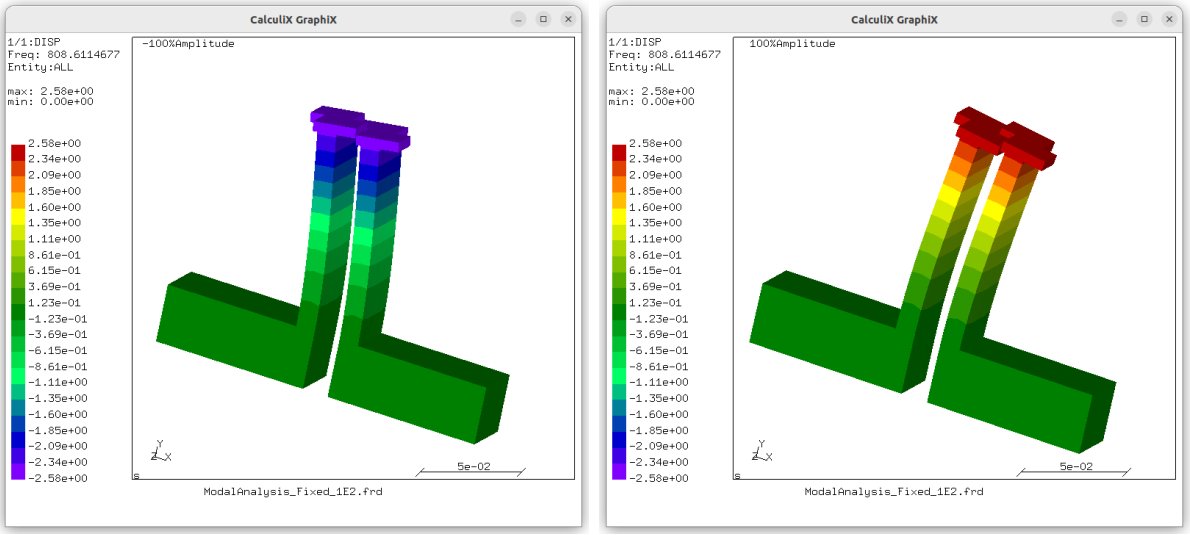

Figure 4.24: Mode shape of the first mode of the model with an added spring of 10^2 N/m on CalculiX, using first strategy.

Moving to Figure 4.25, the focus shifts to the first mode shape associated with an added spring value of 10^7 N/m. This figure not only illustrates the mode shape but also highlights the system's response to a higher stiffness scenario, contributing to a more detailed understanding of the structural dynamics.

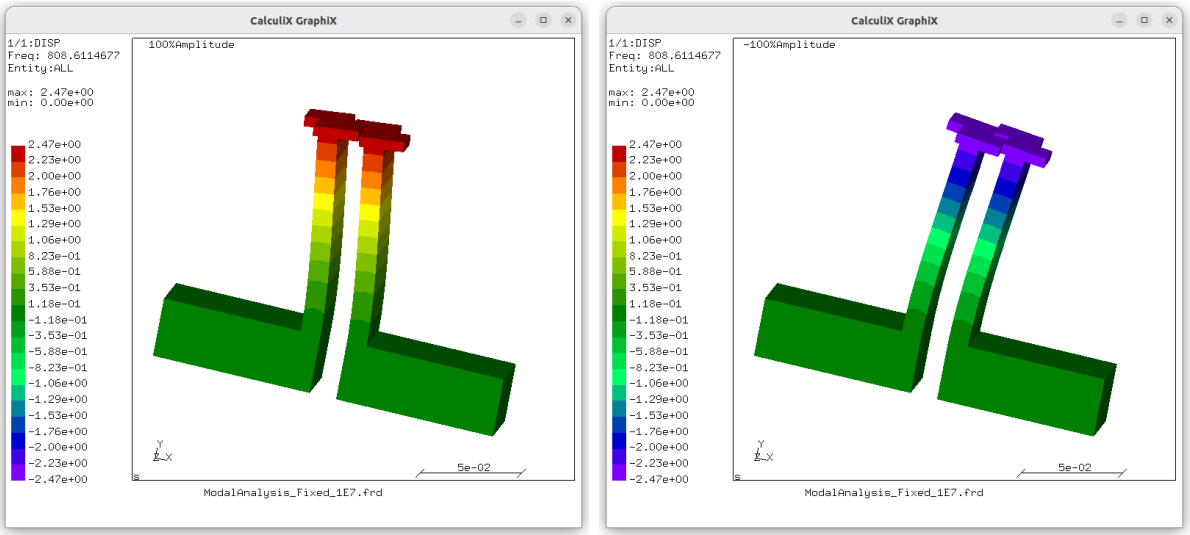

Figure 4.25: Mode shape of the first mode of the model with an added spring of 10^7 N/m on CalculiX, using first strategy.

Continuing the exploration in Figure 4.26, the first mode shape is presented for the most substantial added spring value of 10^{10} N/m. This figure not only captures the mode shape but also signifies the system's behavior under an extremely high stiffness condition.

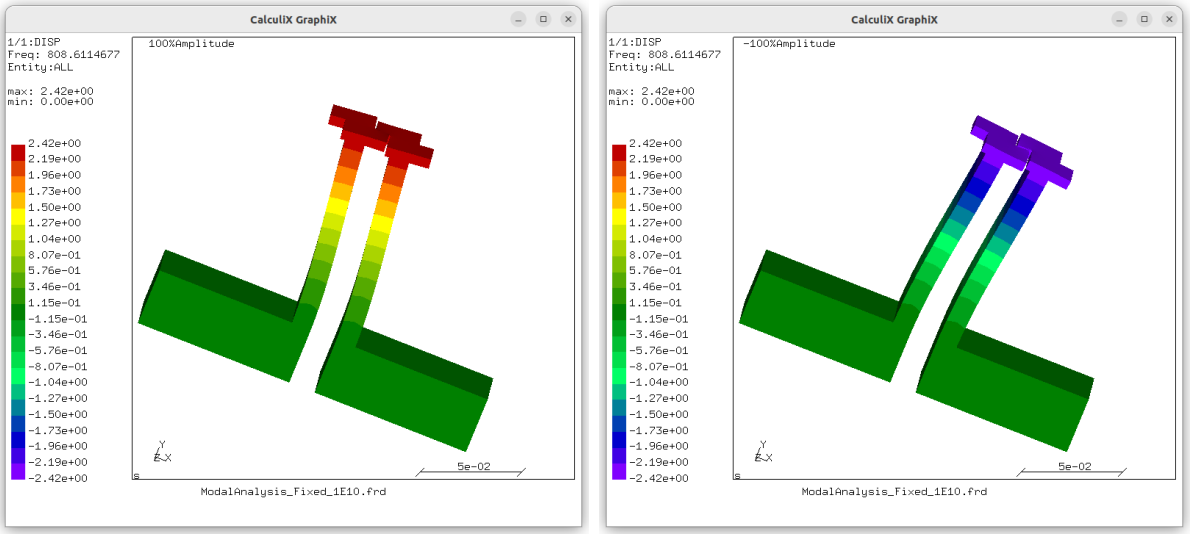

Figure 4.26: Mode shape of the first mode of the model with an added spring of 10^{10} N/m on CalculiX, using first strategy.

These visual representations serve as invaluable tools in understanding the intricate dynamics of the system under varying added spring values, allowing for a detailed examination of mode shapes and their corresponding responses.

4.7.2 Second strategy

Convergence study: Relative error analysis with varying number of retained modes in the Craig-Bampton method

As mentioned before, an essential consideration in the implementation of the Craig-Bampton reduction method lies in determining the optimal number of modes to retain. Once again, a convergence study is conducted, wherein the relative error between the natural frequencies of the full and reduced models is systematically computed.

Figure 4.27 illustrates the convergence study results for the second strategy, specifically focusing on the relative error associated with an added spring of 10^2 N/m. Subsequently, Figure 4.28 and Figure 4.29 delve into the outcomes for added springs of 10^7 N/m and 10^{10} N/m, respectively. This comparative analysis aims to draw insights specific to the second strategy, ensuring a nuanced examination of the reduction method's performance across different scenarios.

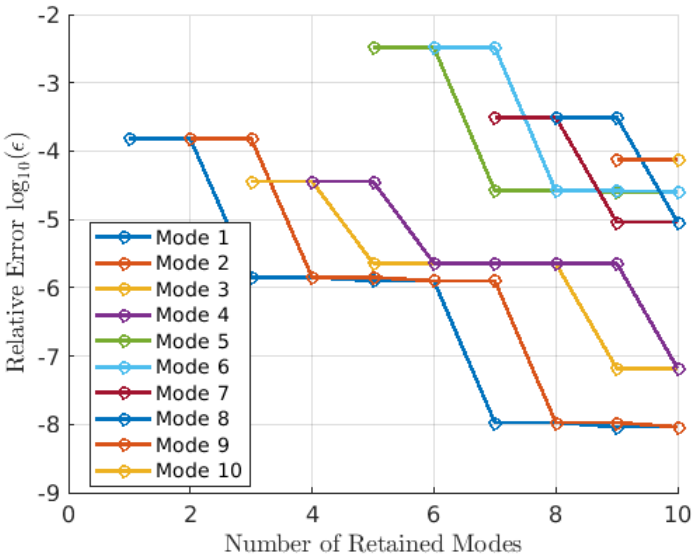

Figure 4.27: Evolution of the relative error between the natural frequencies with the number of modes retained in Craig-Bampton, for an added spring of 10^2N/m, using the second strategy.

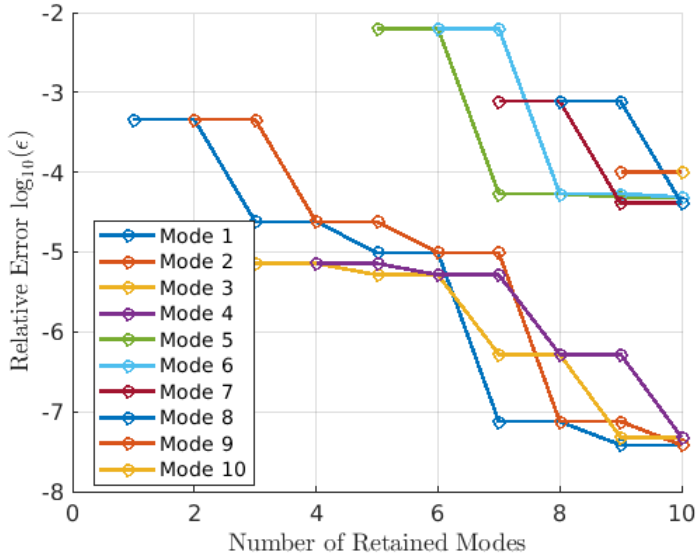

Figure 4.28: Evolution of the relative error between the natural frequencies with the number of modes retained in Craig-Bampton, for an added spring of $10^7 \mathrm{N/m}$, using the second strategy.

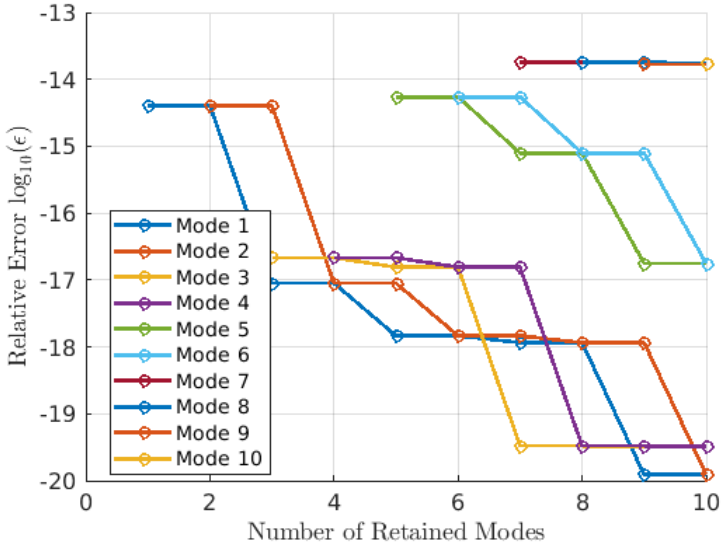

Figure 4.29: Evolution of the relative error between the natural frequencies with the number of modes retained in Craig-Bampton, for an added spring of $10^{10} \mathrm{N/m}$, using the second strategy.

Consistent with the findings for the first strategy, it remains evident that maintaining 6 modes in the reduction method is sufficient for capturing essential characteristics. The minimal relative error observed across scenarios affirms this approach's efficiency in providing an accurate representation of the system's dynamics.

As previously mentioned, the optimal number of retained modes may slightly vary based on specific values of added springs at the contact nodes. To enhance precision, the Modal

Assurance Criterion matrix is once again introduced, offering a nuanced understanding of the number of modes to be retained for the distinct cases in the second strategy.

Analysis of MAC matrix for different number of modes retained

Analyzing the Modal Assurance Criterion matrix for different numbers of retained modes provides insights into the optimal mode selection for the reduction method, considering the three chosen values of added springs.

For an added spring value of 10^2 N/m, as illustrated in Figure 4.30, the MAC matrix fails to approach a perfect identity matrix even with 10 modes retained in the Craig-Bampton method. Off-diagonal elements persist at an order of 10^{-3}, indicating insufficient coupling between the two blades due to the relatively low stiffness in the contact springs.

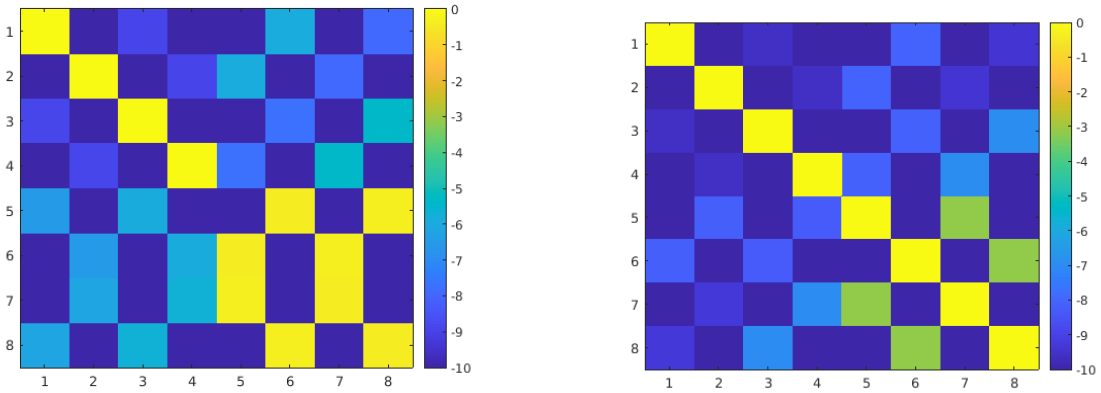

(a) MAC matrix for 6 modes retained.

(b) MAC matrix for 10 modes retained.

Figure 4.30: MAC matrix comparing modes obtained for the full and reduced model for different number of modes retained, for an added spring of 10^2 N/m, using second strategy.

In Figure 4.31, corresponding to an added spring of 10^7 N/m, a similar observation holds. The MAC matrix retains off-diagonal elements, and this behavior is exacerbated in the mid-range added spring region, as evident in the evolution of natural frequencies in Figure 4.17. Here, natural frequencies evolve dramatically with increasing stiffness, influencing the off-diagonal elements in the MAC matrix.

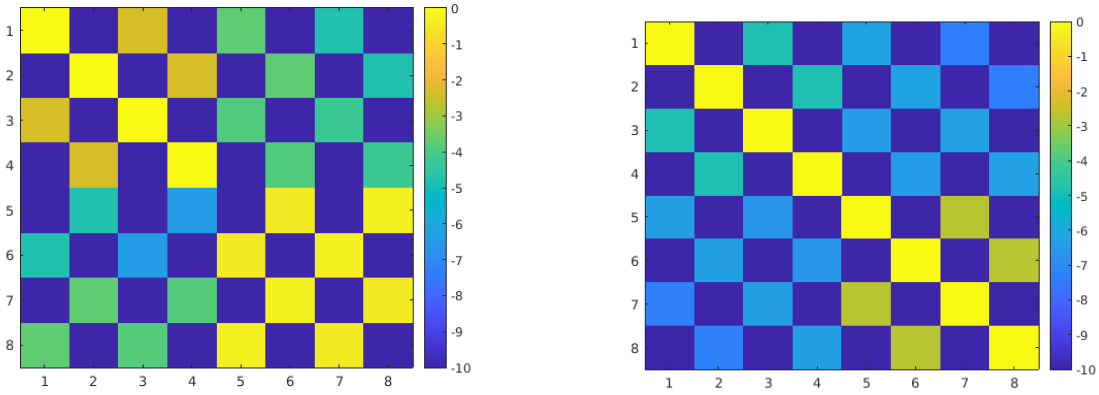

(a) MAC matrix for 6 modes retained.

(b) MAC matrix for 10 modes retained.

Figure 4.31: MAC matrix comparing modes obtained for the full and reduced model for different number of modes retained, for an added spring of 10^7 N/m, using second strategy.

Finally, for a stiffness value of 10^{10} N/m, as depicted in Figure 4.32, the MAC matrix converges towards an identity matrix from 6 modes retained and achieves a perfect identity matrix with 10 modes retained. This signifies that the imposed high stiffness on the contact springs enables a perfectly coupled motion between the two blades, particularly when retaining 10 modes in the Craig-Bampton method.

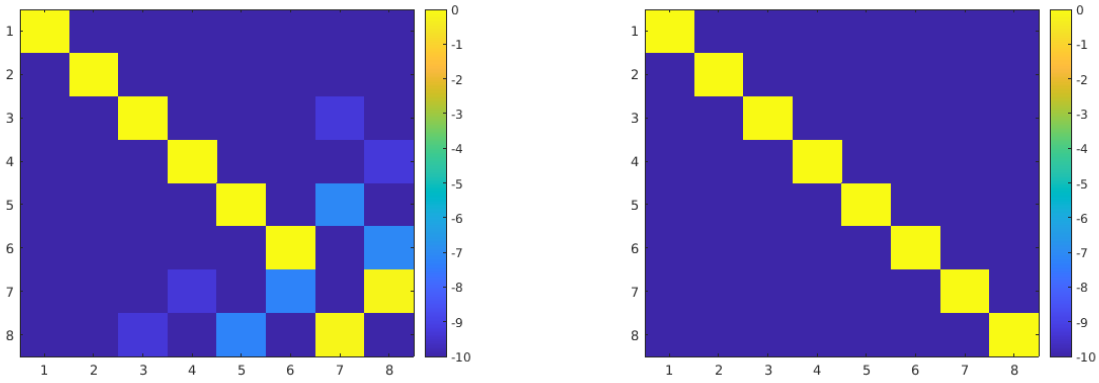

(a) MAC matrix for 6 modes retained.

(b) MAC matrix for 10 modes retained.

Figure 4.32: MAC matrix comparing modes obtained for the full and reduced model for different number of modes retained, for an added spring of 10^{10} N/m, using second strategy.

The interplay between added spring stiffness and retained modes is pivotal in ensuring an accurate representation of the system's dynamic response.

Mode shapes on CalculiX

Once again, to visually comprehend the mode shapes of the system derived from modal analysis in Matlab, the acquired modes are converted into compatible files for visualization in CalculiX.

In Figure 4.33, one observes the representation of the first mode shape linked to the system's firsy natural frequency, where an added spring of 10^2 N/m influences the structural dynamics.

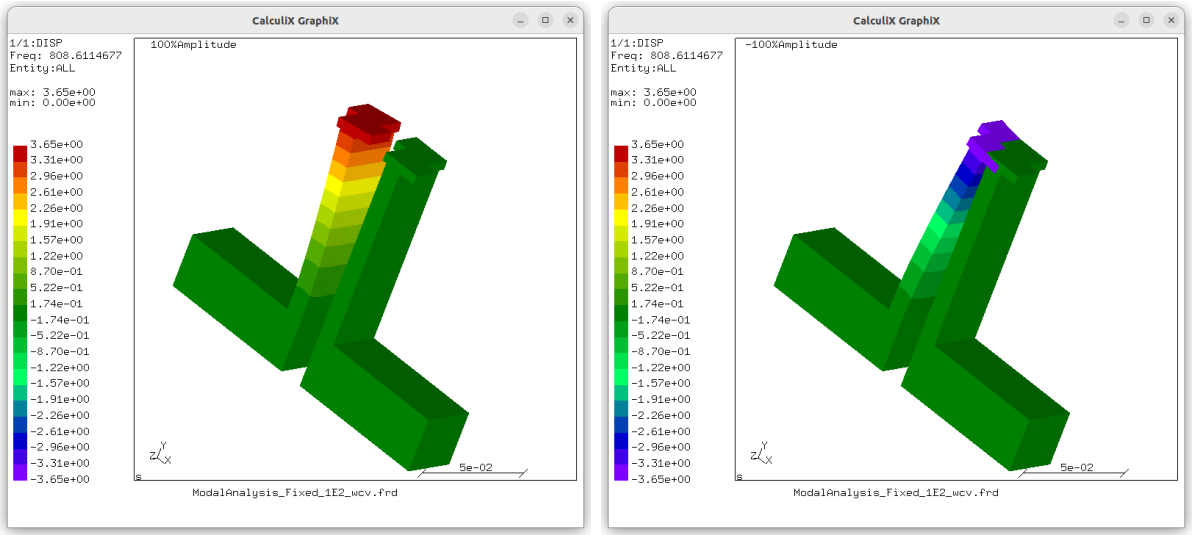

Figure 4.33: Mode shape of the first mode of the model with an added spring of 10^2 N/m on CalculiX, using second strategy.

Moving forward, Figure 4.34 provides a visual insight into the first mode shape for a scenario involving an added spring with a stiffness of 10^7 N/m. This illustration allows us to explore how a considerably higher spring stiffness influences the system's vibrational behavior.

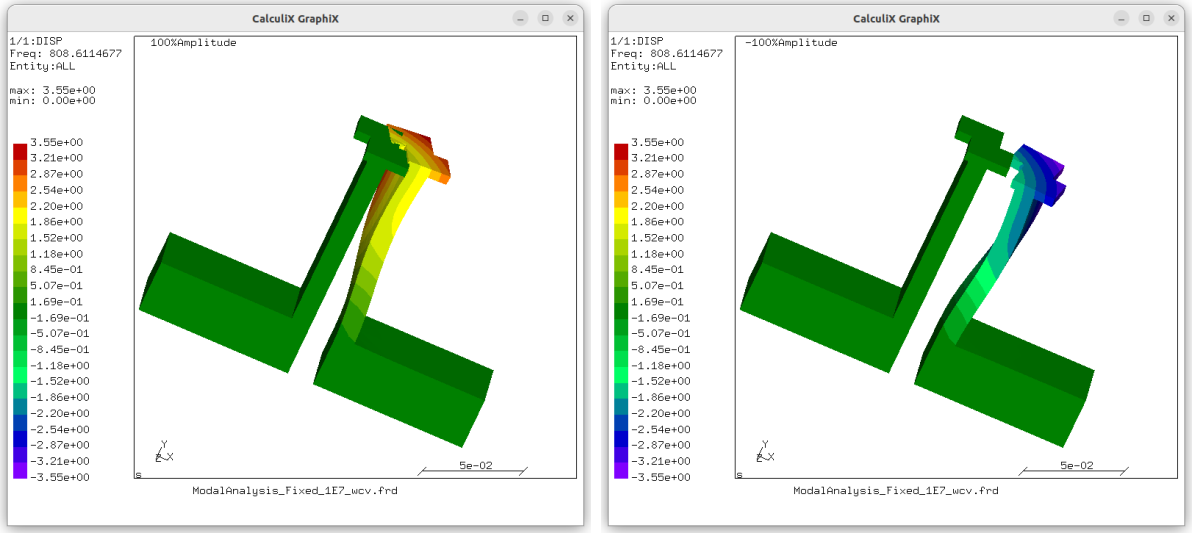

Figure 4.34: Mode shape of the first mode of the model with an added spring of 10^7 N/m on CalculiX, using second strategy.

Finally, Figure 4.35 presents the first mode shape associated with the first natural frequency, emphasizing the impact of an added spring with a substantial stiffness of 10^{10} N/m.

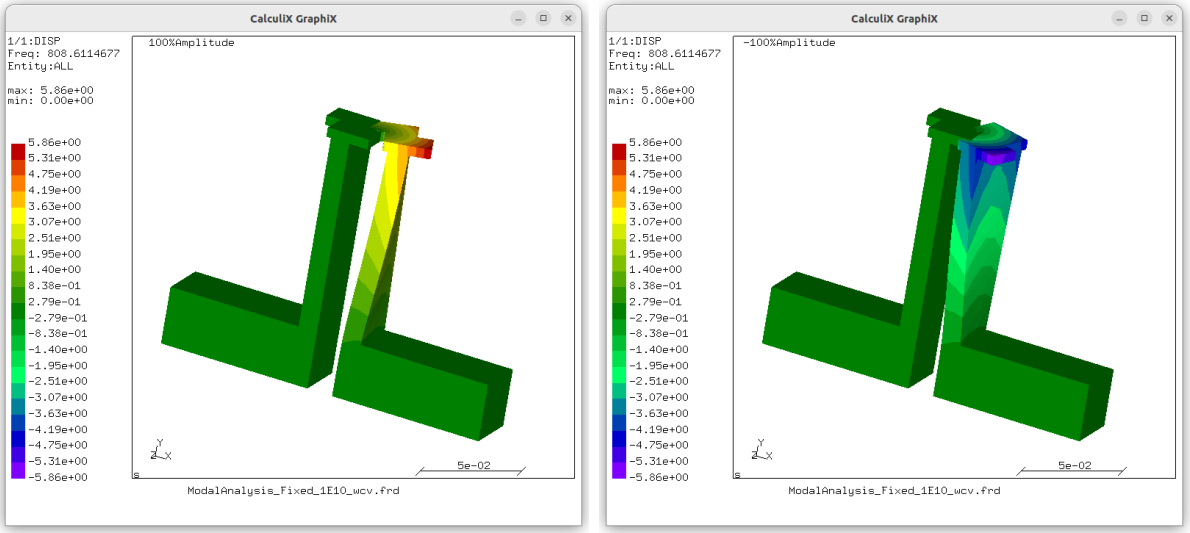

Figure 4.35: Mode shape of the first mode of the model with an added spring of 10^{10} N/m on CalculiX, using second strategy.

This detailed exploration provides a nuanced understanding of how varying spring values contribute to the distinct mode shapes and overall system dynamics.

4.7.3 Comparison between both strategies

The objective of this study is to compare the convergence outcomes of the two strategies. The results obtained from the relative error convergence study and the MAC matrix computation facilitate the identification of key distinctions between the two approaches.

Regarding the relative error convergence analysis, consistent outcomes were observed. For the first strategy, maintaining 6 modes in the Craig-Bampton method yielded minimal relative errors across various added spring values, as illustrated in Figures 4.18, 4.19, and 4.20. Similarly, the second strategy, depicted in Figures 4.27, 4.28, and 4.29, supported the retention of 6 modes for achieving low relative errors in different scenarios. Both strategies exhibited comparable convergence patterns, underscoring the method's resilience with a modest number of retained modes.

In contrast, the results for the MAC matrix analysis displayed more pronounced differences. For the first strategy, the MAC matrix, as seen in Figures 4.21, 4.22, and 4.23, converged towards an identity matrix, with a faster convergence rate for higher spring stiffness values. In the second strategy, illustrated in Figures 4.30, 4.31, and 4.32, the MAC matrix also exhibited convergence, but special attention is warranted for scenarios with lower spring stiffness.

As a reminder, Figure 4.36 presents the MAC matrices obtained for the same value of added spring of 10^{10} N/m, with 6 modes retained in the reduction method, for the two different strategies. As mentioned earlier, it can be observed that achieving a perfect identity matrix is more attainable using the first strategy than the second one.

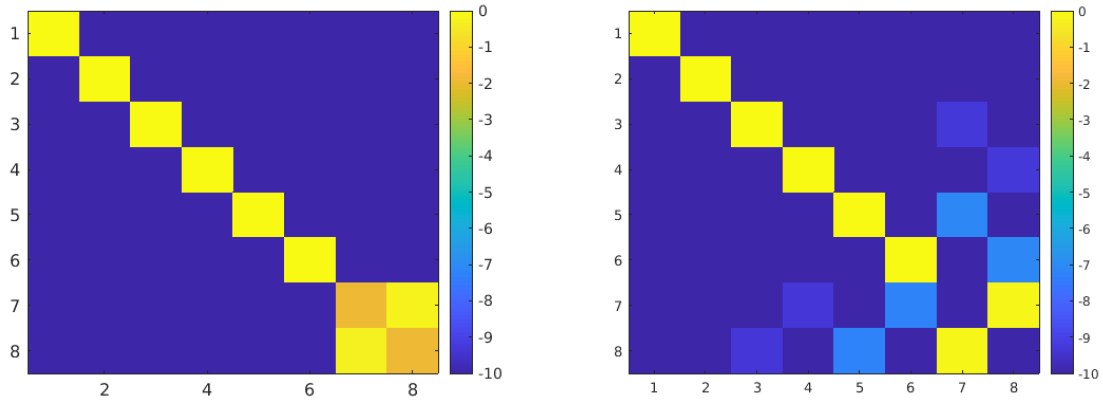

(a) MAC matrix obtained with the first strategy. **(b)** MAC matrix obtained with the second strategy.

Figure 4.36: MAC matrix comparing modes obtained for the full and reduced model for 6 modes retained, for an added spring of 10^{10} N/m, for the two strategies.

In summary, both strategies effectively captured the dynamics of the system, demonstrating subtle differences in convergence behavior. Practical considerations should guide the selection between strategies, taking into account computational efficiency and accuracy. A well-balanced approach, complemented by visual insights from CalculiX mode shapes, serves as a valuable guide for optimal reduction strategy selection.

CHAPTER 5

STUDY OF A BLADED-DISK SECTOR MODEL

After applying both strategies to a simplified model, attention can be directed toward a more intricate and practical component — the bladed disk sector. This component, also known as a turbine or compressor blade sector, is commonly found in gas turbine engines, widely used in aircraft propulsion, power generation, and other applications.

A bladed disk sector typically consists of a circular disk with attached blades or airfoils, strategically designed to efficiently extract or impart energy to the fluid (usually air) flowing through the engine. It is a crucial part of both the compressor and turbine sections of a gas turbine engine.

In the compressor section, the bladed disk aids in compressing incoming air. The rotating blades increase air pressure, directing it into the combustion chamber. In the turbine section, the bladed disk extracts energy from high-temperature, high-pressure gases produced in the combustion process. This extracted energy is then used to drive the compressor and other accessories, contributing to the engine's overall efficiency.

The term "bladed disk sector" often refers to a segment of the full disk, as gas turbine engines may have multiple blades arranged in a circular pattern. In Figure 5.1, the component to be meshed and analyzed is indeed a segment of the full disk. These blades work collaboratively to manage airflow and extract or impart energy as needed for the engine's operation.

The design and engineering of bladed disk sectors are critical for optimizing gas turbine engine performance and reliability in harsh conditions. Advances in materials, aerodynamics, and manufacturing techniques continue to improve the efficiency and durability of bladed disk sectors in modern gas turbine engines.

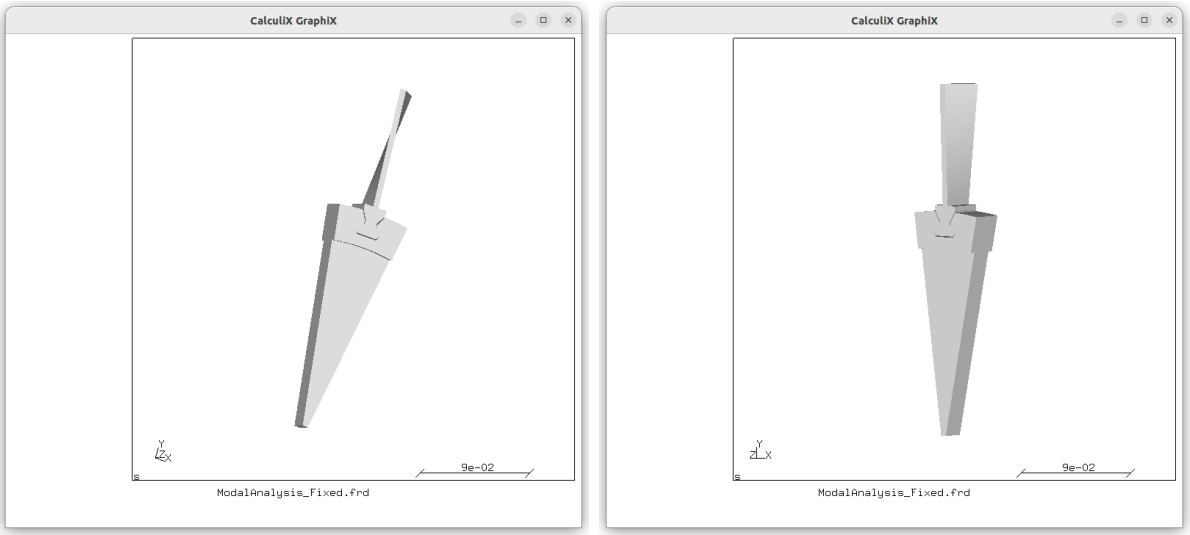

Figure 5.1: Representation of the bladed-disk sector model on CalculiX.

Now, the main focus shifts to the contacts between the blade and the disk. In this chapter, the no-contact case is not studied, as the primary goal is to examine the interaction between the blade and the disk segment rather than studying them separately. In this case, twelve pairs of contacts are defined between the two pieces. The location of the contact nodes is represented in Figure 5.2.

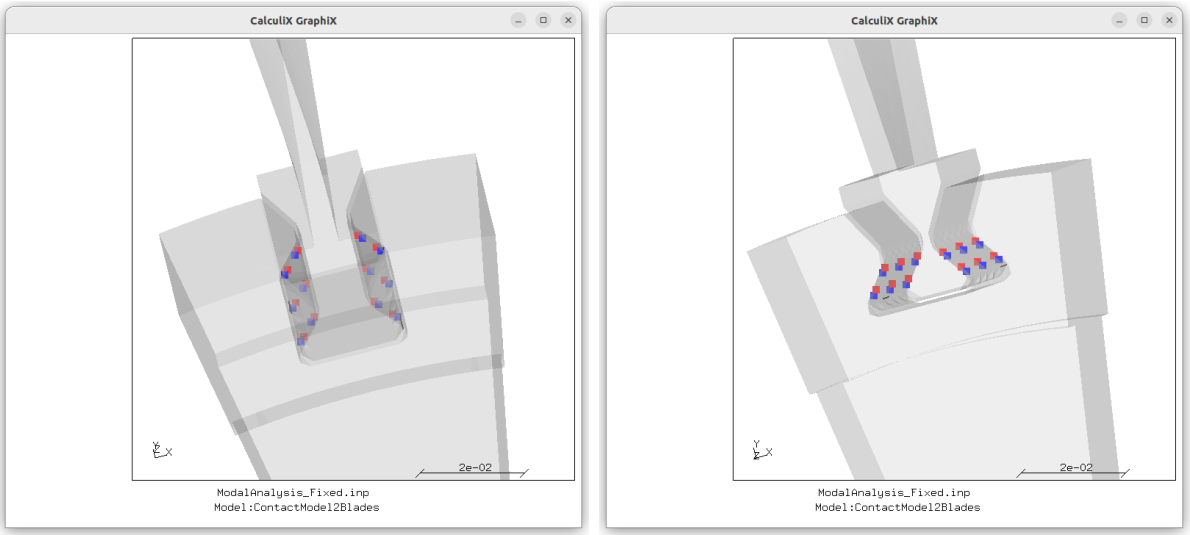

Figure 5.2: Location of the contact nodes within the model.

These nodes are selected to precisely represent the interaction between the two pieces while minimizing the number of contact nodes. Since the number of degrees of freedom relative to the contact nodes is crucial in the Craig-Bampton reduction method, a minimal number of contacts should be chosen while maintaining a certain level of accuracy.

To initiate the analysis, it is important to note that the contacts between the blade and the disk sector are initially considered to be fixed in pairs. This imposes the condition:

$$x_{cb} = x_{cd}, \tag{5.1}$$

where x_{cb} and x_{cd} represent the degrees of freedom corresponding to contact nodes on the blade and the disk sector, respectively.

This condition is enforced only at the beginning of the analysis to test the two strategies under fixed conditions.

Regarding the mesh, the application of the same type of elements as those used in the simplified model has been maintained, specifically the C3D10 elements, for consistency and compatibility reasons. However, a notable distinction arises in the mesh refinement, as illustrated in Figure 5.3, which results in a total node count of 24,481. Once again, the mesh convergence study has been performed by S. Rodriguez Blanco in his doctoral thesis [17].

This finer mesh configuration serves to enhance the intricacy of the model. The decision to refine the mesh was driven by the aim to achieve a more detailed representation of the physical system under examination. The increased number of nodes in the refined mesh facilitates a more precise capture of intricate features and variations within the bladed disk sector. Such nuanced details may have been overlooked in a coarser mesh.

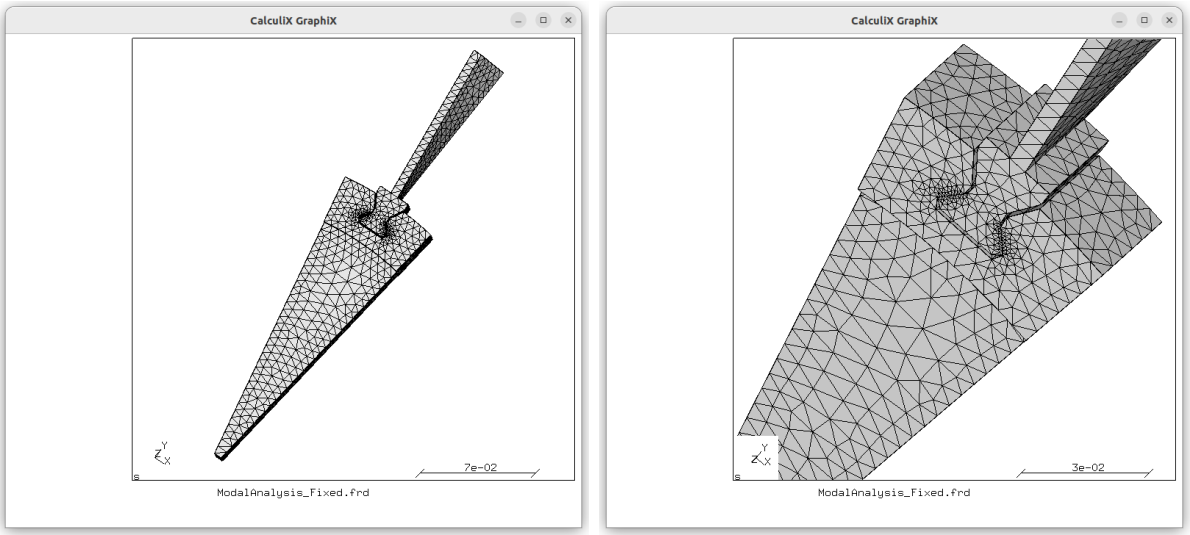

Figure 5.3: Representation of the mesh on CalculiX.

5.0.1 Boundary conditions

To progress with the analysis of the bladed-disk sector model, it is essential to establish the boundary conditions applied to the finite element model. In line with the study's framework, the degrees of freedom at the middle of the disk sector are constrained in both the $x-$ and $z-$ directions.

The DOFs for the displacement at a boundary node of the disk sector are denoted as follows:

- x_{dm} for displacement in the x direction (1^{st} degree of freedom)
- z_{dm} for displacement in the z direction (3^{rd} degree of freedom)

The boundary conditions are mathematically represented as:

$$\begin{aligned} x_{dm} &= 0, \\ z_{dm} &= 0, \end{aligned} \tag{5.2}$$

where the subscript "dm" denotes "disk middle".

The first condition ensures no horizontal movement at the middle of the disk sector, while the second condition guarantees no vertical movement at the middle.

Constraining the DOFs in these directions ensures the stability of the model and accurately represents the dynamic interactions within the disk sector, free from errors due to rigid body motions. These boundary conditions are consistently applied throughout the study to ensure the reliability and validity of the simulation results.

Note that the bladed-disk model is not bounded in the symmetry walls (right and left) in order to have a bigger contribution of the disk.

The boundary nodes are represented in red in Figure 5.4.

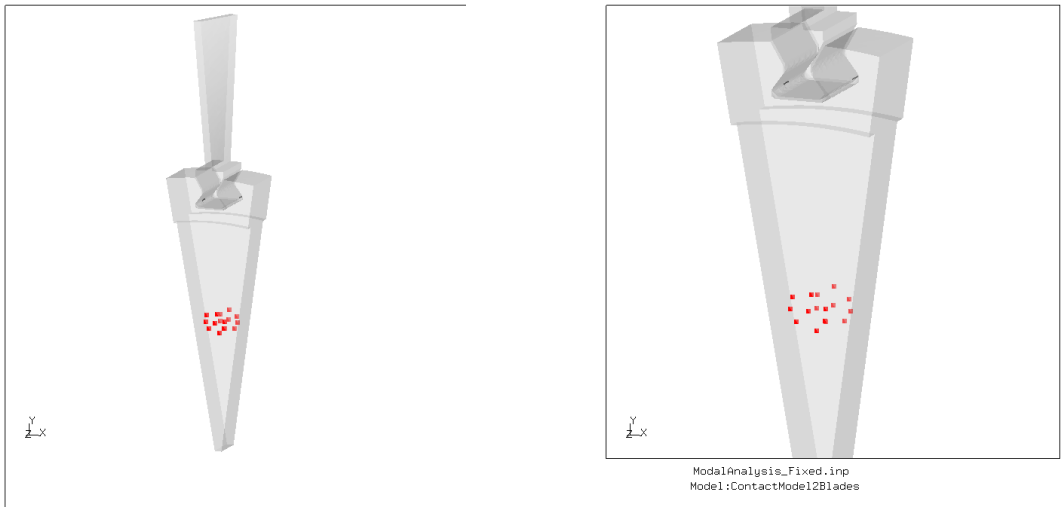

Figure 5.4: Boundary nodes of the model.

5.1 Modal analysis with contact interaction

Building upon the methodology outlined in Section 3.2, a comprehensive modal analysis is conducted on the bladed disk sector model, incorporating predefined pairs of contacts that are kept fixed. This modal analysis is executed using both MATLAB and CALCULIX software tools.

5.1.1 Natural frequencies

In this scenario, the blade is free to move with its six degrees of freedom, while the disk is fixed at the middle. Upon computing the first eight natural frequencies of the system, the values presented in Table 5.1 are obtained.

Table 5.1 Natural frequencies of the full model.

ω_1 [rad/s]	$0.0332 + 0.0000i$
ω_2 [rad/s]	$0.0666 + 0.0000i$
ω_3 [rad/s]	$0.0000 + 0.1351i$
ω_4 [rad/s]	$0.0000 + 0.1444i$
ω_5 [rad/s]	$0.1677 + 0.0000i$
ω_6 [rad/s]	$0.2702 + 0.0000i$
ω_7 [rad/s]	$7.6502 \cdot 10^3 + 0.0000i$
ω_8 [rad/s]	$7.9506 \cdot 10^3 + 0.0000i$

It is noteworthy that the initial six frequencies are close to 0. Ideally, these values should be precisely 0, but due to numerical errors in MATLAB, they are not exact. These numerical errors arise from round-off errors, truncation errors, and the finite precision of floating-point arithmetic in the computational methods used by MATLAB. The occurrence of these initial six nearly zero values implies the presence of six rigid body modes associated with the system.

Eigenvalues represent the natural frequencies of a dynamic system. The existence of zero eigenvalues (or natural frequencies) signifies rigid body motion or translational/rotational modes wherein the entire system moves without undergoing deformation or vibration.

In this specific instance, the six degrees of freedom linked to the blade (translations along the x, y, z axes, and rotations about the x, y, z axes) contribute to these rigid body modes. Since the disk is firmly fixed at the middle and cannot move, it does not introduce any additional rigid body modes. The rigid body modes associated with the blade dominate the lower eigenvalues, resulting in their near-zero values.

The presence of oscillatory modes for ω_3 and ω_4 can be attributed to the damping effects or complex dynamic interactions within the system. These imaginary components indicate the existence of damped oscillations.

In structural dynamics, the inclusion of rigid body modes in the system's dynamic response is commonplace. These modes do not signify deformation or vibration of the structure but rather denote its overall translation or rotation in space.

Given the insights obtained from the analysis of the first six natural frequencies, the subsequent sections of this study will shift the focus to the examination and exploration of frequencies that follow, aiming to gain a comprehensive understanding of the system's dynamic behavior. Consequently, when referring to the initial eight natural frequencies or modes, it pertains to the 7^{th} through 15^{th} frequencies or modes, for example.

5.1.2 Mode shapes on CALCULIX

Employing CALCULIX, a detailed exploration of the model's mode shapes is undertaken, considering the pairs of contacts as fixed to each other. The visualization of these mode shapes provides valuable insights into the dynamic behavior of the system.

In Figure 5.5, the first mode shape corresponding to the first natural frequency is presented. The associated natural frequency is expressed in cycles per unit time, precisely measured at 366.95 cycles per second. In international units, this equates to $2305.597\ \mathrm{rad/s}$. The inclusion of this numerical information enhances the interpretability of the results.

The mode shape is thoughtfully represented at varying amplitudes, allowing for a more comprehensive understanding of the model's motion. By visualizing the mode shape at

different amplitudes, a nuanced depiction of the vibration characteristics at the first natural frequency is achieved.

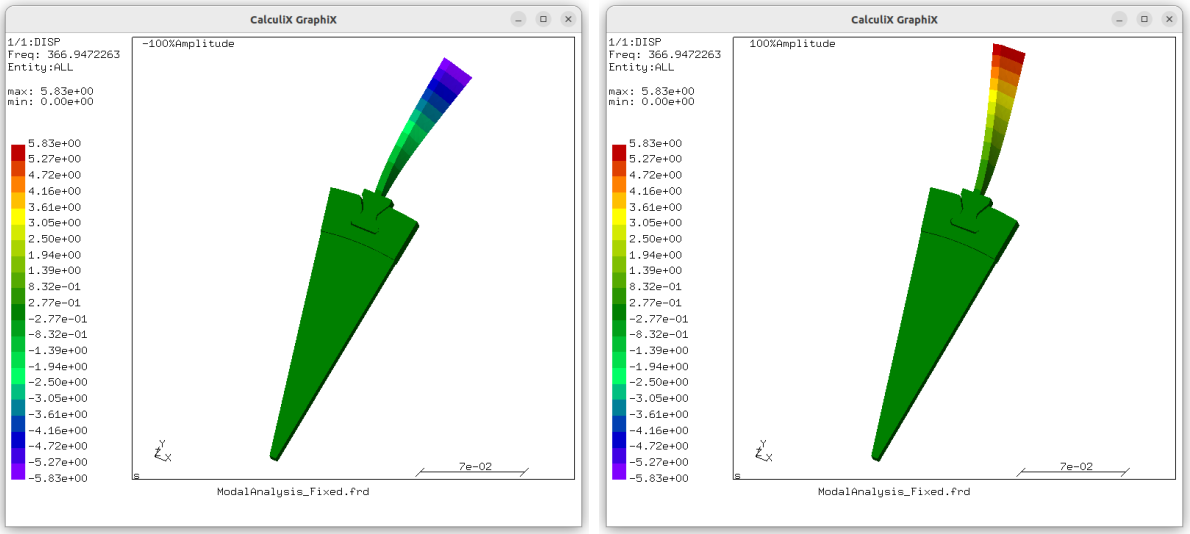

Figure 5.5: Mode shape of the first mode of the fixed model on CalculiX.

5.2 Application of the Craig-Bampton reduction

Given the heightened complexity and refinement of the defined mesh, the number of degrees of freedom of the system has significantly increased. In light of this, the application of a reduction method, such as Craig-Bampton, becomes even more imperative. The primary objective is to mitigate computational demands without compromising the accuracy of the results.

The two strategies outlined in Subsections 4.5.1 and 4.5.2 are employed to implement the Craig-Bampton reduction method. These strategies are selected to facilitate a comparative analysis in terms of their convergence behavior concerning the number of retained modes in the reduction process.

As the intricacy of the model intensifies with the refined mesh, the Craig-Bampton reduction method plays a crucial role in achieving a balance between computational efficiency and result accuracy. By systematically exploring and contrasting the two defined strategies, we aim to discern their effectiveness in capturing the essential modal characteristics of the bladed disk sector while varying the number of retained modes. This investigation not only contributes to optimizing computational efficiency but also sheds light on the sensitivity of the Craig-Bampton reduction process to different strategies, providing valuable insights for future analyses and model refinements.

It is noteworthy that, based on the observations outlined in Subsection 5.1.1, the minimum number of modes to be retained in the Craig-Bampton method should be 7 to ensure a comprehensive representation of the dynamic behavior of the entire system.

5.2.1 First strategy

The initial strategy involves implementing a change of variables before the reordering of vectors and matrices in the application of Craig-Bampton. This alteration in variables serves the purpose of establishing a relationship between the contact nodes of the blade and those of the disk. The introduction of this change facilitates a coherent connection between the nodes, ensuring that the subsequent application of Craig-Bampton effectively captures the interdependence of the blade and disk contact nodes.

Convergence study: Relative error analysis with varying number of retained modes in the Craig-Bampton method

Similar to the approach adopted for the simplified model, a convergence study is conducted for the bladed disk sector. The study involves computing the relative error between the natural frequencies obtained from both the full and reduced models, considering different numbers of modes retained in the Craig-Bampton reduction method. The computation of relative error is based on Equation 4.11.

Figure 5.6 provides a visual representation of the convergence of the relative error concerning the number of retained modes. It is important to note that, as a prerequisite, the minimum number of modes to retain is set at 7 to ensure the inclusion of non-rigid body modes.

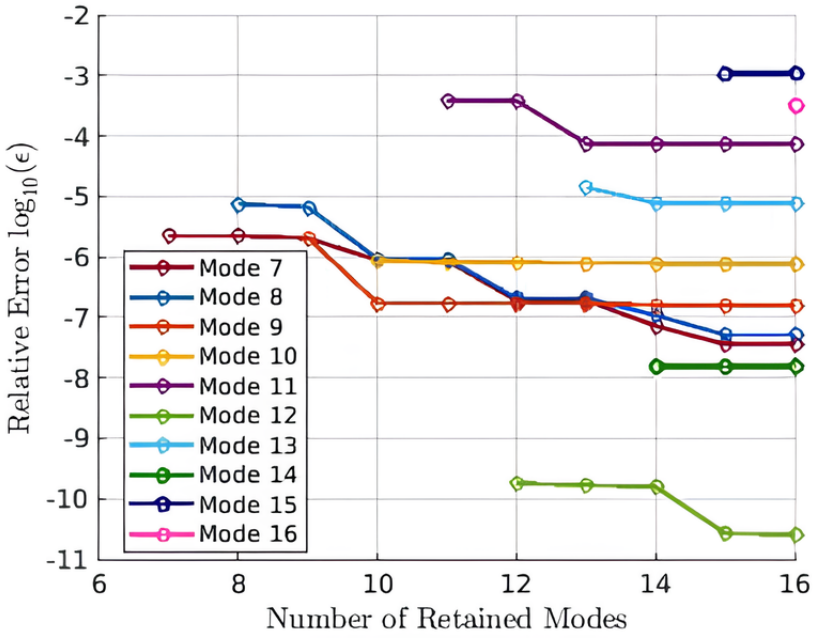

Figure 5.6: Evolution of the relative error between the natural frequencies with the number of modes retained in Craig-Bampton, using the first strategy.

The plot illustrates that the relative error remains relatively small even for a modest number of retained modes. Notably, a choice is made to consider 12 modes retained, exceeding the minimum requirement by 7 modes. This decision is deemed acceptable as the relative error at this point is considered within an acceptable range, ensuring a representative and accurate portrayal of the full model with its reduced counterpart.

Table 5.2 presents the values of the 7^{th} to 12^{th} natural frequencies obtained from both the full and reduced models. The initial 6 frequencies, being equal to 0, are representative of rigid body motion.

Table 5.2 Natural frequencies of the full and reduced model using the first strategy.

	Full model	Reduced model
ω_7 [rad/s]	$7.6501 \cdot 10^3$	$7.6524 \cdot 10^3$
ω_8 [rad/s]	$7.9507 \cdot 10^3$	$7.9534 \cdot 10^3$
ω_9 [rad/s]	$8.9258 \cdot 10^3$	$8.9308 \cdot 10^3$
ω_{10} [rad/s]	$2.1211 \cdot 10^4$	$2.1234 \cdot 10^4$
ω_{11} [rad/s]	$2.1239 \cdot 10^4$	$2.1409 \cdot 10^4$
ω_{12} [rad/s]	$2.2196 \cdot 10^4$	$2.2196 \cdot 10^4$

Unlike the simplified model, the frequencies are not defined in pairs, as the blade and disk segment are distinct components. Specifically, these frequencies pertain exclusively to the blade. Since MATLAB computes eigenvalues from the smallest to the largest, and considering the blade's lower rigidity compared to the disk, the first natural frequencies presented here are solely relative to the blade.

Analysis of MAC matrix with 12 retained modes

In order to substantiate the decision to retain 12 modes in the Craig-Bampton reduction, an analysis of the Modal Assurance Criterion matrix is conducted using Equation 4.12.

Figure 5.7 provides a visual representation of the MAC matrix, allowing for the verification of the efficiency of the reduction process. The obtained identity matrix indicates a perfect correlation between the modes of the full and reduced models. This result signifies that the choice to retain 12 modes is indeed acceptable, as evidenced by the well-applied reduction. The strong correlation between the modal shapes ensures that the reduced model accurately captures the essential dynamic characteristics of the full model, further supporting the robustness and appropriateness of the chosen reduction strategy.

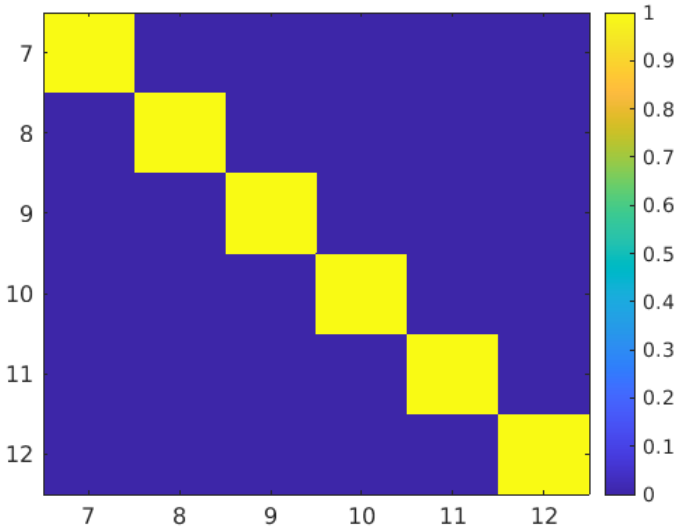

Figure 5.7: MAC matrix comparing modes obtained with the full and reduced model using first strategy.

5.2.2 Second strategy

The second strategy involves reordering the matrices and vectors of the system to apply the Craig-Bampton reduction, without introducing any change of variables. Unlike the first strategy, which includes a change of variables before reordering, this approach streamlines the reduction process by directly manipulating the existing mathematical components.

Convergence study: Relative error analysis with varying number of retained modes in the Craig-Bampton method

Implementing the second strategy involves conducting a convergence study that examines the relative error between the natural frequencies of the full and reduced models. This analysis is performed with respect to the number of retained modes, employing the same Equation 4.11 for computing the relative error.

Figure 5.8 visually illustrates the evolution of the relative error as the number of retained modes changes. Similar to the first strategy, maintaining a minimum of 7 modes is essential to ensure that the reduced model accurately represents the dynamic characteristics of the full model beyond rigid body motion.

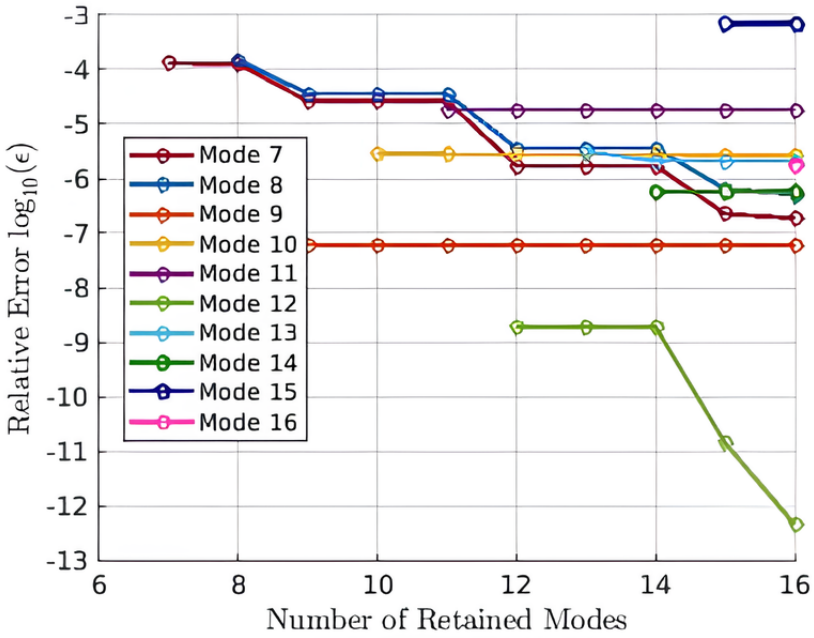

Figure 5.8: Evolution of the relative error between the natural frequencies with the number of modes retained in Craig-Bampton, using the second strategy.

Commencing with 7 retained modes, the relative error consistently remains small, even with a modest number of modes. To maintain consistency with the first strategy, a decision is made to retain 12 modes, a number deemed sufficient to faithfully represent the full model.

Table 5.3 presents the values of the 7^{th} to the 12^{th} natural frequencies, with the initial 6 frequencies associated with rigid body motion being equal to 0 (without any numerical error). These natural frequencies are provided for both the full and reduced models, considering 12 retained modes.

Table 5.3 Natural frequencies of the full and reduced model using the second strategy.

	Full model	Reduced model
ω_7 [rad/s]	$7.6502 \cdot 10^3$	$7.6548 \cdot 10^3$
ω_8 [rad/s]	$7.9506 \cdot 10^3$	$7.9580 \cdot 10^3$
ω_9 [rad/s]	$8.9255 \cdot 10^3$	$8.9288 \cdot 10^3$
ω_{10} [rad/s]	$2.1210 \cdot 10^4$	$2.1250 \cdot 10^4$
ω_{11} [rad/s]	$2.1239 \cdot 10^4$	$2.1331 \cdot 10^4$
ω_{12} [rad/s]	$2.2196 \cdot 10^4$	$2.2196 \cdot 10^4$

The values for the full model closely mirror those obtained with the first strategy, with slight differences attributed to numerical errors in the MATLAB software. This occurs because, as explained for the simplified model, the introduction of a change of variables doesn't affect the modal characteristics of the full model. Concerning the reduced model, the natural frequencies closely align with those of the full model, affirming the adequacy of the chosen number of retained modes.

Analysis of MAC matrix with 12 retained modes

Similar to the first strategy, the Modal Assurance Criterion matrix is employed as a validating measure between the modes of the full and reduced models, specifically with 12 modes retained, further strengthening the justification for this selection.

The relevance of this choice is underscored by the MAC matrix, as depicted in Figure 5.9. Notably, the MAC matrix closely resembles a perfect identity matrix, affirming the effectiveness of the reduction process. The striking similarity between the modes of the full and reduced models, as indicated by the MAC matrix, provides additional evidence supporting the appropriateness of retaining 12 modes. This visual representation contributes to the comprehensive assessment of the reduction method's performance and its ability to faithfully capture the dynamic characteristics of the bladed disk sector.

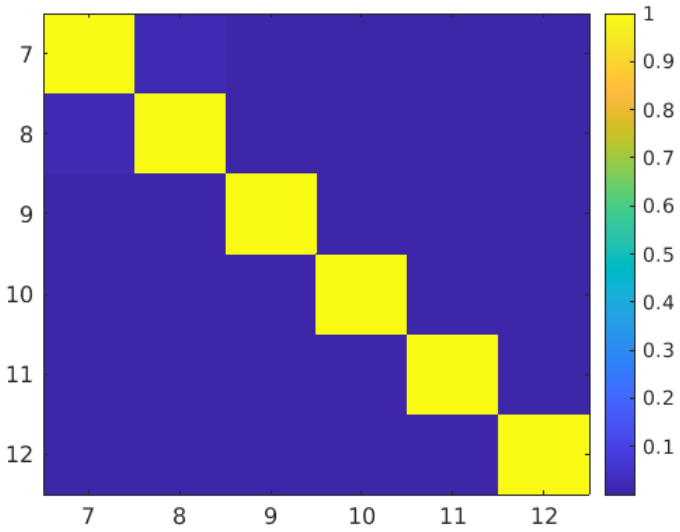

Figure 5.9: MAC matrix comparing modes obtained with the full and reduced model using second strategy.

5.2.3 Comparison between the two strategies

The application of the Craig-Bampton reduction method to the bladed disk sector, with its heightened complexity and refined mesh, demands careful consideration and selection of reduction strategies. The two strategies, namely the first strategy involving a change of variables and the second strategy involving only reordering, were systematically analyzed and compared to evaluate their performance in capturing the essential modal characteristics while varying the number of retained modes.

The convergence study, depicted in Figures 5.6 and 5.8, showcased the relative error between the natural frequencies of the full and reduced models. Both strategies demonstrated consistent convergence, with the relative error staying small even for a modest number of retained modes. A prudent choice of retaining 12 modes for both strategies was made, exceeding the minimum requirement by 7 modes, ensuring an acceptable level of accuracy.

The analysis of the Modal Assurance Criterion matrix, illustrated in Figures 5.7 and 5.9, further validated the effectiveness of the reduction process. The close resemblance to a perfect

identity matrix in both cases indicated a strong correlation between the modes of the full and reduced models. This visual confirmation supported the appropriateness of retaining 12 modes for both strategies.

In comparing the two strategies, the results obtained for the natural frequencies in Tables 5.2 and 5.3 revealed close agreement between the full and reduced models. The small differences observed were attributed to numerical errors in the MATLAB software and were consistent across both strategies. This consistency reinforced the notion that the introduction of a change of variables in the first strategy did not significantly impact the modal characteristics.

In summary, both strategies exhibited robustness and adequacy in capturing the dynamic behavior of the bladed disk sector. The decision to retain 12 modes, regardless of the strategy employed, proved to be effective in achieving a balance between computational efficiency and result accuracy. The comparative analysis offered valuable insights into the sensitivity of the Craig-Bampton reduction process to different strategies, aiding in informed decision-making for future analyses and model refinements.

5.3 Enhancement through the addition of springs to the contact nodes

Similar to the considerations in the simplified model, the bladed disk sector model also faces the potential occurrence of friction between the blades and the disk segment. To address this nonlinear phenomenon, a strategic approach is adopted by introducing linear springs between the predefined pairs of contact. This proactive measure not only simplifies the treatment of friction-related nonlinearity but also aligns with the linear focus of the thesis.

The introduction of these linear springs carries an added layer of complexity to the system's equations of motion, particularly influencing the stiffness matrix K. The modified formulations for these models are expressed through Equation 4.19 for the first strategy and Equation 4.20 for the second strategy.

With the addition of these linear springs, the contact pairs are no longer fixed together. As a result, the condition defined by Equation 5.1 is no longer satisfied, reflecting the changed dynamics due to the introduction of the springs.

The incorporation of these linear springs presents an opportunity for enhanced representation and analysis of the contact dynamics within the bladed disk sector. By assigning a common value to these springs, a level of simplicity is maintained, allowing for a systematic investigation of the linear interactions between the blade and the disk segment. This deliberate enhancement contributes not only to the mitigation of friction-related nonlinearity but also to the overall analytical tractability of the system.

5.3.1 First strategy

Using the first strategy, a modal analysis is performed on the full model, considering two distinct values for the added springs: 10^3 N/m and 10^9 N/m. The results of this analysis encompass the 7^{th} to the 12^{th} natural frequencies, as presented in Table 5.4.

Table 5.4 Natural frequencies of the full model for different added stiffness values using the first strategy.

	Addition of $k_{\text{spr}} = 10^3$ N/m	Addition of $k_{\text{spr}} = 10^9$ N/m
ω_7 [rad/s]	$7.6520 \cdot 10^3$	$2.1555 \cdot 10^4$
ω_8 [rad/s]	$7.9524 \cdot 10^3$	$2.2204 \cdot 10^4$
ω_9 [rad/s]	$8.9290 \cdot 10^3$	$2.4335 \cdot 10^4$
ω_{10} [rad/s]	$2.1210 \cdot 10^4$	$3.1861 \cdot 10^4$
ω_{11} [rad/s]	$2.1239 \cdot 10^4$	$3.8541 \cdot 10^4$
ω_{12} [rad/s]	$2.2196 \cdot 10^4$	$4.3741 \cdot 10^4$

Examination of these frequencies reveals noteworthy insights. For an added spring value of 10^3 N/m, the natural frequencies remain in close proximity to those obtained for the full model, as detailed in Table 5.2. Although there is a marginal increase in the frequencies, this effect is relatively modest. However, a more pronounced impact is observed for the added spring value of 10^9 N/m, where the natural frequencies exhibit a substantial increase in magnitude. This behavior aligns with expectations, considering that the addition of springs directly influences the stiffness matrix of the system.

The observed variations in natural frequencies underscore the sensitivity of the dynamic characteristics to changes in stiffness induced by the added springs. This observation reinforces the importance of a meticulous consideration of spring values, as they play a crucial role in shaping the vibrational behavior of the bladed disk sector. Additionally, these findings provide valuable insights into the dynamic response of the system under different spring configurations, offering a nuanced understanding of the interplay between stiffness modifications and natural frequencies.

Dynamic exploration: natural frequency evolution with varied spring values

The dynamic exploration of the system involves a comprehensive analysis of how its natural frequencies evolve in response to varying spring values. This exploration is particularly insightful in understanding the system's sensitivity to changes in stiffness, offering a nuanced perspective on the impact of different spring configurations on its vibrational behavior.

By systematically varying the spring values and observing the corresponding shifts in natural frequencies, we gain valuable insights into the system's dynamic response under different stiffness conditions. This analysis aids in identifying critical points where the system's behavior undergoes significant changes, providing a basis for optimizing the design parameters.

The results of this dynamic exploration, showcasing the evolution of natural frequencies with different spring values in a logarithmic scale, are visually represented in Figure 5.10. The logarithmic scale is chosen for its ability to highlight variations across a broad range of values, allowing for a clearer depiction of the system's behavior under different spring configurations.

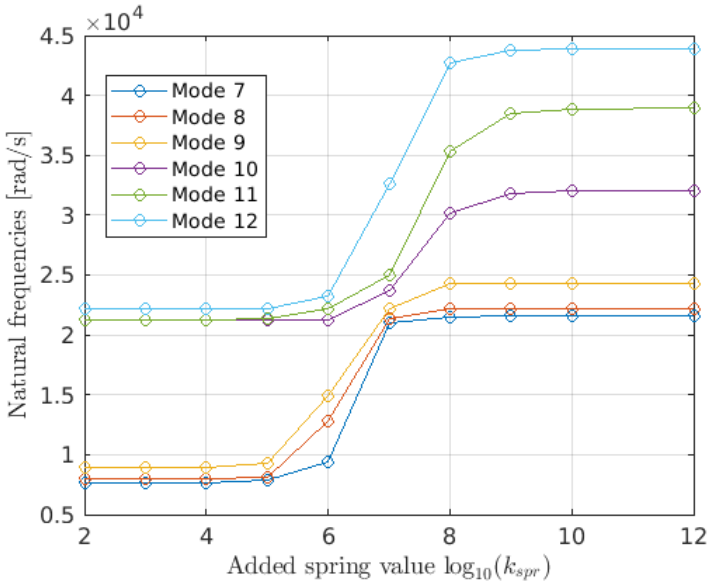

Figure 5.10: Evolution of the natural frequencies with the added spring values, using first strategy.

The analysis of Figure 5.10 reveals the presence of distinct regions characterized by different behaviors in the system's natural frequencies. This observation aligns with the findings from the exploration of the simplified model and further contributes to our understanding of the bladed disk sector's dynamic response to varying spring values.

Similar to the simplified model, three discernible regions emerge in the current investigation: a soft, intermediate, and hard spring values region. Each of these regions provides unique insights into the system's vibrational characteristics under different stiffness conditions.

In the soft spring values region, an interesting shift is noted. Unlike the simplified model, the natural frequencies are no longer defined by pairs in this region. This divergence is attributed to the distinct nature of the blade and disk components, which are not identical. Despite this difference, the plot exhibits a behavior reminiscent of Figure 4.16 from the simplified model. This consistency underscores the robustness of the observed patterns across different configurations and reinforces the significance of the representative spring values of 10^2, 10^7, and 10^{10} $\mathrm{N/m}$ in this region.

5.3.2 Second strategy

The second strategy is employed to perform modal analysis on the full model. The natural frequencies obtained for two distinct values of added springs, 10^3 and 10^9 $\mathrm{N/m}$, are presented in Table 5.5.

Table 5.5 Natural frequencies of the full model for different added stiffness values using the second strategy.

	Addition of $k_{\text{spr}} = 10^3$ N/m	Addition of $k_{\text{spr}} = 10^9$ N/m
ω_7 [rad/s]	$7.6520 \cdot 10^3$	$3.3681 \cdot 10^4$
ω_8 [rad/s]	$7.9524 \cdot 10^3$	$3.9492 \cdot 10^4$
ω_9 [rad/s]	$8.9290 \cdot 10^3$	$4.2744 \cdot 10^4$
ω_{10} [rad/s]	$2.1210 \cdot 10^4$	$4.8643 \cdot 10^4$
ω_{11} [rad/s]	$2.1239 \cdot 10^4$	$4.9890 \cdot 10^4$
ω_{12} [rad/s]	$2.2196 \cdot 10^4$	$5.1729 \cdot 10^4$

Comparing the results with those obtained from the first strategy, similar observations can be made, albeit with subtle differences. For an added spring value of 10^3 N/m, the natural frequencies align closely with those acquired through the first strategy. These frequencies are slightly higher than the ones without any added springs, as evidenced by the values in Table 5.3. This consistency suggests that the addition of a moderate stiffness does not significantly alter the system's vibrational characteristics, regardless of the chosen strategy.

However, a notable distinction arises when considering the frequencies obtained with an added spring of 10^9 N/m. In this case, the impact of introducing a high stiffness value appears to be more pronounced with the second strategy compared to the first one. The frequencies exhibit a more substantial shift, indicating that the choice of strategy influences how the system responds to extreme stiffness conditions. This nuanced difference underscores the importance of strategy selection in accurately capturing and interpreting the dynamic behavior of the bladed disk sector, especially under extreme stiffness scenarios.

Dynamic exploration: natural frequency evolution with varied spring values

The dynamic exploration of the system's natural frequencies is once again conducted, this time employing the second strategy. This exploration involves varying the values of added springs and observing the corresponding evolution of the system's vibrational characteristics. The objective is to gain insights into how the bladed disk sector responds dynamically to different stiffness conditions.

Figure 5.11 illustrates the evolution of the natural frequencies with varying added spring values, presented in a logarithmic scale. This exploration allows us to discern the system's behavior across different regions characterized by low, mid-range, and high added spring values. As observed in the results obtained with the first strategy, the dynamic exploration using the second strategy also reveals distinct regions with varying trends in natural frequency shifts.

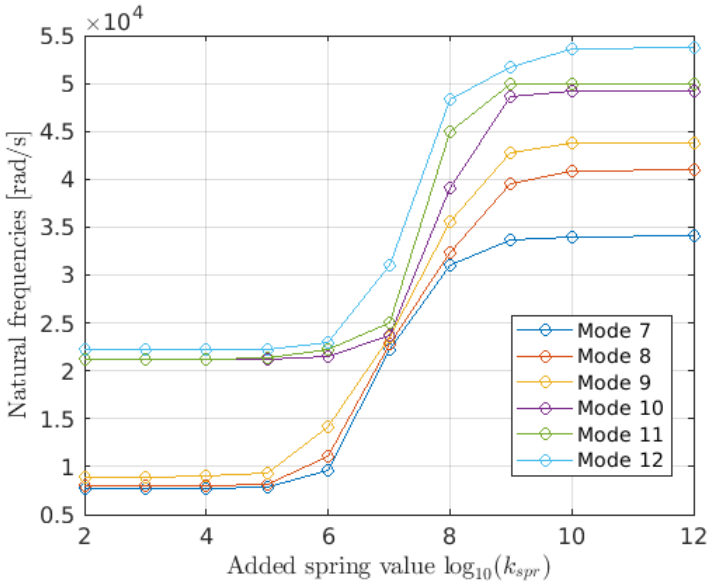

Figure 5.11: Evolution of the natural frequencies with the added spring values, using second strategy.

The evolution curves exhibit a consistent trend, mirroring the observations made with the first strategy. Consequently, one maintains the same three representative values of 10^2, 10^7, and 10^{10} $\mathrm{N/m}$ for the subsequent analysis. This selection ensures a focused and meaningful exploration of the bladed disk sector's dynamic behavior, allowing us to delve deeper into the system's response under varying stiffness conditions.

5.4 Application of the Craig-Bampton reduction with the added springs at the contact nodes

After the introduction of springs at the contact nodes, the subsequent step involves reapplying the Craig-Bampton reduction. This reduction process will be implemented using both strategies, enabling a comparative analysis to discern the influence of the added spring values on the reduced models. This comparative study aims to provide insights into the effectiveness of each strategy in capturing the system's dynamic characteristics under different spring conditions.

5.4.1 First strategy

Convergence study: Relative error analysis with varying number of retained modes in the Craig-Bampton method

To determine the optimal number of modes to retain in the reduction method, a comprehensive convergence study is conducted, mirroring the approach employed in the absence of added springs. The study involves computing the relative error between the natural frequencies of the full and reduced models, considering different numbers of retained modes. Importantly, this analysis is carried out for three distinct values of added spring stiffness: 10^2 $\mathrm{N/m}$, 10^7 $\mathrm{N/m}$, and 10^{10} $\mathrm{N/m}$.

Figure 5.12 illustrates the evolution of the relative error with the number of modes retained for the added spring value of 10^2 N/m. Similarly, Figures 5.13 and 5.14 depict the evolution of the relative error for added spring values of 10^7 N/m and 10^{10} N/m, respectively. These visual representations provide insights into how the number of retained modes influences the accuracy of the reduced models under varying spring conditions.

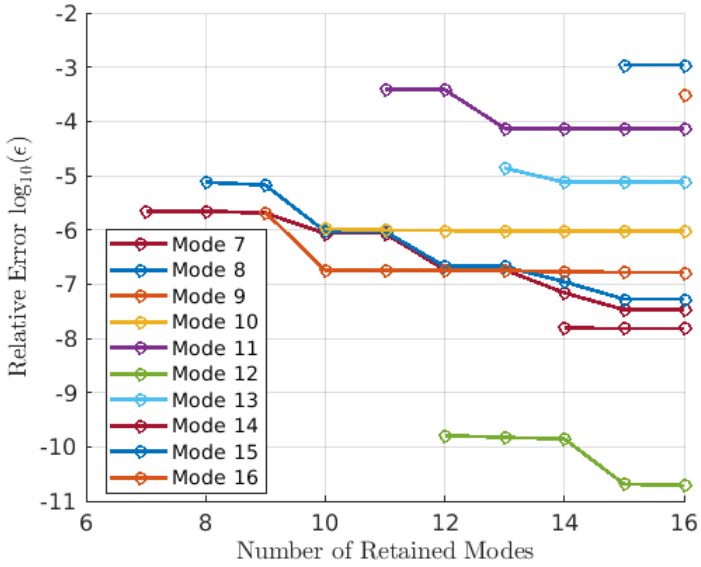

Figure 5.12: Evolution of the relative error between the natural frequencies with the number of modes retained in Craig-Bampton, for an added spring of 10^2N/m, using the first strategy.

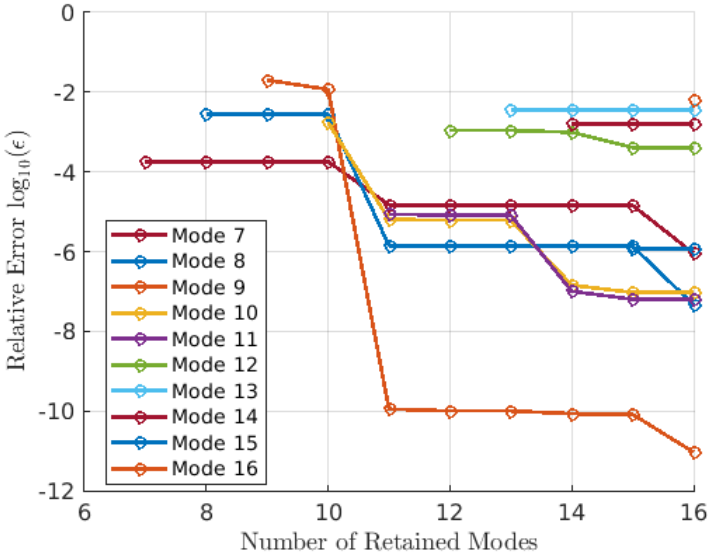

Figure 5.13: Evolution of the relative error between the natural frequencies with the number of modes retained in Craig-Bampton, for an added spring of 10^7N/m, using the first strategy.

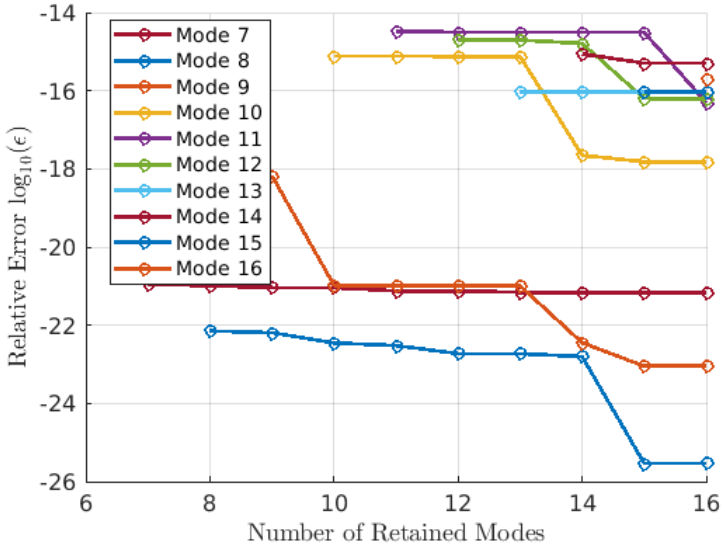

Figure 5.14: Evolution of the relative error between the natural frequencies with the number of modes retained in Craig-Bampton, for an added spring of $10^{10}\mathrm{N/m}$, using the first strategy.

The analysis of the convergence study reveals consistent trends across the three cases, particularly for the 10^7 and 10^{10} stiffness values. The evolution of the relative error remains similar and remains low even for a relatively small number of retained modes. Considering the prerequisite of retaining a minimum of 6 modes for a comprehensive model representation, the choice of retaining 12 modes appears to be a reasonable compromise. However, due to the dependence on the added spring values, a more in-depth analysis is warranted, which involves examining the Modal Assurance Criterion matrix. This additional step will provide a more nuanced understanding of the impact of different added spring values on the reduction method's performance.

Analysis of MAC matrix for different number of modes retained

When considering an added spring value of 10^2 $\mathrm{N/m}$, the MAC matrix depicted in Figure 5.15 illustrates that even with a modest number of retained modes, specifically 7 (which is the minimum required), the MAC matrix closely resembles a perfect identity matrix. This suggests that the imposition of a small stiffness between the blade and the disk enables the reduced model to accurately represent the full model, even with a limited number of retained modes.

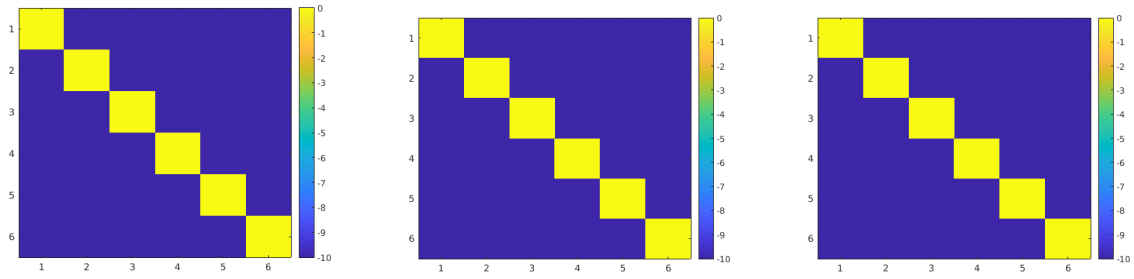

(a) MAC matrix for 7 modes retained.

(b) MAC matrix for 12 modes retained.

(c) MAC matrix for 16 modes retained.

Figure 5.15: MAC matrix comparing modes obtained for the full and reduced model for different number of modes retained, for an added spring of 10^2 N/m, using first strategy.

Moving on to Figure 5.16, which corresponds to an added spring value of 10^7 N/m, it becomes evident that a higher number of modes must be retained compared to the first case. Retaining only 7 modes does not result in a perfect identity matrix. The stiffness value of 10^7 N/m falls within the mid-range region of Figure 5.10, where significant variations occur. These variations in frequencies directly impact the system's modes, necessitating a greater number of retained modes for an accurate representation.

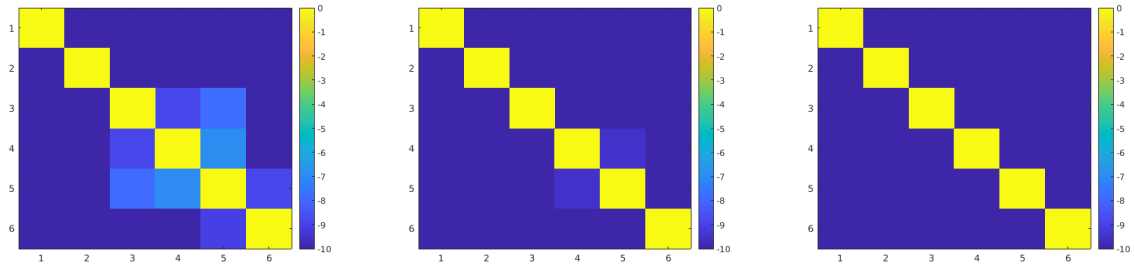

(a) MAC matrix for 7 modes retained.

(b) MAC matrix for 12 modes retained.

(c) MAC matrix for 16 modes retained.

Figure 5.16: MAC matrix comparing modes obtained for the full and reduced model for different number of modes retained, for an added spring of 10^7 N/m, using first strategy.

Finally, for an added spring value of 10^{10} N/m, an identity MAC matrix is once again observed, even with only 7 modes retained, as illustrated in Figure 5.17. This finding implies that for high added spring values, situated outside the mid-range region, the Craig-Bampton reduction can be effectively applied with a small number of retained modes for the first strategy.

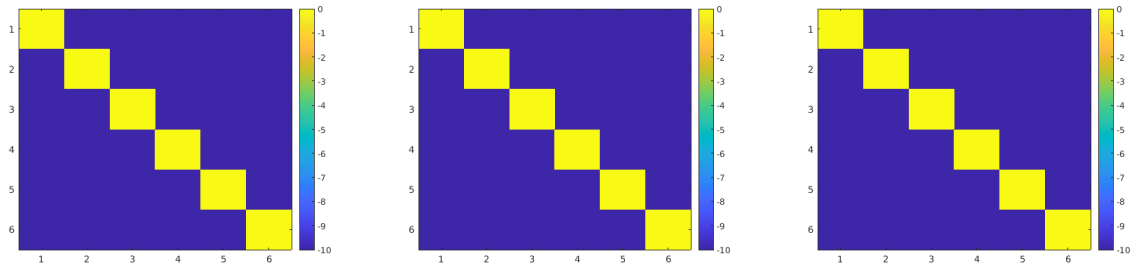

(a) MAC matrix for 7 modes retained.

(b) MAC matrix for 12 modes retained.

(c) MAC matrix for 16 modes retained.

Figure 5.17: MAC matrix comparing modes obtained for the full and reduced model for different number of modes retained, for an added spring of 10^{10} N/m, using first strategy.

Mode shapes on CalculiX

To visualize the impact of added spring values on the model, the mode shapes, obtained through modal analysis on Matlab, are portrayed using CalculiX.

Figure 5.18 illustrates the first mode shape corresponding to the first natural frequency, considering a spring stiffness of 10^2 N/m applied at the contact nodes between the blade and the disk. The representation includes variations in amplitude to enhance understanding of the blade disk sector's motion.

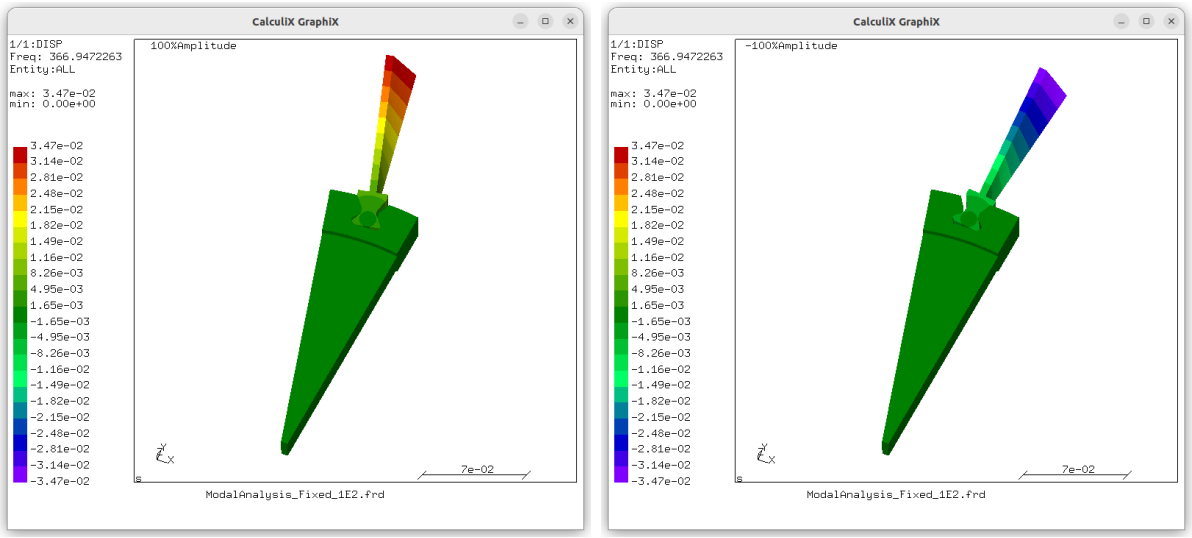

Figure 5.18: Mode shape of the first mode of the model with an added spring of 10^2 N/m on CalculiX, using first strategy.

Similarly, Figure 5.19 presents the mode shapes for the first natural frequency with an added spring stiffness of 10^7 N/m. This visualization helps understanding the altered dynamic behavior resulting from a higher spring stiffness.

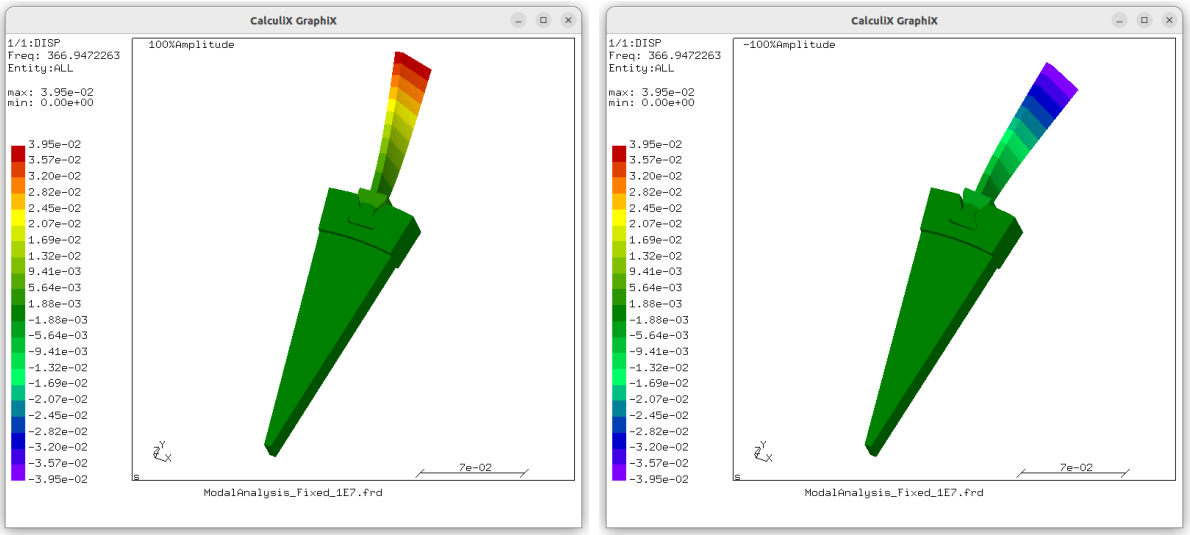

Figure 5.19: Mode shape of the first mode of the model with an added spring of 10^7 N/m on CalculiX, using first strategy.

Expanding the analysis, Figure 5.20 showcases the mode shapes influenced by an added spring stiffness of 10^{10} N/m. This visual exploration provides insights into the distinct motion patterns induced by a significantly higher spring stiffness.

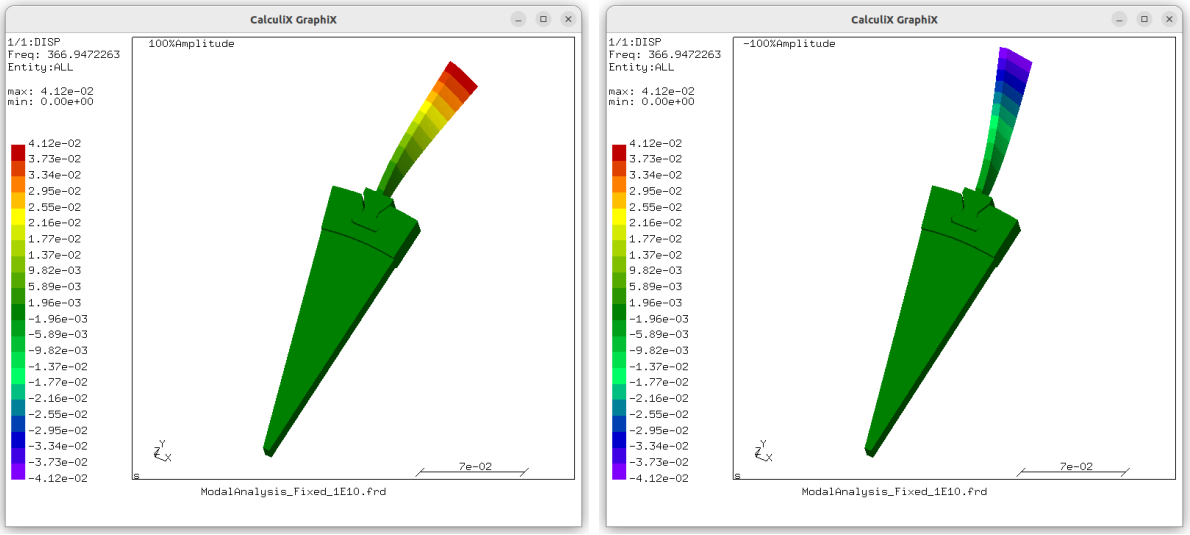

Figure 5.20: Mode shape of the first mode of the model with an added spring of 10^{10} N/m on CalculiX, using first strategy.

5.4.2 Second strategy

Convergence study: Relative error analysis with varying number of retained modes in the Craig-Bampton method

Similar to the first strategy, a convergence study is conducted to determine the optimal number of modes to retain in the reduction method when applying the second strategy, which

involves reordering the matrices and vectors without introducing any change of variables. This analysis is carried out for the same three values of added springs: 10^2, 10^7, and 10^{10} $\mathrm{N/m}$.

The convergence studies for these three values are depicted in Figures 5.21, 5.22, and 5.23.

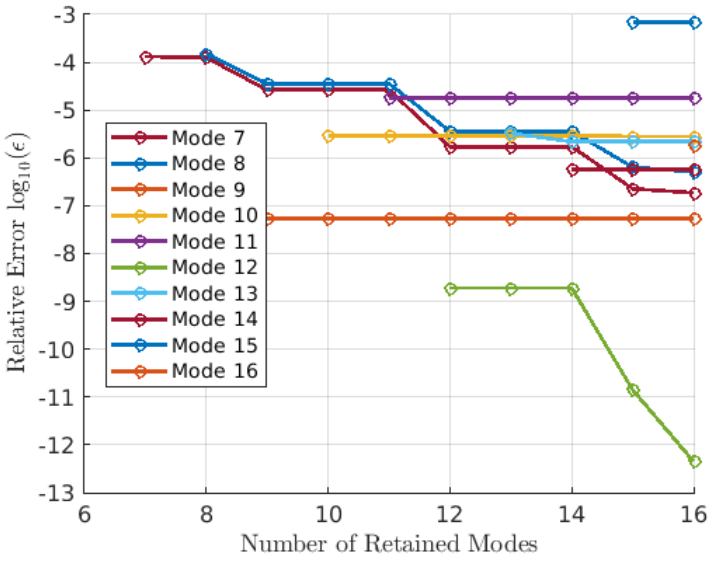

Figure 5.21: Evolution of the relative error between the natural frequencies with the number of modes retained in Craig-Bampton, for an added spring of $10^2\mathrm{N/m}$, using the second strategy.

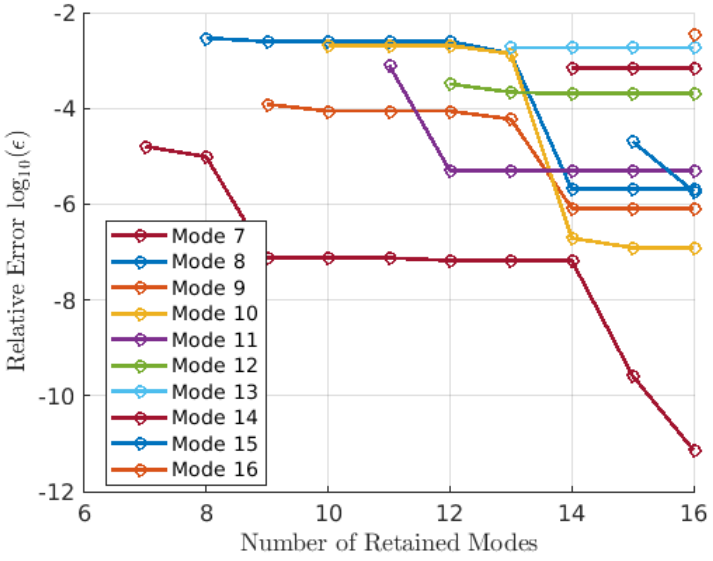

Figure 5.22: Evolution of the relative error between the natural frequencies with the number of modes retained in Craig-Bampton, for an added spring of $10^7\mathrm{N/m}$, using the second strategy.

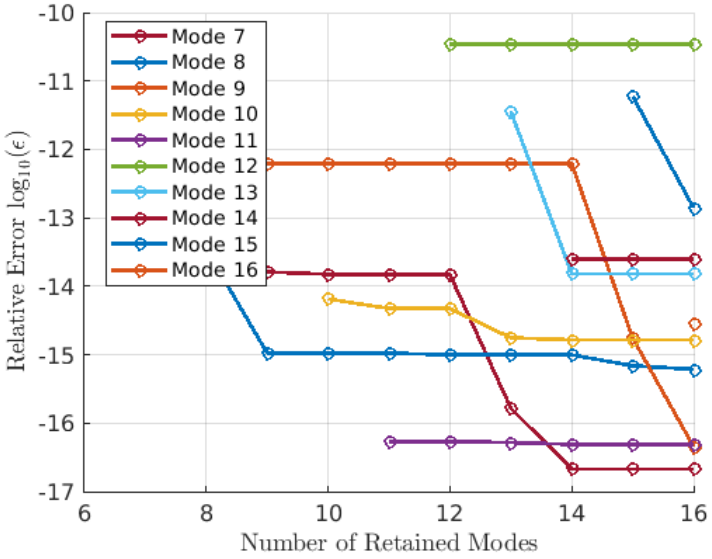

Figure 5.23: Evolution of the relative error between the natural frequencies with the number of modes retained in Craig-Bampton, for an added spring of $10^{10}\mathrm{N/m}$, using the second strategy.

The order of magnitude of the relative errors mirrors those observed for the first strategy and remains quite small, especially for an added spring with a stiffness of 10^{10} N/m. Similar to the first strategy, retaining 12 modes appears to be sufficient for accurately representing the full model with its reduced counterpart. However, to optimize the number of retained modes for each specific case, it is essential to compute the MAC matrices for all three scenarios. This additional step will enable a more tailored and optimal selection of the number of modes to retain based on the characteristics of the system influenced by the different added spring values.

Analysis of MAC matrix for different number of modes retained

For an added spring value of 10^2 N/m, the MAC matrix, depicted in Figure 5.24, already demonstrates a perfect identity for a modest number of retained modes of 7. This observation indicates that the second strategy allows for the retention of a small number of modes in the Craig-Bampton method when a low stiffness value is introduced at the contacts.

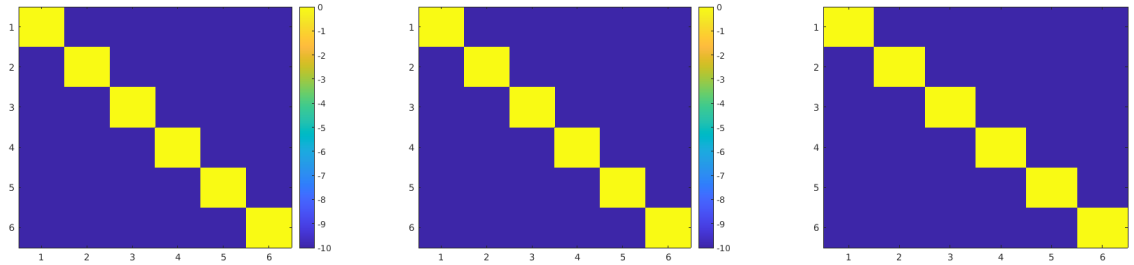

(a) MAC matrix for 7 modes retained.

(b) MAC matrix for 12 modes retained.

(c) MAC matrix for 16 modes retained.

Figure 5.24: MAC matrix comparing modes obtained for the full and reduced model for different number of modes retained, for an added spring of 10^2 N/m, using second strategy.

In Figure 5.25, corresponding to a stiffness value of 10^7 N/m, the MAC matrix does not exhibit a perfect identity behavior, even with 16 modes retained. This stiffness value falls within the mid-range region of Figure 5.11, where high frequency fluctuations occur. This instability suggests that applying the Craig-Bampton method with a small number of retained modes is challenging for this stiffness value. The results imply that a higher number of modes should be retained compared to the first strategy, where 12 modes were sufficient.

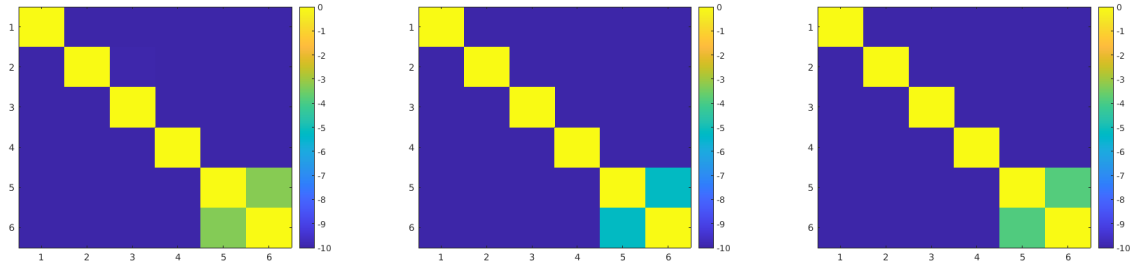

(a) MAC matrix for 7 modes retained.

(b) MAC matrix for 12 modes retained.

(c) MAC matrix for 16 modes retained.

Figure 5.25: MAC matrix comparing modes obtained for the full and reduced model for different number of modes retained, for an added spring of 10^7 N/m, using second strategy.

Lastly, for an added spring value of 10^{10} N/m, the MAC matrix is a perfect identity for 7 modes retained. This outcome suggests that a minimal number of modes can be retained in the reduction method when dealing with high added spring values, indicating a nearly fixed model.

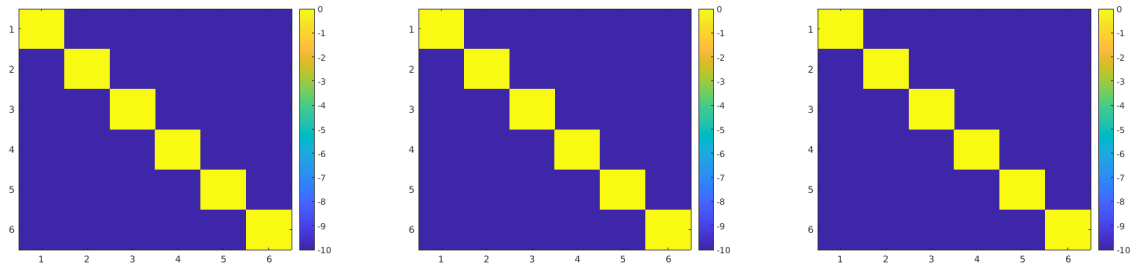

(a) MAC matrix for 7 modes retained.

(b) MAC matrix for 12 modes retained.

(c) MAC matrix for 16 modes retained.

Figure 5.26: MAC matrix comparing modes obtained for the full and reduced model for different number of modes retained, for an added spring of 10^{10} N/m, using second strategy.

Mode shapes on CalculiX

Similar to the first strategy, it is essential to visualize the resulting mode shapes computed in Matlab. This visualization is facilitated on CalculiX by converting the data extracted from Matlab into compatible files for CalculiX.

Figure 5.27 presents the first mode shape related to the first natural frequency at various amplitudes, considering an added spring value of 10^2 N/m on CalculiX.

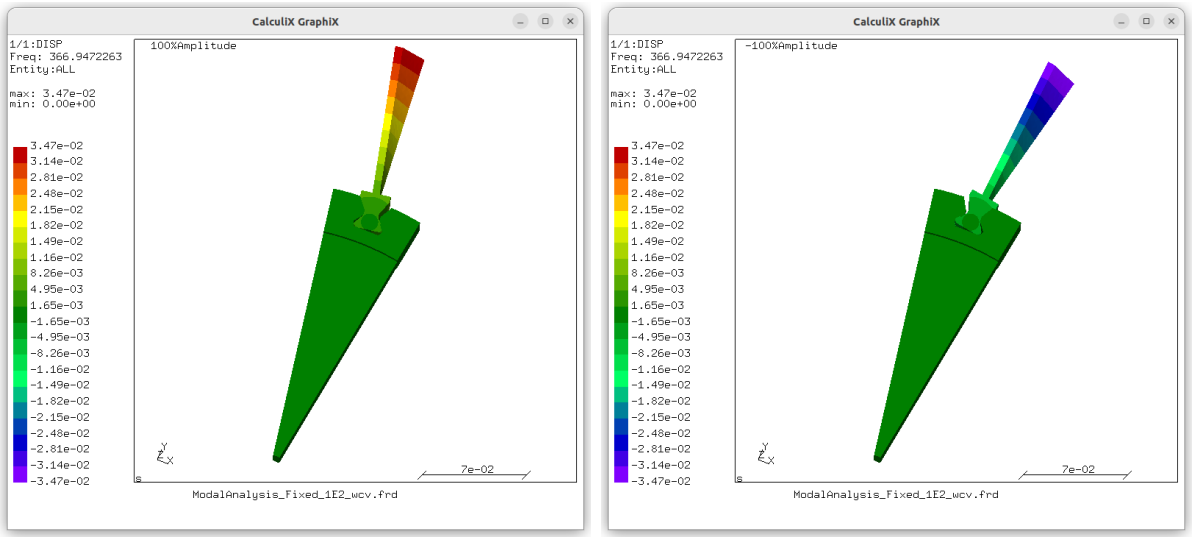

Figure 5.27: Mode shape of the first mode of the model with an added spring of 10^2 N/m on CalculiX, using second strategy.

In Figure 5.28, the first mode shape is visualized, corresponding to the first natural frequency, with an added spring value of 10^7 N/m.

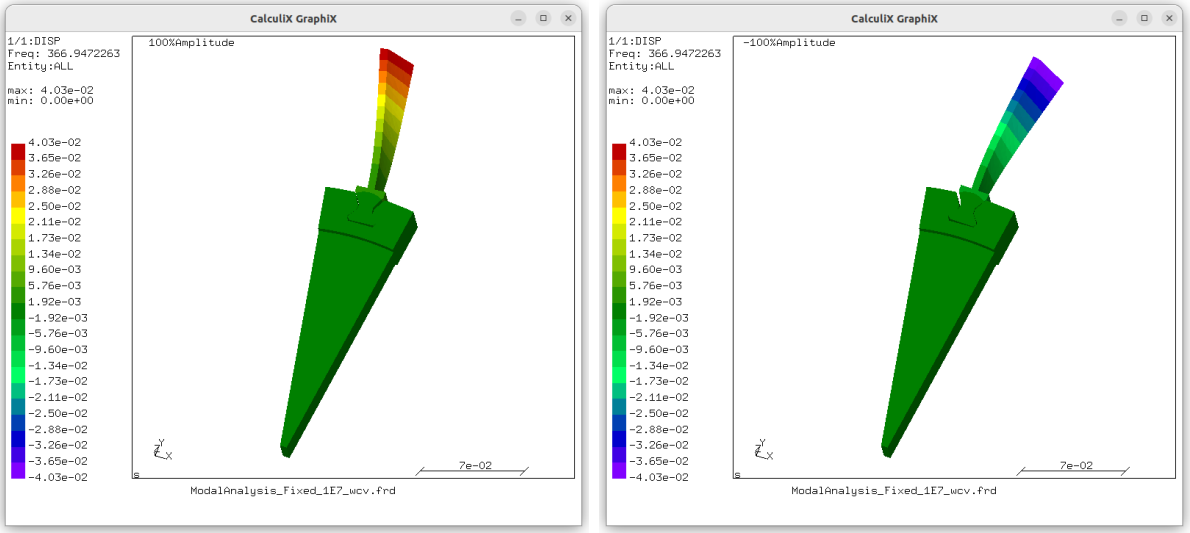

Figure 5.28: Mode shape of the first mode of the model with an added spring of 10^7 N/m on CalculiX, using second strategy.

Figure 5.29 showcases the first mode shape for the first natural frequency, considering an added spring of 10^{10} N/m on Calculix.

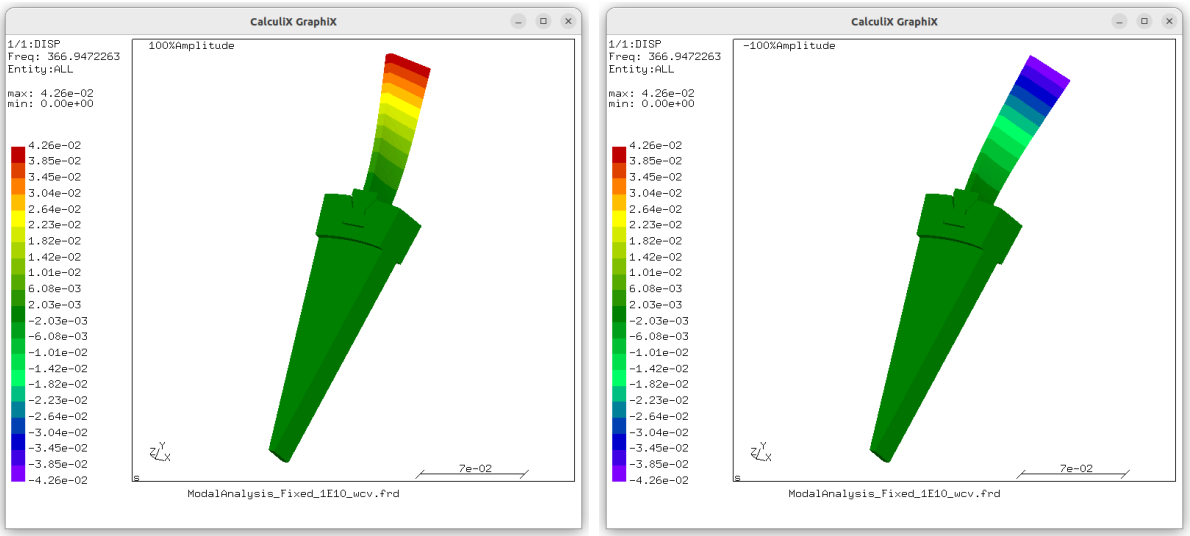

Figure 5.29: Mode shape of the first mode of the model with an added spring of 10^{10} N/m on CalculiX, using second strategy.

5.4.3 Comparison between both strategies

The comparative analysis of two strategies for applying the Craig-Bampton reduction with added springs at contact nodes provides valuable insights into their respective performances. The primary objective is to discern the influence of added spring values on reduced models, shedding light on the strategies' effectiveness in capturing the dynamic characteristics of the system.

Conducting a convergence study reveals the evolution of relative errors with the number of retained modes for both strategies. Figures depicting these analyses demonstrate consistently

small relative errors, with the second strategy exhibiting a trend similar to the first. This convergence study sets the stage for a nuanced examination of the Modal Assurance Criterion matrices, offering deeper insights into the accuracy of the reduced models.

Analyzing the MAC matrices for different numbers of retained modes under various added spring conditions reveals distinctive behaviors for each strategy. The first strategy proves adept at achieving near-perfect identity matrices even with a modest number of retained modes for low and high added spring values. However, mid-range stiffness values demand a higher mode count due to significant frequency fluctuations. In contrast, the second strategy excels in accurately representing low stiffness scenarios with minimal retained modes and demonstrates stability for high added spring values. Nevertheless, it faces challenges in achieving identity behavior for mid-range stiffness, requiring a higher number of retained modes.

The mathematical differences between the two strategies can be understood by considering the influence of the coupling stiffness on the dynamic behavior of the system. The added springs modify the stiffness matrix of the system, affecting the natural frequencies and mode shapes. For the first strategy, the coupling introduced by the springs is incorporated directly into the reduction process (as shown in Equation 4.19), which allows the method to handle low and high stiffness values effectively with fewer modes retained. However, the mid-range stiffness values introduce significant variations in the natural frequencies, requiring more modes to accurately capture the system's dynamics.

On the other hand, the second strategy, which involves a different approach to incorporating the spring stiffness into the reduction process (see Equation 4.20), is more sensitive to changes in stiffness. It performs well for low and high stiffness values due to the simplicity of the dynamic interactions at these extremes. However, for mid-range stiffness values, the complexity of the interactions increases, leading to a need for more retained modes to achieve an accurate representation.

For comparison, Figure 5.30 displays the MAC matrices obtained for an added spring value of 10^7 N/m, with 16 modes retained. As mentioned earlier, it is evident that, in contrast to the first strategy, the second strategy requires a higher number of retained modes, exceeding 16, to achieve a perfect recovery of the identity matrix.

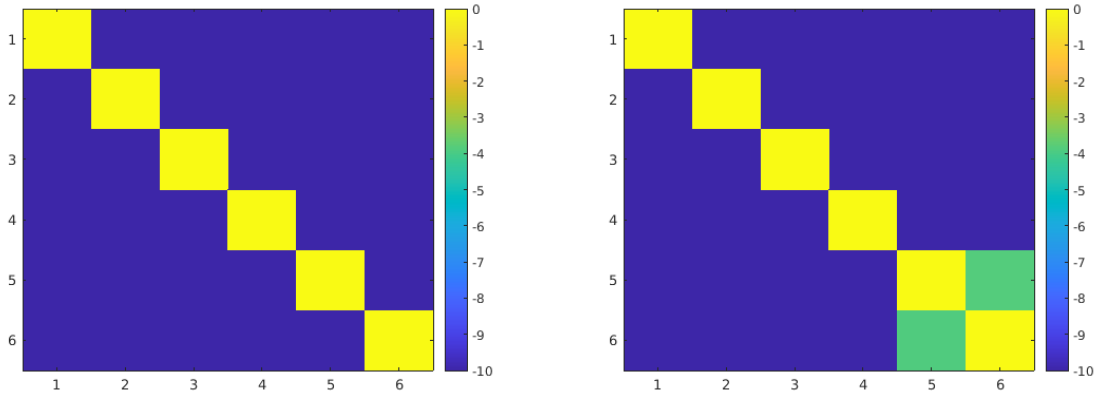

(a) MAC matrix obtained with the first strategy. **(b)** MAC matrix obtained with the second strategy.

Figure 5.30: MAC matrices comparing modes obtained for the full and reduced model for 16 modes retained, for an added spring of 10^7 N/m, for the two strategies.

Visualizing the mode shapes on CalculiX provides a tangible understanding of the strategies' impact on the dynamic behavior of the system. While both strategies effectively capture the altered dynamics induced by varying spring conditions, the first strategy generally exhibits consistent and robust performance, particularly in achieving accurate reductions for different spring values.

In conclusion, the choice between the two strategies depends on the specific characteristics of the added springs and the desired balance between accuracy and computational efficiency. The first strategy demonstrates overall robustness, offering reliable performance across varying spring conditions. The second strategy showcases specific strengths, particularly for low and high added spring values, but requires careful consideration in mid-range stiffness scenarios. This comparative analysis provides a comprehensive overview, aiding practitioners in selecting the most suitable strategy based on their specific modeling requirements and system characteristics.

CHAPTER 6

NONLINEAR RESPONSE OF REDUCED ORDER METHODS

In the context of dynamic system analysis, the incorporation of nonlinearities is paramount for accurately predicting the system's response under various operating conditions. Traditional linear models, while useful for many applications, often fail to capture the complexities introduced by nonlinear elements such as polynomial stiffness and Coulomb friction. These nonlinearities can significantly alter the system's behavior, leading to phenomena such as amplitude-dependent resonance frequencies, harmonic generation, and complex damping effects.

This chapter explores the application of nonlinearities in Reduced Order Models (ROMs), specifically focusing on the two-blade model used in this study. The chapter begins by introducing the nonlinear elements, including a polynomial stiffness and Coulomb friction, integrated into the model to better simulate the dynamic interactions that occur in real-world scenarios.

The nonlinearities are incorporated using the NI2D software, which provides the necessary tools to model these complex interactions effectively. This approach allows for a detailed examination of how these nonlinear forces alter the dynamic behavior of the two-blade model, offering insights into the necessity of including such elements in ROMs for more accurate and reliable predictions.

The application of external forces to the model is also analyzed, with particular attention to the frequency and magnitude of these forces and their impact on the system's response in the presence of nonlinear elements.

This exploration underscores the need to move beyond linear assumptions in dynamic modeling, especially for systems as intricate as those encountered in turbomachinery, where the stakes for accuracy and reliability are high.

6.1 NI2D software

NI2D is a specialized software developed for the analysis and simulation of nonlinear dynamic systems, particularly in the field of structural dynamics. The software was created by a research team at the Université de Liège [19], led by experts in the areas of aeroelasticity and mechanical vibrations, as part of their efforts to advance computational tools for complex engineering applications.

NI2D is designed to handle both linear and nonlinear elements within dynamic models, making it an essential tool for engineers and researchers working with complex mechanical structures. The software's strength lies in its ability to model and simulate the effects of nonlinear forces between specific degrees of freedom (DOFs), which is crucial for accurately predicting the behavior of systems under various operating conditions. Nonlinearities, such as cubic stiffness or Coulomb friction, can be directly integrated into the model, allowing for a detailed analysis of how these factors influence the system's dynamic response.

The software also supports different modeling strategies, such as the application of nonlinear elements between DOFs and the ground when using the Change of Variables (COV) method, or directly between DOFs without COV. This flexibility is valuable for investigating various scenarios and understanding how different configurations affect system behavior.

The interface of NI2D is designed to be user-friendly and intuitive, making it easier for users to define connections between DOFs and visualize the setup of their models. The following figures illustrate two key configurations within the NI2D interface. In Figure 6.1a, a DOF circle with an external force applied is shown, which is typical when examining the dynamic response under specific excitations. This configuration also includes connections between DOFs without applying the COV method, representing the direct interaction between nodes. In Figure 6.1b, the scenario with the COV method applied is demonstrated, where the nonlinear elements are connected to the ground. This figure highlights how the COV method alters the connection strategy within the model, grounding the nonlinear elements instead of directly connecting the DOFs.

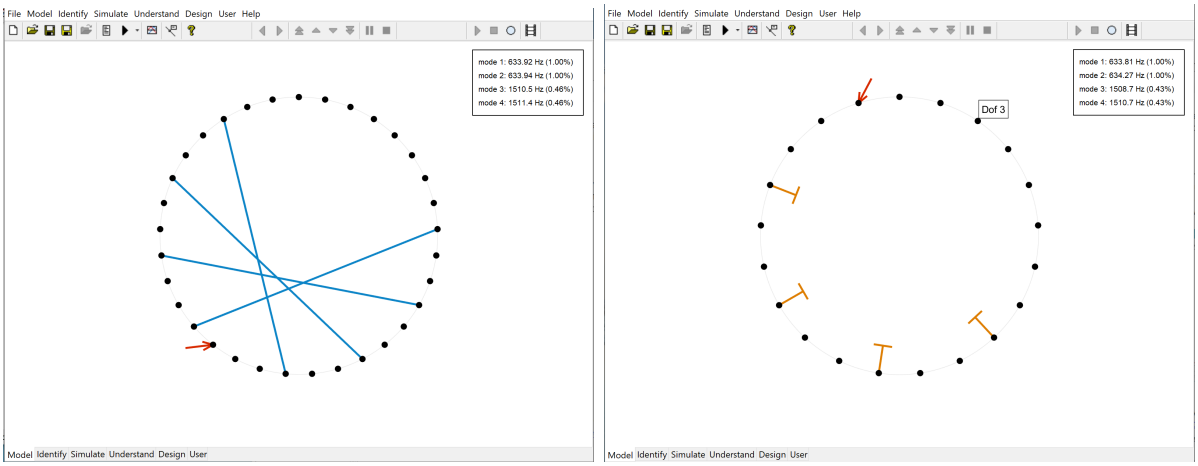

(a) NI2D interface showing the DOF circle with an external force applied and normal connections (without COV).

(b) NI2D interface showing the DOF circle with an external force applied and ground connections (with COV).

Figure 6.1: NI2D interface for two different cases.

These visualizations clarify the structural setup within NI2D and provide insight into how different modeling strategies can be implemented within the software. NI2D 's robust visualization tools, coupled with its advanced simulation capabilities, make it an invaluable tool for studying the nonlinear dynamic behavior of mechanical systems, particularly in fields such as aerospace engineering, mechanical vibrations, and structural analysis.

In summary, NI2D is a versatile and powerful tool for the analysis of nonlinear dynamic systems, offering the precision and flexibility needed to address the challenges posed by

nonlinearities in engineering models. Its development and widespread use in both academic and industrial settings underscore its importance in advancing the field of structural dynamics.

6.2 Addition of non linear polynomial stiffness

The integration of nonlinear polynomial stiffness into the two-blade model significantly enhances the complexity of its dynamic behavior, providing a more accurate representation of the system's physical interactions. The modification of the model involves changes in how connections are made between degrees of freedom, how external forces are applied, and the implementation of proportional damping.

6.2.1 Connections with and without the change of variables

The nonlinear polynomial stiffness is introduced into the model by adding a cubic stiffness element between the x-degrees of freedom (x-DOFs) of selected pairs of contact nodes. This stiffness is represented as a third-degree polynomial with a coefficient of $1000\ \mathrm{N/m^3}$, making the force exerted by the stiffness element proportional to the cube of the displacement between the two nodes.

When the model is configured without applying the Change of Variables (COV) method, the nonlinear stiffness elements are directly connected between the corresponding x-DOFs of the contact nodes. This configuration represents the most straightforward and physically intuitive modeling approach, where the nonlinear stiffness directly influences the interaction between the nodes based on their relative displacements.

In contrast, with the COV method applied, the nonlinear stiffness elements are connected between the x-DOFs of the contact nodes and the ground. This approach effectively transforms the model, using the ground as a reference point for the stiffness elements instead of directly connecting the nodes to each other. This method simplifies the analysis by decoupling the nonlinear interactions from the rest of the system, allowing for a different perspective on how each node behaves relative to a fixed reference.

6.2.2 Application of external force

In both configurations, an external force is applied to a specific degree of freedom to simulate the operational conditions of the system. The force is applied to the 21^{st} DOF, which corresponds to the x-DOF of node 1000091 in the meshed model. This particular node, while not originally a contact node, has been isolated and retained in the reduced model through the Craig-Bampton method to ensure consistent application of the external force across different modeling strategies. Figure 6.2 shows the location where the external force is applied.

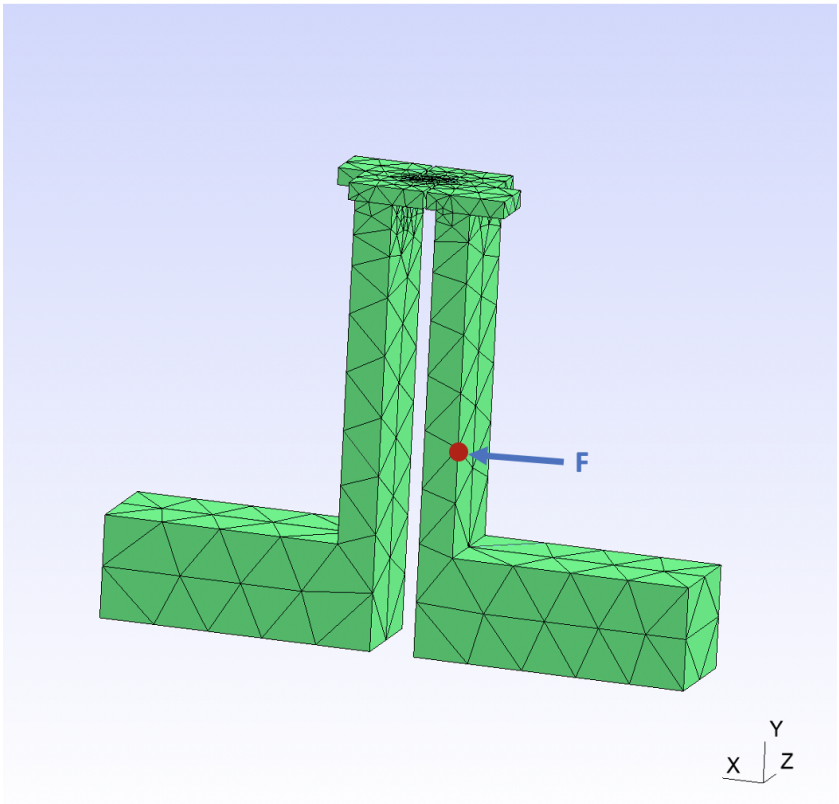

Figure 6.2: Location where the external force is applied at the 21^{st} DOF on the x-DOF of node 1000091.

The external force is sinusoidal with a frequency of 1000 Hz, and its magnitude varies between 0.1 and 20 N. This force simulates external excitations that the blades might encounter during operation, allowing for a detailed examination of how the nonlinear stiffness influences the system's response to varying levels of excitation.

6.2.3 Proportional damping

To account for damping effects within the system, proportional damping, also known as Rayleigh damping, is applied. In scenarios where a specific damping matrix is unavailable, NI2D enables the creation of one using the relationship $C = \alpha \cdot M + \beta \cdot K$, where α and β are coefficients that determine the contribution of mass and stiffness to the damping matrix. The goal is to achieve desired damping ratios over a specified frequency range.

In this study, the frequency band was set between the first and the 15^{th} natural frequencies of the system, ensuring that the modal damping ratios remain below 1% within this range. NI2D offers an advanced procedure [20] to calculate the coefficients α and β based on the desired damping ratios at specific modes. This method allows for precise control of the damping characteristics, ensuring that the system's response is realistically damped without being overly suppressed. As noted by the NI2D documentation [21], setting these coefficients appropriately is crucial to achieving accurate damping behavior within the modeled frequency range.

As shown in Figure 6.3, the evolution of the modal damping with frequency differs between the two strategies. These subfigures provide a visual representation of how the modal damping

varies across the frequency range for each strategy, underscoring the impact of the chosen coefficients on the damping characteristics.

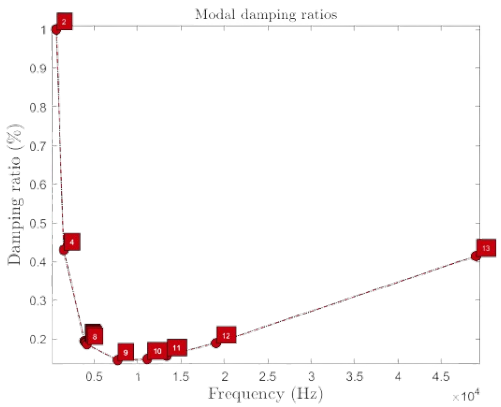

(a) Evolution of modal damping with frequency (with COV).

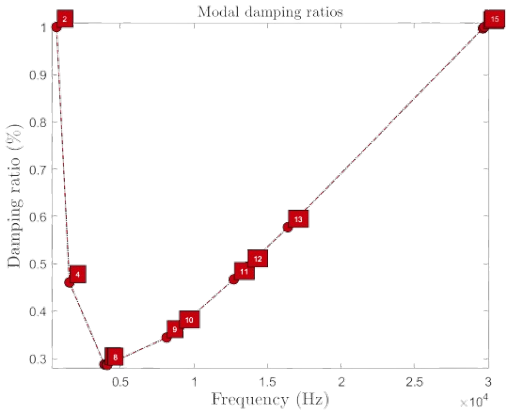

(b) Evolution of modal damping with frequency (without COV).

Figure 6.3: Comparison of the evolutions of modal damping with frequency for the two strategies.

6.2.4 Nonlinear Frequency Response Curves (FRCs)

In the analysis of the nonlinear polynomial stiffness applied to the two-blade model, the obtained nonlinear Frequency Response Curves (FRCs) for the 21^{st} degree of freedom (where the external force is applied) were generated using the harmonic balance continuation method, as described by Detroux et al. [22] and Krack and Gross [23], within the NI2D software. These functions are represented in Figures 6.4 and 6.5. This method is particularly effective for capturing the steady-state response of systems with nonlinearities, providing accurate insights into the resonance behavior and amplitude variations under different force magnitudes.

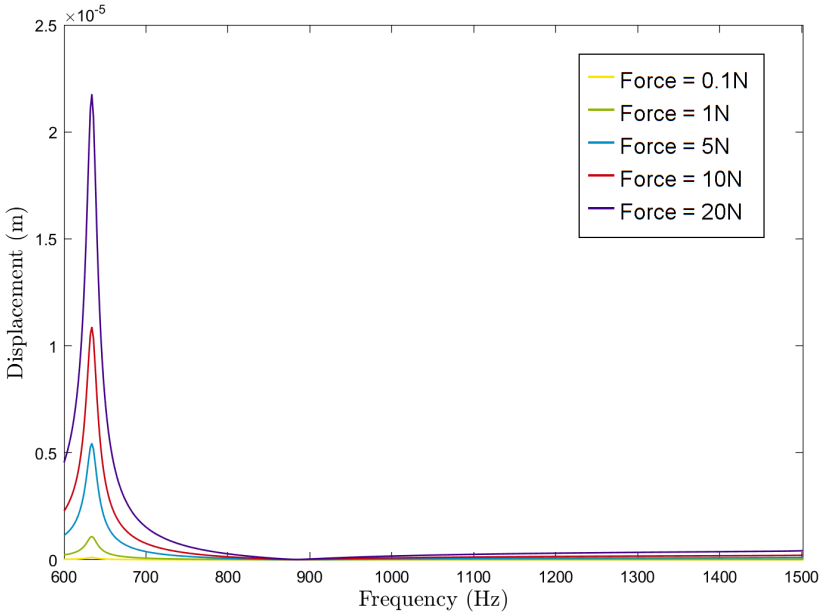

Figure 6.4: Nonlinear FRCs with varying excitations for the first strategy (with COV) at the 21^{st} DOF, with nonlinear polynomial stiffness of 10^3 $\mathrm{N/m^3}$.

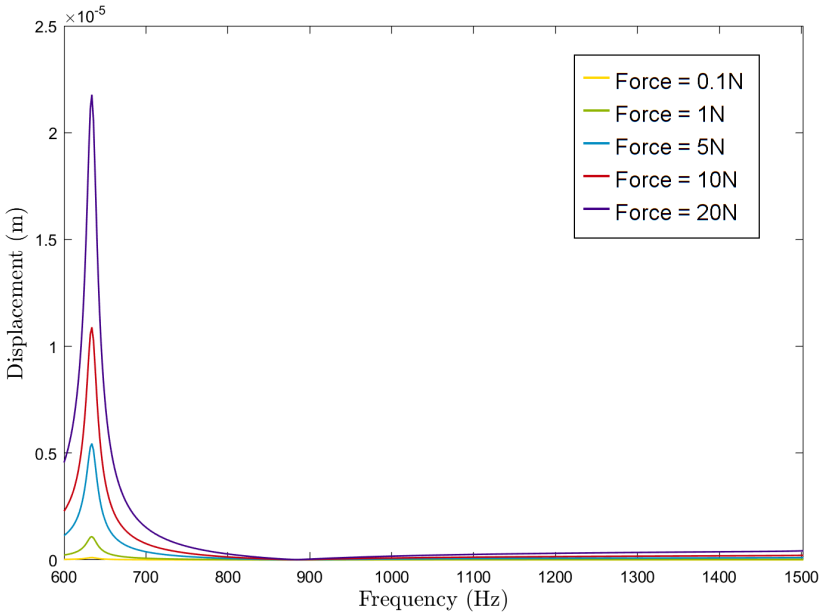

Figure 6.5: Nonlinear FRCs with varying excitations for the second strategy (without COV) at the 21^{st} DOF, with nonlinear polynomial stiffness of 10^3 $\mathrm{N/m^3}$.

The FRCs produced for both modeling strategies — whether the Change of Variables (COV) is applied or not — are remarkably consistent, demonstrating that the dynamic response of the system is captured effectively in both cases. The FRCs reveal a prominent peak near the system's first natural frequency, which indicates the presence of resonance. As

the magnitude of the external force increases from 0.1 N to 20 N, the amplitude of the displacement increases proportionally with the force applied, while the resonance frequency remains largely unchanged. This behavior confirms that the nonlinearity introduced by the cubic stiffness does not lead to a frequency shift in this range of force magnitudes; rather, the amplitude response scales with the external excitation.

Despite the identical FRCs produced by both strategies, there is a slight difference in computational performance. When the COV method is applied, the CPU (Central Processing Unit) time is recorded at 26.79 seconds, slightly lower than the 26.94 seconds recorded without applying the COV. Although this difference is minimal, it suggests a minor computational advantage with the COV method, likely due to the decoupling of nonlinear interactions from the rest of the system, which may simplify the calculations slightly.

For the higher stiffness value of 10^{12} N/m^3, the FRCs produced by both modeling strategies — whether the Change of Variables (COV) is applied or not — continue to show a prominent peak near the system's first natural frequency, as depicted in Figures 6.6 and 6.7. However, while the first strategy (with COV) retains a behavior similar to the lower stiffness case, the second strategy (without COV) begins to exhibit a more pronounced nonlinear behavior.

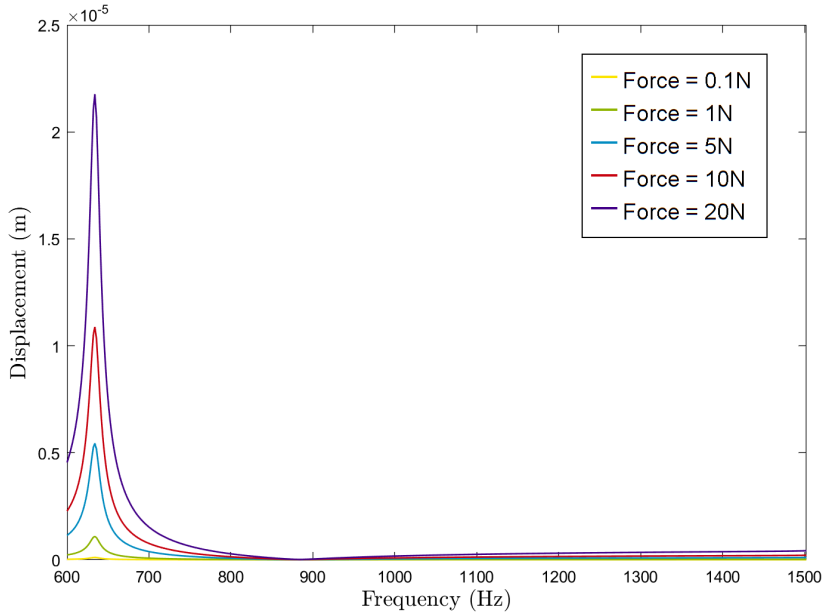

Figure 6.6: Nonlinear FRCs with varying excitations for the first strategy (with COV) at the 21^{st} DOF, with nonlinear polynomial stiffness of 10^{12} N/m^3.

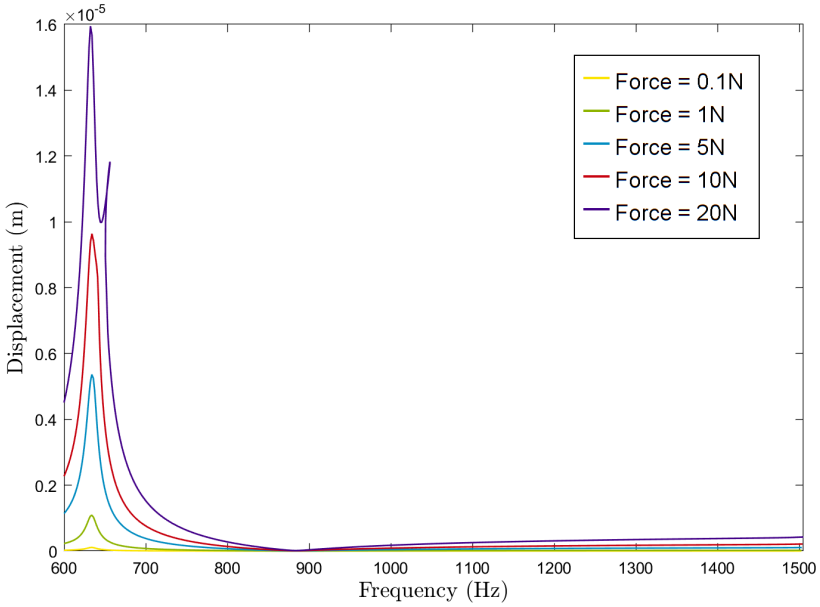

Figure 6.7: Nonlinear FRCs with varying excitations for the second strategy (without COV) at the 21^{st} DOF, with nonlinear polynomial stiffness of 10^{12} $\mathrm{N/m^3}$.

In particular, the FRCs for the second strategy (without COV) demonstrate a noticeable frequency shift and increased nonlinearity as the force magnitude increases. This nonlinear response is characterized by a widening of the resonance peak and a more significant deviation from the linear trend as the external excitation is increased. This behavior is a direct result of the increased stiffness, which amplifies the nonlinear effects and makes the system more sensitive to changes in the excitation force.

The application of the COV method appears to mitigate these nonlinear effects to some extent, likely due to the decoupling of the nonlinear terms from the linear dynamics, which allows the system to respond more linearly to the applied forces. In contrast, without the COV, the full impact of the nonlinear stiffness is felt, resulting in the observed frequency shifts and nonlinear amplitude responses.

Regarding computational performance, similar trends as before are observed. The CPU time recorded for the higher stiffness value is 26.96 seconds with the COV method and 27.10 seconds without it. Although this difference remains minimal, it reinforces the slight computational advantage of the COV method, particularly as the system nonlinearity increases.

Despite these differences, the harmonic balance continuation method in NI2D continues to be a robust tool for analyzing the nonlinear dynamic behavior of the two-blade model, ensuring that the complex interactions introduced by the nonlinear polynomial stiffness are accurately represented.

In summary, the nonlinear FRCs obtained for the higher stiffness value reveal that while both strategies effectively capture the dynamic response, the second strategy (without COV) shows more pronounced nonlinear behavior, particularly at higher force and stiffness magnitudes. The slight improvement in CPU time with the COV method remains consistent, underscoring its potential for more efficient simulations, especially as the system nonlinearity increases.

6.3 Addition of Coulomb friction

The introduction of Coulomb friction into the two-blade model introduces a different type of nonlinearity compared to the previously discussed nonlinear polynomial stiffness. This section discusses how Coulomb friction is integrated into the model, the resulting nonlinear Frequency Response Curves (FRCs), and the differences observed between the two modeling strategies (with and without the Change of Variables method). In real turbine applications, Coulomb friction is commonly encountered in shrouded blades, where frictional forces between the shrouds significantly affect the dynamic behavior of the system, making this model particularly relevant for understanding such effects.

6.3.1 Connections with and without the change of variables

Coulomb friction is added between the x-DOFs of the contact nodes, with a coefficient (Coulomb limit) of 0.1 N and a sharpness factor of 100. Unlike the smooth and continuous nature of polynomial stiffness, Coulomb friction introduces a discontinuous nonlinearity that is highly dependent on the relative motion between the contact nodes.

When the model is configured without applying the COV method, the Coulomb friction forces are directly applied between the corresponding x-DOFs of the contact nodes. This direct interaction captures the frictional forces as they would naturally occur, with the frictional force opposing the relative motion between the nodes.

In contrast, when the COV method is applied, the Coulomb friction elements are connected between the x-DOFs of the contact nodes and the ground. This setup changes the reference for the frictional forces, as the relative motion is now considered with respect to a fixed reference point (ground) rather than another moving node. The change in reference alters how the frictional forces influence the system's dynamic response, leading to different FRC results compared to the non-COV strategy.

6.3.2 Application of external force

The external force applied remains consistent with the previous case involving nonlinear polynomial stiffness. It is applied to the 21^{st} DOF, corresponding to the x-DOF of node 1000091 in the meshed model, as shown in Figure 6.2. The force is sinusoidal, with a frequency of 1000 Hz, and its magnitude varies between 0.1 and 20 N. This setup allows for a direct comparison of how different nonlinear elements (polynomial stiffness vs. Coulomb friction) influence the system's response under identical excitation conditions.

6.3.3 Proportional damping

Proportional damping is implemented in the same manner as described previously, using the relationship $C = \alpha \cdot M + \beta \cdot K$. The damping coefficients are chosen to achieve modal damping ratios below 1% between the first and the 15^{th} natural frequencies of the system, ensuring consistent damping behavior across the different nonlinear models.

6.3.4 Nonlinear Frequency Response Curves (FRCs)

The nonlinear Frequency Response Curves (FRCs) obtained with the addition of Coulomb friction are shown in Figures 6.8 and 6.9. Unlike the FRCs produced with nonlinear polynomial stiffness, the FRCs with Coulomb friction exhibit some differences between the two modeling strategies, particularly at lower excitation levels.

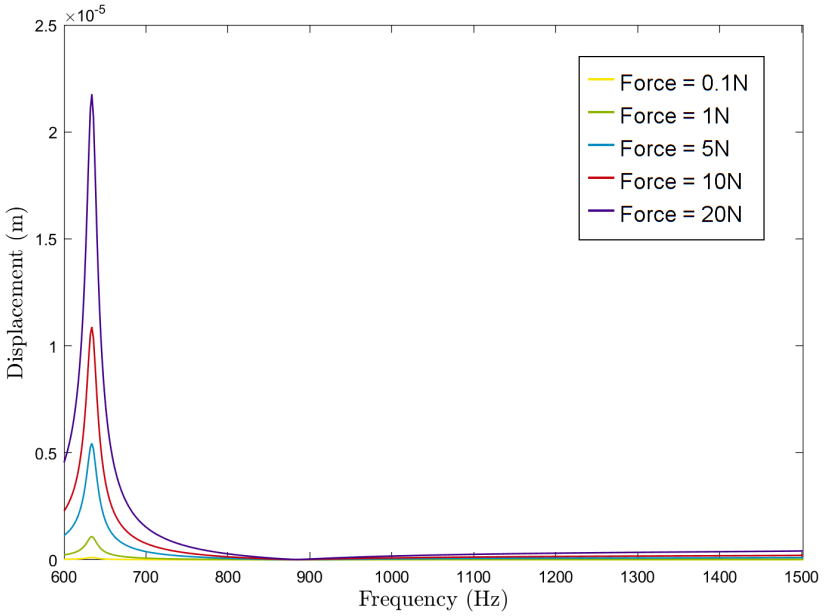

Figure 6.8: Nonlinear FRCs with varying excitations for the first strategy (with COV) at the 21st DOF, with Coulomb friction.

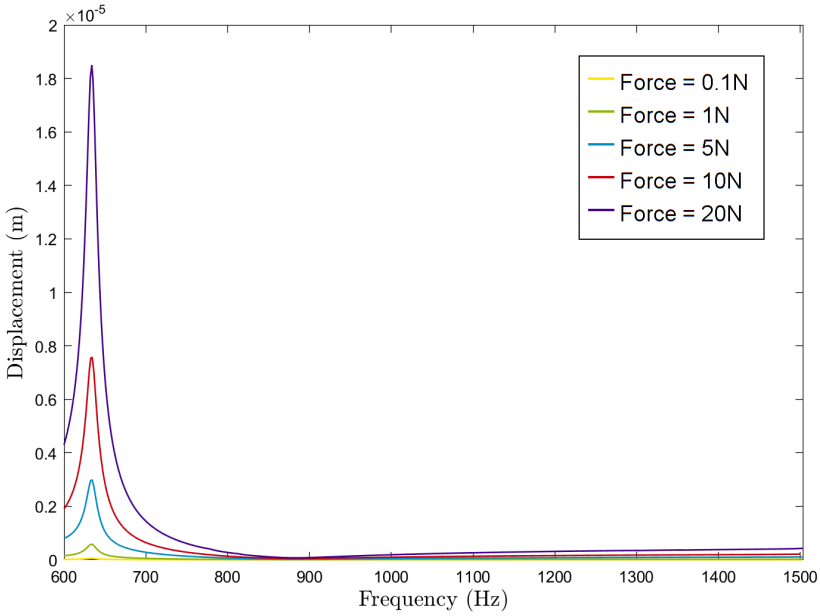

Figure 6.9: Nonlinear FRCs with varying excitations for the second strategy (without COV) at the 21^{st} DOF, with Coulomb friction.

The FRCs reveal that when Coulomb friction is included, the system's dynamic response is more sensitive to the modeling strategy. Specifically, differences in the FRCs are observed at lower force magnitudes, where the frictional forces are more dominant. These differences arise because Coulomb friction is highly dependent on the relative motion between the contact nodes, which is significantly altered by the application of the COV method. The frictional forces respond differently when the relative motion is referenced to the ground, leading to variations in the amplitude and shape of the FRCs.

As the magnitude of the external force increases, the differences between the FRCs for the two strategies become less pronounced. At higher force levels, the system's response is dominated more by the applied force than by the frictional forces, leading to a convergence in the FRCs produced by the two methods.

Despite the observed differences in the FRCs, the computational performance also differs between the two strategies. When the COV method is applied, the CPU time is recorded at 27.14 seconds, slightly lower than the 28.54 seconds recorded without applying the COV. This difference indicates that the COV method offers a more computationally efficient approach, especially in scenarios involving complex frictional interactions.

In summary, the addition of Coulomb friction results in nonlinear FRCs that are more sensitive to the chosen modeling strategy compared to those obtained with nonlinear polynomial stiffness. The observed differences highlight the importance of considering the nature of the nonlinearity when selecting a modeling approach. The COV method, while computationally more efficient, introduces a different reference for frictional forces, which can significantly impact the system's dynamic response, particularly at lower excitation levels.

6.4 Conclusion

In this chapter, the nonlinear dynamic behavior of the two-blade model was analyzed through the addition of different nonlinear elements: a nonlinear polynomial stiffness and Coulomb friction. These nonlinearities were introduced into the model to study their impact on the system's response under varying external excitations, and the effectiveness of two strategies — the application of a COV and a direct approach without COV — was assessed.

The first part of the analysis centered on the nonlinear polynomial stiffness, implemented as a cubic stiffness element with a coefficient of 10^3 $\mathrm{N/m^3}$ and a higher value of 10^{12} $\mathrm{N/m^3}$ between selected degrees of freedom. The nonlinear Frequency Response Curves generated for both stiffness values indicated that the dynamic response, characterized by amplitude and resonance behavior, was effectively captured by both modeling strategies. While the system's resonance frequency remained stable across varying force magnitudes, the introduction of the higher stiffness value began to highlight nonlinear effects, particularly in the direct modeling approach (without COV), where frequency shifts and enhanced nonlinear behavior were observed. The computational efficiency was slightly better with the COV method, although the differences in CPU time were minimal.

In the second part, the addition of Coulomb friction, with a defined friction coefficient and sharpness factor, introduced a different type of nonlinearity. Unlike the polynomial stiffness, the FRCs for Coulomb friction displayed notable differences between the two strategies, especially at lower force levels where frictional forces were more pronounced. The COV method, by altering the reference for the frictional forces, led to variations in the system's response, highlighting the importance of the chosen modeling strategy in accurately capturing friction-induced nonlinearities. As the excitation force increased, these differences diminished, but the COV method continued to offer a slight computational advantage.

Overall, the chapter highlights that while both nonlinear elements impact the dynamic behavior of the system, the choice of modeling strategy — whether to apply a COV or not — can influence both the results and computational efficiency. For higher stiffness values, the direct approach without COV may reveal more pronounced nonlinear behavior, while the COV method provides a more computationally efficient solution, particularly in scenarios involving complex frictional interactions. The harmonic balance continuation method, as implemented in the NI2D software, effectively captured these nonlinear dynamics, offering critical insights into the resonance characteristics and performance trade-offs of the different modeling approaches. The findings suggest that the choice between these strategies should be guided by the specific nonlinear characteristics of the system under study and the available computational resources.

CHAPTER 7

CONCLUSION

This thesis has provided an in-depth analysis of structural dynamics with a particular emphasis on the Craig-Bampton method. The research underscores the method's capability to balance accuracy and computational efficiency, a critical aspect for engineering applications where full-order models are often impractical due to their complexity and computational demands.

The results from the various analyses conducted throughout this thesis reveal several key insights.

Firstly, the application of the Craig-Bampton reduction method to complex systems, such as a bladed disk, demonstrated its robustness in accurately capturing the dynamic behavior of the system while significantly reducing computational load. This method proved especially effective in maintaining the integrity of the modal characteristics, even when simplifying the model.

Secondly, the introduction of springs at contact nodes added a layer of complexity, necessitating a detailed comparative analysis between two reduction strategies. This investigation revealed that the first strategy generally provides a more consistent and robust performance across varying spring conditions, particularly for achieving accurate reductions with fewer modes retained. The second strategy, while effective for low and high stiffness values, faced challenges with mid-range stiffness scenarios, indicating a need for higher mode counts to capture the dynamics accurately.

Evaluations using the Modal Assurance Criterion matrix and mode shape visualizations provided a comprehensive understanding of how each strategy performed under different conditions. The first strategy's ability to achieve near-perfect identity matrices for extreme stiffness values highlights its robustness, whereas the second strategy's stability at these extremes, albeit with a higher sensitivity to mid-range stiffness, underscores the nuanced trade-offs between accuracy and computational efficiency.

In addition to the linear analyses, this thesis also explored the impact of incorporating nonlinearities into the 2-blade model. By introducing nonlinear elements such as nonlinear polynomial stiffness and Coulomb friction, the study extended the evaluation of the Craig-Bampton reduction method to scenarios that more closely mimic real-world operating conditions.

The results of the nonlinear analysis revealed that while the COV and non-COV strategies produced consistent results in the linear case, the inclusion of nonlinear elements, particularly Coulomb friction, introduced significant variations. The FRFs obtained from the two strategies differed, highlighting the sensitivity of the nonlinear response to the choice of reduction strategy. This was especially evident at lower force levels where the frictional forces dominated the dynamic response. However, as the external force increased, the differences between the two strategies diminished, indicating that the nonlinear effects become less pronounced at higher excitations.

Moreover, the nonlinear analysis underscored the importance of selecting an appropriate modeling strategy based on the specific type of nonlinearity involved. For nonlinear polynomial stiffness, both strategies performed similarly, but for Coulomb friction, the choice of strategy had a more substantial impact on the results. The COV method again demonstrated a slight computational advantage, reducing CPU time while maintaining accuracy, making it a preferable choice in scenarios involving complex frictional interactions.

Through the systematic application and evaluation of the Craig-Bampton reduction method across a range of models, this thesis has contributed valuable insights into the efficacy of different reduction strategies. The addition of nonlinear analysis provided a more comprehensive understanding of the dynamic behavior of turbine blades, demonstrating the importance of considering nonlinear effects in the design and analysis process. The findings suggest that while the COV method offers advantages in both linear and nonlinear cases, the choice of reduction strategy should be carefully tailored to the specific characteristics of the system being analyzed.

Overall, the study validates the use of the Craig-Bampton reduction method for efficient and accurate modeling of bladed-disk systems, particularly when extended to include nonlinear dynamic interactions. These results have significant implications for the broader field of structural dynamics, offering guidance for future research and practical applications in the design of high-performance turbomachinery.

Building on the findings of this thesis, future research could explore several avenues to further enhance our understanding and application of reduction methods in structural dynamics. Extended comparative studies involving other reduction techniques could provide a broader perspective on the strengths and weaknesses of each method. This would help in developing hybrid approaches that combine the best features of multiple techniques. Developing algorithms to optimize the selection of retained modes based on specific system requirements and constraints could enhance the method's efficiency. This would involve creating adaptive schemes that dynamically adjust the mode selection criteria in response to changes in system characteristics. Furthermore, exploring the feasibility of implementing the Craig-Bampton reduction method in real-time applications, such as active vibration control and structural health monitoring, could significantly broaden its practical utility. This would require addressing challenges related to computational speed and real-time data processing.

In conclusion, the Craig-Bampton method has proven to be a potent tool in structural dynamics, offering a balanced approach to modeling accuracy and computational efficiency. The insights gained from this thesis not only advance our theoretical understanding but also provide practical guidance for future applications and developments in this field.

BIBLIOGRAPHY

[1] SaVRee. Gas turbines explained (combustion turbine). *Online Course*.

[2] O. Bendiksen, R. E. Kielb, and K. C. Hall. Turbomachinery aeroelasticity. *Encyclopedia of Aerospace Engineering*, 2010.

[3] M. S. Rajput. Evaluation of experimental forced response data of a turbine stage with respect to different stator blade damages. *Royal Institute of Technology*, 2013.

[4] E. P. Petrov and D. J. Ewins. Generic friction models for time-domain vibration analysis of bladed disks. *Centre of Vibration Engineering*, vol. 126, 2004.

[5] J. Yuan, F. Scarpa, G. Allegri, B. Titurus, S. Patsias, and R. Rajasekaran. Efficient computational techniques for mistuning analysis of bladed discs: A review. *Mechanical Systems and Signal Processing*, 2017.

[6] R. J. Guyan. Reduction of stiffness and mass matrices. *AIAA Journal*, vol. 3(no. 2), 1965.

[7] M. T. Yang and J. H. Griffin. A reduced-order model of mistuning using a subset of nominal system modes. *Journal of Engineering for Gas Turbines and Power*, vol. 123, 2001.

[8] J. Yuan, C. Schwingshackl, L. Salles, C. Wong, and S. Patsias. Draft : Reduced order method based on an adaptive formulation and its application to fan blade systeme with dovetail joints. *Proceedings of ASME Turbo Expo 2020: Turbine Technical Conference and Exposition*, June 2020.

[9] J. Yuan, C. Schwingshackl, C. Wong, and L. Salles. On an improved adaptive reduced-order model for the computation of steady-state vibrations in large-scale non-conservative systems with friction joints. *Nonlinear Dynamics*, August 2020.

[10] M. Patil and A. Datta. Three-dimensional aeromechanical analysis of lift offset coaxial rotors: A helios test case. *Journal of Aircraft*, vol. 61(no. 3), May-June 2024. University of Maryland, College Park, Maryland 20742.

[11] M. Guttiérrez Salas. Development of accurate reduced order models in a simulation tool for turbomachinery aeromechanical phenomena. *KTH Royal Institute of Technology*, 2018.

[12] R. R. Craig Jr. and C. J. Chang. A review of substructure coupling methods for dynamic analysis. *University of Texas*, 1976.

[13] J.R. Dormand and P.J. Prince. A family of embedded runge-kutta formulae. *Journal of Computational and Applied Mathematics*, vol. 6:pp. 19–26, 1980.

[14] L.F. Shampine and M.W. Reichelt. The matlab ode suite. *SIAM Journal of Scientific Computing*, vol. 18:pp. 1–22, 1997.

[15] R. R. Craig Jr. and M. C. C. Bampton. Coupling of substructures for dynamic analyses. *AIAA Journal*, vol. 6(no. 7):pp. 1313–1319, 1968.

[16] G. Dhondt. Calculix crunchix user's manual. Version 2.7, 2014.

[17] S. Rodriguez Blanco. Reduced models for the study of aeroelastic vibrations in turbomachinery. *E. T. S. de Ingeneria Aeronautica y del Espacio (UPM)*, 2023.

[18] D. C. Lay, S. R. Lay, and J. J. McDonald. *Linear Algebra and its Applications*. Pearson, 5th ed. edition, 2006.

[19] Université de Liège. Ni2d, a software to analyze non-linear vibrations, May 2017. *News*. Last accessed: 2024-08-19.

[20] Ondrej. Damping coefficients, May 2013. *Computers & Structures Inc.*. Last accessed: 2024-08-19.

[21] Université de Liège. *Ni2D Software Documentation*. Université de Liège, 2024.

[22] T. Detroux, L. Renson, L. Masset, and G. Kerschen. The harmonic balance method for bifurcation analysis of large-scale nonlinear mechanical systems. *Computer Methods in Applied Mechanics and Engineering*, vol. 296:pp. 18–38, November 2015.

[23] M. Krack and J. Gross. *Harmonic balance for nonlinear vibration problems*. Cham: Springer International Publishing, 2019.